Defect Characterization of High-Power Diode Lasers' Facets and Cavities

by

Luyang Wang

A dissertation proposal submitted in partial fulfillment
of the requirements for the degree of
Doctor of Philosophy
(Mechanical Engineering)
in the University of Michigan
2025

Doctoral Committee:

Professor Kevin P. Pipe, Chair
Dr. Robert J. Deri, Lawrence Livermore National Lab
Professor Rachel S. Goldman
Professor Zetian Mi
Professor Pramod S. Reddy

Luyang Wang
luyangw@umich.edu
ORCID iD: 0000-0001-8270-376X

© Luyang Wang 2025

DEDICATION

In memory of my grandpa, Heqi Lu (陆和启).

ACKNOWLEDGEMENTS

The diode laser has been a system that struck me as both complex and deeply fascinating from the moment I was first introduced to it. From that moment on, I've been drawn to studying this device and contributing, in my own way, to the advancement of the field. While the work presented in this dissertation may not stand among the groundbreaking achievements of the giants in this field, I hope it represents one of the countless small forces that, together, drive scientific progress forward. This journey is not easy and would not have been possible without the unwavering support of my Ph.D. advisor, my collaborators, and my family and friends, to whom I owe my deepest gratitude.

First and foremost, I would like to express my deepest gratitude to my Ph.D. advisor, Prof. Kevin Pipe, for his exceptional coaching, mentorship, and unwavering support over the past several years. In the fall of 2019, I had the privilege of joining his research group as a master's student and began working on the diode laser project with only limited knowledge of laser physics. Throughout this long journey, Prof. Pipe coached me with remarkable patience, guide me through challenges, and inspired me with his sharp insights. Beyond academic guidance, he also offered genuine kindness and steady support during the difficult days of the COVID-19 pandemic and the growing geopolitical uncertainties in recent days. I am truly grateful for his support and encouragement over these years.

I am also truly thankful to our collaborators from Lawrence Livermore National Laboratory, Dr. Robert J. Deri, Dr. Salmaan H. Baxamusa, and Dr. Elaine McVay. Our biweekly meetings were consistently filled with wisdom, inspiration, and insight, and I learned a tremendous amount through these interactions. In particular, the support from Dr. Deri and Dr. McVay in simulation and theoretical development was critical to the progress of this dissertation. It has been both a pleasure and a privilege to work with you.

To my dear lab mates, Aman Kumar Jha, Shantonio W. Birch, Shuhao Wan, and Connie Lee, thank you for being an irreplaceable part of this journey. Their presence made the long days brighter and the challenges lighter. Aman was the first to train me when I joined the group and became my collaborator on the laser project. He patiently taught me thermoreflectance, laser physics, and experimental procedures when I knew almost nothing. Even after he graduated, he was always just a message away, ready to help, support, and guide me. The countless hours we spent in the lab are some of my most cherished memories. Although Shantonio and I worked on different projects,

he offered valuable suggestions throughout my research. More importantly, it has been a pleasure having a friend like him, someone I could always share a beer with and have engaging conversations on a variety of topics. Shuhao joined our group two years ago, giving me the opportunity to serve as a mentor and pass on what I had learned. We shared many great moments both in and out of the lab, and I know our brotherhood will last a lifetime. Connie is a kind and thoughtful person whose encouragement and support I will always remember and deeply appreciate.

I would like to thank my parents and grandparents for their unwavering support and unconditional love, not only throughout my Ph.D. journey, but throughout my entire life. You raised me and shaped me into the person I am today. Your encouragement and financial support allowed me to pursue my interests and focus on my work while living comfortably. I am deeply grateful for everything you have done for me. I would also like to express my deepest gratitude to my girlfriend for her companionship and endless patience throughout this journey, especially when obstacles affected my mood. Her understanding and encouragement meant more than words can say.

Special thanks to Prof. Joseph P. Heremans, who invited me for a conversation in his office when I was a junior undergraduate student. During that meeting, he encouraged me to consider pursuing a doctoral degree, a path I had never envisioned for myself before that moment. That conversation became a turning point; it opened a new door and fundamentally reshaped how I viewed my future, ultimately leading me to begin this journey toward a Ph.D.

This work was performed under the auspices of the U.S. Department of Energy by Lawrence Livermore National Laboratory under Contract DE-AC52-07NA27344.

TABLE OF CONTENTS

DEDICATION ii

ACKNOWLEDGEMENTS iii

LIST OF FIGURES vii

LIST OF TABLES xi

LIST OF ACRONYMS xii

ABSTRACT xiv

CHAPTER

1 Introduction 1

1.1 Diode Lasers 1
1.1.1 Fundamental Principles of Diode Lasers 1
1.1.2 Basic Structures of Diode Lasers 2
1.1.3 Non-radiative Recombination 6
1.2 Degradation in Diode Lasers 7
1.2.1 Rapid Degradation 8
1.2.2 Gradual Degradation 10
1.2.3 Catastrophic Optical Damage 10
1.3 Mechanisms of Dark Line Defect Propagation 13
1.3.1 Dark Line Defect Propagation during COD 14
1.3.2 Dark Line Defect Propagation during Rapid and Gradual Degradation . . 15
1.4 Defect Characterization Methods for Diode Lasers 18
1.4.1 Destructive Methods 19
1.4.2 Non-destructive Methods 20
1.5 Defect Characterization Methods used in this Dissertation 23

2 Temperature Profiling of a High-Power Diode Laser Facet During Aging 24

2.1 Physics Behind Thermoreflectance 24
2.2 CCD-based Thermoreflectance 26
2.3 Experimental Setup and Protocol 29
2.3.1 Device Under Test 29
2.3.2 Thermoreflectance System 29

2.3.3 Thermoreflectance Coefficient Calibration . . . 30
2.3.4 Experimental Protocol . . . 32
2.4 Results . . . 33
2.4.1 DC Images and SEM Images of the Laser . . . 33
2.4.2 Temperature Maps . . . 36
2.4.3 Laser Emission Profile . . . 41
2.4.4 PIV Data . . . 43
2.4.5 Facet Optical Absorption . . . 45
2.4.6 Discussion of Facet Temperature Profiling . . . 45

3 Defect Characterization of High-Power Diode Lasers Cavities During Aging . . . 48

3.1 Broad Band NIR Emission . . . 48
3.1.1 Device Under Test . . . 49
3.1.2 Experimental Setup . . . 49
3.1.3 NIR Properties . . . 50
3.2 In situ, Non-destructive NIR Imaging Technique . . . 53
3.2.1 Time-resolved NIR Intensity Maps . . . 53
3.2.2 Optical Power and Centroid Wavelength Shift . . . 71
3.2.3 LBIC Results . . . 73
3.2.4 Thermoreflectance Results . . . 74
3.2.5 Discussion . . . 80

4 Photon-accelerated REDG Mechanism . . . 82

4.1 Mechanisms behind REDG Effect . . . 82
4.1.1 Phonon-kick Mechanism . . . 82
4.1.2 Thermal Stress Mechanism . . . 85
4.2 Longitudinal Spatial Dependence of DLD Growth Velocity in Diode Lasers . . . 85
4.2.1 Calculation of DLD Growth Velocity . . . 86
4.2.2 Longitudinal Spatial Hole Burning Simulation . . . 88
4.2.3 Asymmetric DLD Propagation . . . 89
4.2.4 Photon-accelerated REDG . . . 90
4.2.5 Non-linear Regression Fit . . . 92

5 Summary and Future Work . . . 94

5.1 Summary . . . 94
5.2 Future Work . . . 96
5.2.1 Nature of DLDs that lead to COMD . . . 96
5.2.2 Expanding the NIR Defect Imaging Technique to Devices at Various Wavelengths . . . 97
5.2.3 Mitigation of the Photon-accelerated REDG Process . . . 97

APPENDIX . . . 98

LIST OF FIGURES

FIGURE

1.1 Spontaneous emission and stimulated emission. 2
1.2 a) Schematic of a homojunction diode laser with Fabry-Pérot cavity. b) Band diagram of a homojunction laser under zero bias and forward bias, where E_v represents the valance band, E_c represents the conduction band, E_f represents the Fermi level at equilibrium, E_{fn} and E_{fp} represent quasi-Fermi levels under non-equilibrium conditions. 3
1.3 Band gap energies and lattice constants of common III–V compound semiconductors used for high-power diode lasers. Compound binaries are represented as solid dots and ternaries as solid lines. Dashed lines represent regions of indirect gap. The two dot–dashed vertical lines show the range of bandgap energies of ternaries and quaternaries that can be grown lattice-matched on the binary substrates GaAs and InP[3]. 4
1.4 Regular double heterostructure and separate confinement double heterostructure in diode lasers. 5
1.5 a) Density of state in QW and bulk material. b) Carrier distribution in QW and bulk material. 6
1.6 Degradation modes in diode lasers at constant a) power output, b) drive current [6]. . . 8
1.7 Cathodoluminescence, electron beam induced current and TEM images of DLDs. . . . 9
1.8 Cathodoluminescence images of defects: (left) gradual degradation, (middle) rapid degradation, (right) COD after gradual degradation [19]. 10
1.9 Images of diode lasers after two types of COD. 11
1.10 Two feedback loops in thermal runaway [38]. 12
1.11 Sequential images of the entire COD, each image is 8.5 μs duration [42]. 12
1.12 Schematic of the sequence of events during COD. Note that the temperature indicated on the y-axis does not necessarily correspond to hot spots on the facet; it can also represent hotspots located within the laser cavity [38]. 14
1.13 Illustration of a) the climb motion of an edge dislocation, b) jogs that form the climb motion of a edge dislocation (left) and a screw dislocation (right) [87]. 16
1.14 Illustration of a) the glide motion of an edge dislocation (arrows indicate the applied shear stress), b) kinks that form the glide motion of a edge dislocation (left) and a screw dislocation (right) [87]. 17
1.15 Elongation process of $\langle 100 \rangle$ DLDs [12]. 18
1.16 Energy diagram of photon matter scattering [115]. 20

2.1 A Schematic of the 4-bucket thermoreflectance imaging technique [36]. 28
2.2 Image of the device under test, along with microscopic images of its facet captured at 10× and 100× magnification [36]. 29

2.3 CCD-based thermoreflectance imaging setup used in this experiment. 30
2.4 A schematic of the 2-bucket thermoreflectance imaging technique. 31
2.5 Thermoreflectance coefficients of substrate, waveguide, and cladding materials. 32
2.6 DC images of the laser facet, including the active region, a small portion of the substrate, and a small portion of the solder. 34
2.7 a) SEM images of the front facet stitched together, b) chemical composition of a point on the facet without foreign matter, c) chemical composition of the foreign matter in the middle of the facet. 35
2.8 2D thermal maps at 4A from 0 to 1262 hours. The laser failed during TR measurement at 768 hours when current was 4A. Due to that reason, at 768 hours the 3.5A thermal map is presented instead. 39
2.9 Average temperature increase across the active region at 4A (relative to average off-state active region temperature) before laser failure. 40
2.10 a) Six selected regions on the facet (region 2 is a control region in which no hot spot is observed). b) average temperature increase across a given region at 4A from 0 to 1262 hours. 41
2.11 a) Laser emission profile at 36 hours and 769 hours in comparison with temperature profile just before and after laser failure. b) Temperature profiles (averaged in the fast axis direction) within the epitaxial layers at the facet along the slow axis direction just before and after failure. (c) Normalized emission profile within the epitaxial layers at the facet along the slow axis direction just after failure. 42
2.12 PIV characteristics of the laser under test over its lifetime, a) optical power percentage (relative to initial state) at 4A. b) optical power percentage at 4A before failure, c) optical power percentage at 4A after failure, (d) centroid wavelength at 4A, (e) voltage between laser electrodes at 4A. 44
2.13 a) ΔT of active region vs. waste heat for above and below threshold current points. b) Slope of 2nd order polynomial fitting line at 4A from 0 to 720 hours, as an indicator of facet absorption. 45

3.1 a) Image of a device undergoing cavity defect characterization. b) Schematic of the high-power diode laser being measured (top left inset shows the front view). 49
3.2 Spectrum of the broadband NIR from the n-contact window. 50
3.3 a) Photoluminescence intensity map of NIR emission measured from the laser facet under a 100X objective (Excitation wavelength at 970 nm). b) Electroluminescence intensity map of NIR emission measured from the laser facet under a 100X objective (I_{Laser} = 500 mA). 51
3.4 a) Average intensity of NIR in p-contact region along the cavity of device CTNW5 at 0 hour. Different lines represent data collected at currents below and above threshold. b) Average NIR intensity of the entire p-contact region (blue) and L-I curve (orange) of device CTNW5 at 0 hours. 52
3.5 Intensity maps of NIR emission from the n-contact window under a 10X objective (CTNW5 at 0.7A after 100 hours of aging). Only three fourths of the total cavity length can be seen in one image due to a limited camera field of view. 53
3.6 Intensity maps of the NIR emission from the n-contact window of device CTNW2 from 0 to 850 hours (10X, $I_{laser} = 0.7A$). 56

3.7 Intensity maps of the NIR emission from the n-contact window of device CTNW3 from 0 to 750 hours (10X, $I_{laser} = 0.7A$) . . . 58
3.8 Intensity maps of the NIR emission from the n-contact window of device CTNW4 from 0 to 201 hours (10X, $I_{laser} = 0.7A$) . . . 59
3.9 Intensity maps of the NIR emission from the n-contact window of device CTNW5 from 0 to 700 hours (10X, $I_{laser} = 0.7A$) . . . 61
3.10 Intensity maps of the NIR emission from the n-contact window of device CTNW10 from 0 to 500 hours (10X, $I_{laser} = 0.7A$) . . . 62
3.11 Intensity maps of the NIR emission from the n-contact window of device CTNW11 from 0 to 800.5 hours (10X, $I_{laser} = 0.7A$) . . . 63
3.12 Intensity maps of the NIR emission from the n-contact window of device CTNW33 from 0 to 500 hours (10X, $I_{laser} = 0.7A$) . . . 65
3.13 Intensity maps of the NIR emission from the n-contact window of device T120TA from 0 to 596 hours (10X, $I_{laser} = 0.7A$) . . . 66
3.14 Intensity maps of the NIR emission from the n-contact window of device T120Z9 from 0 to 2202.5 hours (10X, $I_{laser} = 0.7A$) . . . 71
3.15 a) Optical power change vs. aging at 3.5A. b) Wavelength shift from fresh device condition at 3.5A. . . . 72
3.16 Correlation between the number of ”dark” pixels caused by DLD propagation and the optical power decrease for device CTNW2. . . . 73
3.17 Comparison of NIR emission and laser beam induced current (LBIC) signals along the optical axis of device CTNW3 at 750 hours of aging with the region in which a large dark line is observed indicated by a red box. . . . 73
3.18 a) Selected 2D thermal profiles of device CTNW2 at 4 A, along with near-field laser emission profiles at 800 hours and 850 hours. b) Averaged near-field emission profile along the slow axis. c) Temperature profiles (averaged in the fast axis direction) within the epitaxial layers at the facet along the slow axis. d) Averaged NIR intensity near the front facet along the slow axis. . . . 75
3.19 Selected 2D thermal profiles of device CTNW3 at 4 A. . . . 76
3.20 Selected 2D thermal profiles of device CTNW4 at 4 A. . . . 76
3.21 Selected 2D thermal profiles of device CTNW10 at 4 A. . . . 77
3.22 a) Selected 2D thermal profiles of device CTNW11 at 4 A, along with near-field laser emission profiles at 700 hours and 900 hours. b) Averaged near-field emission profile along the slow axis. c) Temperature profiles (averaged in the fast axis direction) within the epitaxial layers at the facet along the slow axis. d) Averaged NIR intensity near the front facet along the slow axis. . . . 79
3.23 Selected 2D thermal profiles of device T120TA at 4 A. . . . 79
3.24 DC images of device T120TA at a) 0 hours, b) 500 hours, c) 595.5 hours. . . . 80
3.25 Selected 2D thermal profiles of device T120Z9 at 4 A. . . . 80

4.1 Band diagram of a defect energy state in the band gap of a semiconductor [88]. . . . 83
4.2 The number distribution functions $n(E)$ of defect molecules possessing vibration energy between E and $E + dE$ [104]. . . . 84

4.3 a) Average DLD growth rate (measured) for segments along the cavity vs. distance from the AR facet (segment length = 200 μm) and non-linear regression fitted DLD growth rate for different m values. b) Number of dark line defect propagation observed for segments along the cavity vs. distance from the AR facet (segment length = 200 μm) 87
4.4 Simulation results of photon density and waveguide carrier density along the longitudinal direction. Negative photon density (S^-) represents light propagating toward the AR facet, while positive photon density (S^+) represents light propagating toward the HR facet. The total photon density is the sum of both components. Note that the relative variation of simulated carrier density in the quantum well is very similar to that in the waveguide. 89
4.5 Illustration of asymmetric dark line defect (DLD) propagation driven by a large S^- to S^+ ratio closer to the AR facet. The initial dark spots are represented by grey spots, while the dark spot after propagation are shown as a black spots. 90
4.6 Ratio of the photon-assisted component to the total DLD growth velocity. 93

A.1 Thermal maps of device CTNW2 at 4 A from 0 to 850 hours. 99
A.2 Thermal maps of device CTNW3 at 4 A from 0 to 750 hours. 100
A.3 Thermal maps of device CTNW10 at 4 A from 0 to 500 hours. 101
A.4 Thermal maps of device CTNW11 at 4 A from 0 to 1000 hours. 102
A.5 Thermal maps of device T120TA at 4 A from 0 to 595.5 hours. 103
A.6 Thermal maps of device T120Z9 at 4 A from 0 to 2202.5 hours. 105

LIST OF TABLES

TABLE

2.1 Aging conditions and aging steps over the laser lifetime 33

3.1 Aging conditions over the lifetime of device T120Z9 67

LIST OF ACRONYMS

AFM atomic force microscopy

AR anti-reflective

C-AFM conductive atomic force microscopy

CL cathodoluminescence

COBD catastrophic optical bulk damage

COD catastrophic optical damage

COMD catastrophic optical mirror damage

CW continuous wave

DLDs dark line defects

DSDs dark spot defects

EBIC electron beam induced current

EL electroluminescence

HR highly-reflective

IFVD impurity-free vacancy disordering

IID impurity-induced disordering

LBIC laser beam induced current

LID laser-induced disordering

LSHB longitudinal spatial hole burning

NIR near infrared

OSA optical spectrum analyzer

PL photonluminescence

QCW quasi-continuous wave

QW quantum well

REDC recombination enhanced dislocation climb

REDG recombination enhanced dislocation glide

REDR recombination enhanced defect reaction

SEM scanning electron microscopy

TEC thermoelectric cooler

TEM transmission electron microscopy

TR thermoreflectance

TRC thermoreflectance coefficient

ABSTRACT

Diode lasers are widely used in various aspects of daily life, including medical devices, industrial manufacturing, and fiber-optic communication, owing to their high optical output, excellent beam quality, high efficiency, spectral coherence, and compact size. For high-power diode lasers, the three most critical performance metrics are maximum optical power output, efficiency, and device lifetime. However, all of these are fundamentally limited by degradation processes that occur within the chip during laser operation. These degradation processes are typically classified into three categories: rapid degradation, gradual degradation, and catastrophic optical damage (COD). Each of these modes is closely linked to the formation and evolution of defects, either on the front facet or within the laser cavity. Therefore, investigating the mechanisms behind defect formation and propagation is essential for understanding the degradation behavior of diode lasers and offers valuable insights for developing strategies to enhance device reliability and increase optical power without accelerating failure.

In this dissertation, defect formation and evolution were monitored using non-destructive methods to characterize both facet and cavity defects in diode lasers. Given the well-established correlation between non-radiative defects and localized heating, thermal maps of the device's front facet can yield valuable information on the formation and progression of small point defect clusters at or near the facet during laser aging. To capture this information, a high-spatial-resolution CCD-based thermoreflectance technique was employed to profile the thermal behavior of the device facet throughout its lifetime. This technique offers a spatial resolution of approximately 0.5 μm and a temperature resolution of about 0.2 K. Thermal maps collected over the device lifetime revealed that the average temperature rise (ΔT) of the active region increased from approximately 20 K to 45 K accompanied by the formation of several localized hot spots, including two highly concentrated regions that emerged just before and after catastrophic optical damage (COD). The occurrence of COD was indicated by a sudden loss of 68% of the original optical output power. These concentrated hot spots were found to correlate with localized loss of light emission. However, SEM imaging of the facet presented no observable morphological changes, suggesting that the associated defects are either too small to be resolved by SEM or are located beneath the facet surface.

To image defect formation and evolution within the device cavity, an in situ and non-destructive NIR defect imaging technique was developed. This method utilizes broadband NIR emission

originating from the core layers of the laser. Because its wavelength (λ_{NIR} ≥910 nm) is longer than the absorption edge of GaAs (λ_{GaAs} ≃870 nm), this emission enables defect imaging through the substrate, even when the substrate is opaque at the lasing wavelength (λ_{lasing} ≃ 790 nm). The technique achieves a spatial resolution of approximately 1 μm. Using this approach, the evolution of dark line defects (DLDs) during aging was observed in 7 out of 9 devices. Correlations were established between observed defect growth characteristics and changes in key device parameters such as optical output power and lasing wavelength. Results show that gradual degradation is associated with DLDs that slowly propagate from pre-existing dark spots present in the device interior at the fresh (unaged) state, rather than from new spots formed during aging. This finding suggests the potential for early-stage screening of fresh devices based on initial defect signatures to predict long-term reliability.

A longitudinal spatial dependence of the dark line defect growth velocity was observed from cavity defect images, captured using the NIR defect imaging technique. The growth rate for dark line defect located 100 μm from the facet is approximately 3 times higher than that for dark line defect located 1000 μm from the facet. This observation, along with the known non-uniform distribution of photon and carrier densities along the laser cavity, driven by the longitudinal spatial hole burning (LSHB) effect, motivated an investigation into the underlying mechanism responsible for the position dependent DLD growth. A photon-accelerated defect growth mechanism is proposed. In contrast to the widely accepted recombination enhanced dislocation glide (REDG) mechanism, where carrier capture is the primary driver of defect propagation, the proposed mechanism highlights photon absorption as the dominant contributor to defect motion in diode laser devices. This does not exclude the role of carrier capture; rather, it suggests that both processes are active, with photon-induced energy deposition playing a leading role under the observed conditions. Nonlinear regression fitting, performed using the measured DLD growth rates and the simulated photon and carrier density profiles, confirms that photon absorption accounts for more than 65% of the contribution to DLD propagation near the facet and more than 50 % at 1000 μm from the facet, providing strong support for the proposed photon-accelerated growth mechanism.

CHAPTER 1

Introduction

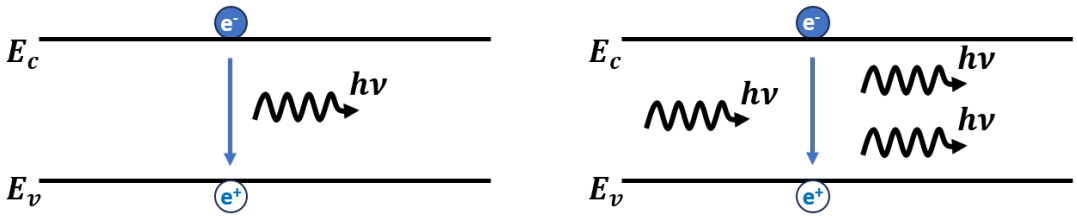
1.1 Diode Lasers

1.1.1 Fundamental Principles of Diode Lasers

LASER, an acronym for Light Amplification by Stimulated Emission of Radiation, produces light that differs from that generated by thermal radiation. Laser light exhibits spectral coherence, superior beam quality, high power density, and extremely short pulse duration. These distinctive properties enable a wide range of applications. Lasers incorporate a gain medium and a resonant optical cavity. Depending on the physical state of the gain medium, lasers are categorized into several types: gas lasers (He-Ne, CO_2, Ar, etc.), liquid lasers (dye solution), and solid-state lasers (Rubby, Nd: YAG, semiconductors, etc). In this dissertation, the emphasis is placed on high-power diode lasers. Since Robert N. Hall [1] and Marshall Nathan [2] independently demonstrated coherent light emission from a GaAs semiconductor diode in 1962, diode lasers have been playing an important role not only in advancing science and technology but also in various aspects of daily life. Examples include fiber optic communications, medical procedures, industrial manufacturing, and autonomous vehicles, etc.

In diode lasers, the gain media are semiconductors that have different band gap energies. The band gap energy of the medium determines the wavelength of light generated by a diode laser. By pumping the gain media electrically, electrons in the semiconductor's valence band are excited to higher, non-equilibrium energy levels in the conduction band, achieving what is known as population inversion. These excited electrons will spontaneously relax back to lower, equilibrium energy levels in the valence band after a certain amount of time by emitting photons with energy corresponding to the band gap energy. This process is called spontaneous emission (Figure 1.1a). Stimulated emission, however, is the crucial process that leads to the amplification and coherence of light coming out of a diode laser. The presence of an incident photon prompts an excited electron to release a photon before natural relaxation (Figure 1.1b). The emitted photon has the

same frequency, propagation direction, and phase as the initiating photon, fostering the exponential increase in coherent photons, which is essential for the laser's amplified and coherent output.



(a) Spontaneous emission

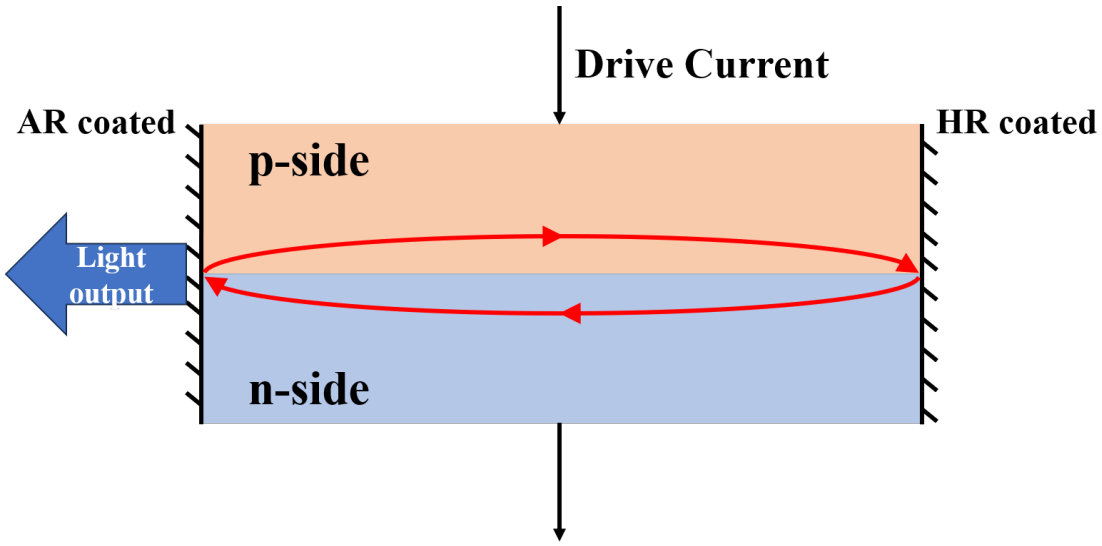
(b) Stimulated emission

Figure 1.1: Spontaneous emission and stimulated emission.

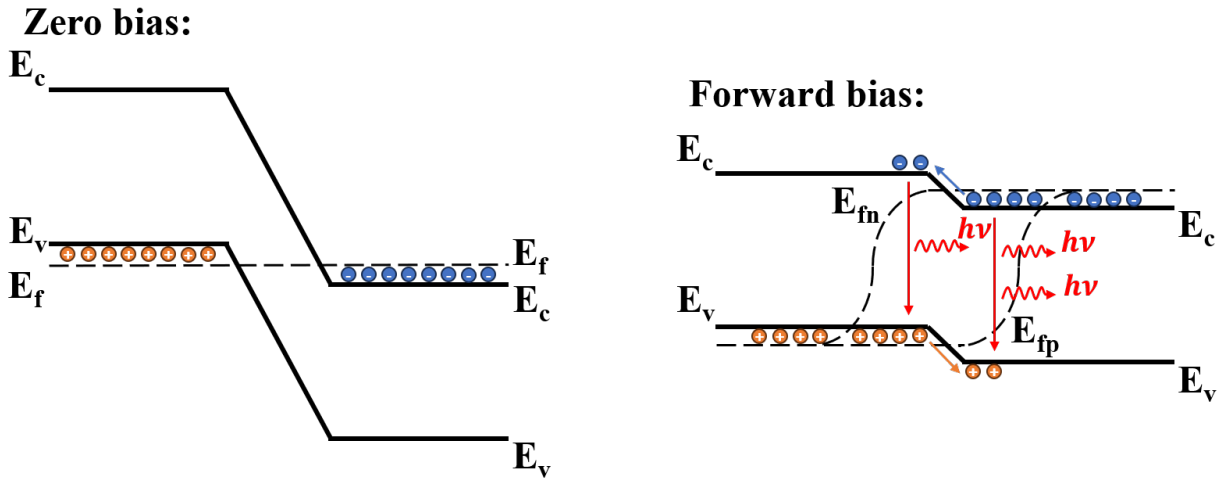
1.1.2 Basic Structures of Diode Lasers

Diode lasers come in two basic types: edge-emitting lasers and surface-emitting lasers. In this dissertation, our focus is on edge-emitting lasers, characterized by light propagation that is parallel to the substrate surface. Early semiconductor diode lasers were homojunction lasers, where the same material (typically a III-V compound with a direct bandgap, such as GaAs) was used for both the heavily doped p-side and n-side of the junction (Figure 1.2a). When a forward bias is applied to the junction, minority carriers are injected into both sides, leading to population inversion within a narrow zone at the junction. In this region, electrons and holes recombine radiatively, generating photons that can trigger stimulated emission. The energy band diagram of the junction without bias and with forward bias is shown in Figure 1.2b. In edge-emitting diode lasers, a Fabry-Pérot cavity is usually employed to ensure coherent light emission. As shown in Figure 1.2a, the lasing medium is placed between two parallel plane mirrors with different reflectivity. In semiconductor lasers, these two mirrors are created by cleaving two ends of the junction and applying anti-reflective (AR) coating and highly-reflective (HR) coating correspondingly. With this configuration, standing waves at specific wavelengths can form within the cavity. When the wave resonates, the cavity provides positive feedback, enabling amplification at the desired wavelength. It is important to note that the selected wavelength is determined by the length of the Fabry-Pérot cavity. Lasing occurs when the total optical gain provided by the lasing medium compensates for the total losses in the cavity for a roundtrip. Therefore, the threshold current of a diode laser is the injection level that the round-trip gain in the laser cavity exceeds the losses (free-carrier absorption, defects scattering and non-radiative transitions, etc). However, the use of homojunction structures in early diode lasers resulted in a significant drawback: extremely high threshold current density, primarily due to poor optical and carrier confinement. As a result, these lasers could only operate in quasi-continuous wave (QCW) mode at room temperature, or in continuous wave (CW) mode at

cryogenic temperatures, which severely limited their practical applications [3].



(a)



(b)

Figure 1.2: a) Schematic of a homojunction diode laser with Fabry-Pérot cavity. b) Band diagram of a homojunction laser under zero bias and forward bias, where E_v represents the valance band, E_c represents the conduction band, E_f represents the Fermi level at equilibrium, E_{fn} and E_{fp} represent quasi-Fermi levels under non-equilibrium conditions.

Nowadays, edge-emitting lasers typically adopt a double-heterostructure configuration, which addresses the limitations of earlier homojunction lasers. In this design, a thin, often undoped or lightly doped, active region is sandwiched by p and n doped cladding layers (Figure 1.4a). The

band gaps of the *p* and *n* doped cladding layers are larger than the band gaps of the active region, as shown in Figure 1.4b. This arrangement ensures electrons and holes are confined within the active region due to the barrier created by the higher-band gap cladding layers. According to Snell's law, this double heterostructure also provides good optical confinement because the refractive index *n* of the higher-bandgap claddings is smaller than that of the active region. Moreover, the bandgaps of the cladding layers are larger, so light generated in the active region will not be absorbed by the claddings. The confinements of both carriers and photons improve the power efficiency of diode lasers and lower the threshold current density by a lot.

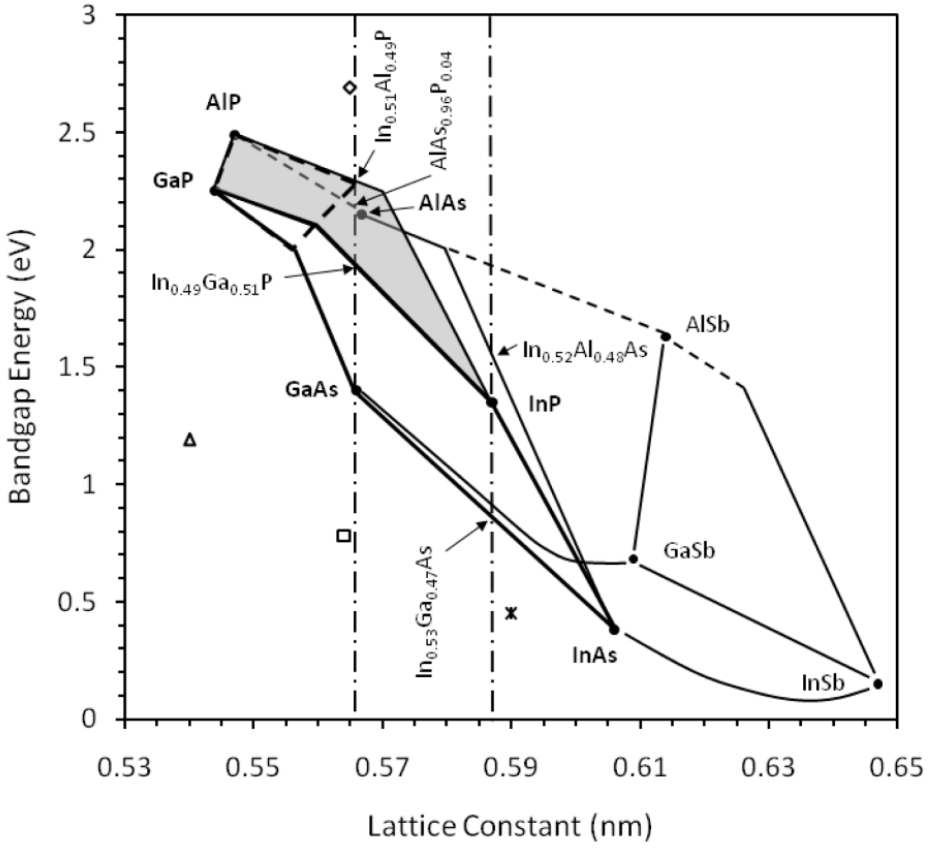
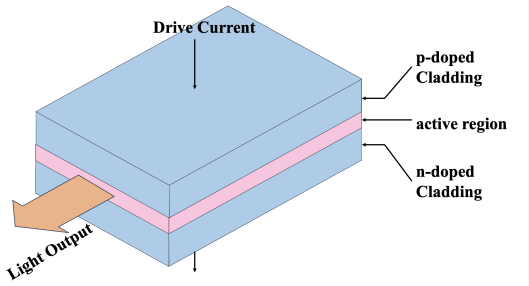


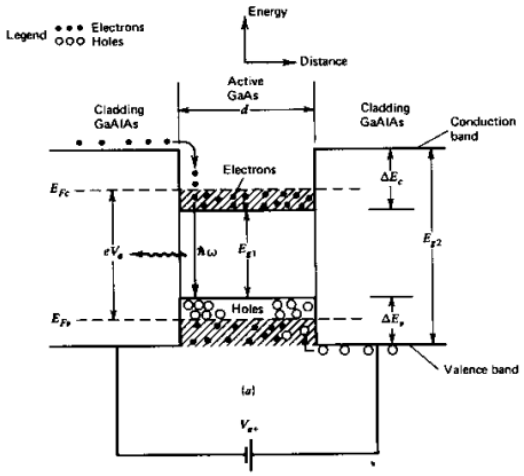
Figure 1.3: Band gap energies and lattice constants of common III–V compound semiconductors used for high-power diode lasers. Compound binaries are represented as solid dots and ternaries as solid lines. Dashed lines represent regions of indirect gap. The two dot–dashed vertical lines show the range of bandgap energies of ternaries and quaternaries that can be grown lattice-matched on the binary substrates GaAs and InP[3].

The double-heterostructure design effectively solves the photon and carrier confinement issues; however, it requires careful material selection to ensure lattice constant matching between layers. A mismatch can lead to misfit dislocations, which acts as non-radiative recombination centers and

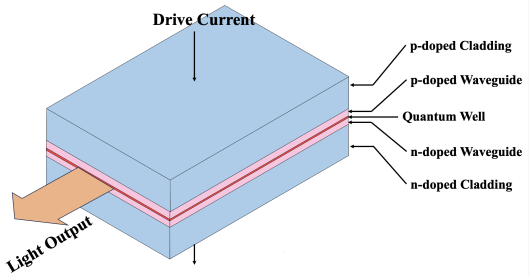
negatively impact the reliability and performance of the laser. Figure 1.3 shows the relationship between energy band gap and lattice constant for common III-V materials used for diode lasers.



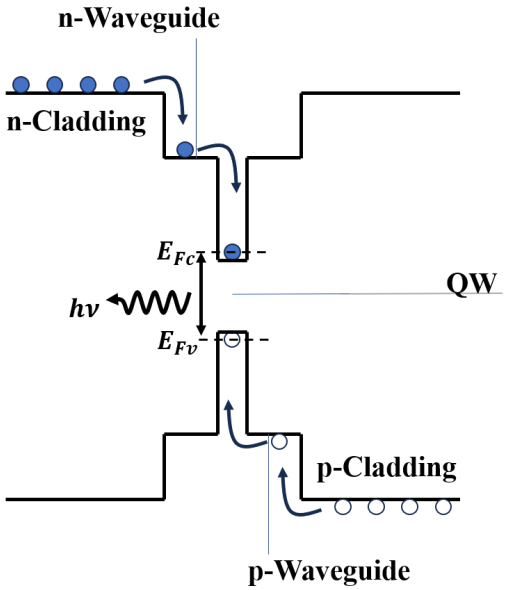
(a) Schemetic of a Double Heterostructure



(b) Band Diagram of a Double Heterostructure [4]



(c) Schemetic of a Separate Confinement Double Heterostructure



(d) Band Diagram of a Separate Confinement Double Heterostructure

Figure 1.4: Regular double heterostructure and separate confinement double heterostructure in diode lasers.

$$E_n - E_c = \frac{\hbar^2 \pi^2}{2m^* L^2} n^2, \qquad n = 1, 2, 3... \tag{1.1}$$

Quantum well (QW) lasers are a special subset of double-heterostructure lasers, in which the active region is made ultra-thin which is comparable to the de Broglie wavelength so that energy levels in the QW are quantized. One notable benefit of QW lasers is their tunable bandgap, achieved by adjusting the thickness of the quantum well (Equation 1.1). In a regular double-heterostructure, the density of states near the band edge is relatively low, while the probability of state occupancy (given by the Fermi-Dirac distribution) is highest at those energies. As a result, the carrier distribution tends to spread over a wide energy range, as illustrated in Figure 1.5, which makes population inversion harder to achieve. In contrast, the step-like DOS in a QW leads to a high density of available states near the band edge, enabling a larger population of carriers concentrated near the edge, which is more favorable for achieving population inversion. However, the ultra-thin active region leads to poor optical confinement. To solve this issue, as shown in Figure 1.4c and 1.4d, one way is to use a separate confinement heterostructure to enhance optical confinement, where the carriers are confined in the QW, while the photons are confined in the waveguide layers. Another point need to be mentioned here is that when the lattice constant of the epitaxial layer and that of the substrate are different, strain will be introduced to the thin epitaxial layer, which will change the band structure and thus change the optical properties of the epi layers.

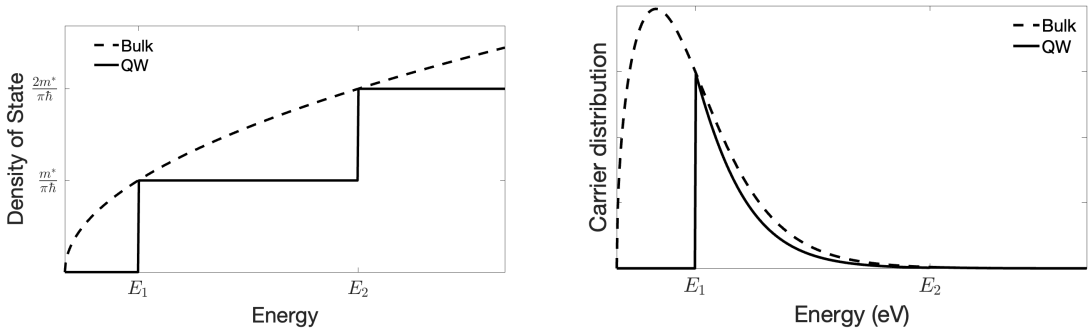


Figure 1.5: a) Density of state in QW and bulk material. b) Carrier distribution in QW and bulk material.

1.1.3 Non-radiative Recombination

In 1.1.1, the concepts of spontaneous emission and stimulated emission were introduced. In both processes, the energy released by electron-hole recombination is converted into photon energy, and thus this type of recombination is referred to as radiative recombination. In addition to radiative recombination, non-radiative recombination processes also occur, where the recombination energy is dissipated as phonons. Non-radiative recombination can be broadly categorized into three main types: surface recombination, defect recombination (also known as Shockley-Read-Hall

recombination), and Auger recombination.

Surface recombination arises from the presence of dangling bonds and bonds associated with foreign atoms, such as oxygen, at the semiconductor surface. These bonds introduce a high density of defect states within the bandgap. These mid-gap defect states significantly enhance the probability of non-radiative recombination, leading to localized heating and a reduction in radiative recombination efficiency.

Defect recombination refers to carrier transitions through mid-gap states introduced by native lattice defects, such as vacancies, interstitials, substitutional impurities, or impurity–vacancy complexes. It is generally believed that the energy released during recombination at these trap states is dissipated via the emission of single or multiple phonons [5]. In fact, Surface recombination is a special case of trap-assisted recombination.

Auger recombination is another important non-radiative recombination mechanism. It is a three-carrier process, in which the energy released from the recombination of an electron–hole pair is transferred to a third carrier, exciting it to a higher energy level within the same band. This excited carrier eventually thermalizes back to the band edge by emitting phonons. Since this process relies on Coulombic collisions with a third carrier, it normally occurs in heavily doped materials, where the carrier concentration is high [5].

1.2 Degradation in Diode Lasers

Since the introduction of diode lasers to the world in the 1960s, their reliability, performance, efficiency, and lifetime have remained paramount concerns. However, these crucial parameters are often constrained by the degradation of diode lasers, which can be classified into three distinct types: rapid degradation, gradual degradation, and catastrophic optical damage (COD) [6][7][8]. Rapid degradation manifests as a swift decline in optical power output within the initial 100 hours of operation for affected devices. Gradual degradation denotes a slow and long process that may occur over the entire lifespan of the device. COD is a fast and sudden process that typically marks the end of a device's lifetime. Figure 1.6 illustrates how devices typically behave when experiencing these degradation modes.

COD can occur either on the laser facet or within the laser cavity. When COD occurs on the laser facet, it is termed catastrophic optical mirror damage (COMD). Typically, COMD results in the localized melting of a region on the facet of the laser's active region (Figure 1.9a), and the damage can extend further into the cavity and form dark line defects (DLDs). On the other hand, when COD occurs within the laser cavity, it is referred to as catastrophic optical bulk damage (COBD). In such cases, DLDs extending from mid-cavity threading dislocations have been observed within the degraded laser cavities (Figure 1.9b).

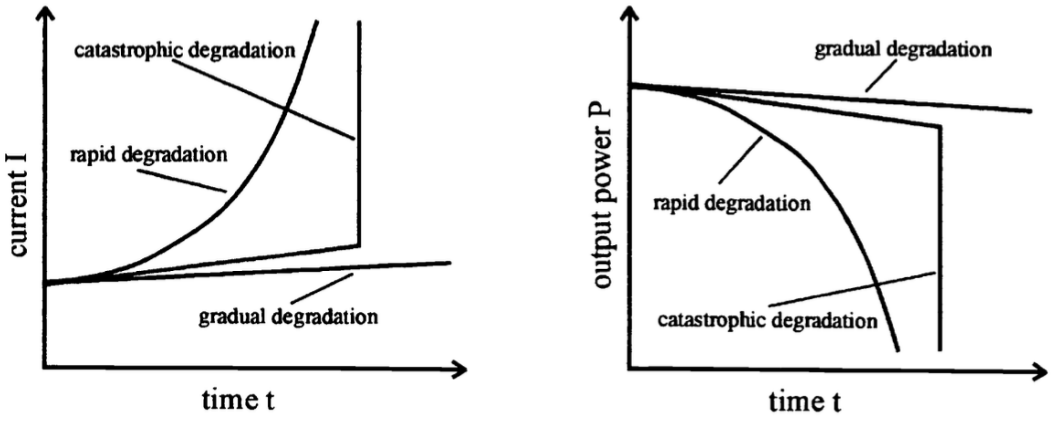


Figure 1.6: Degradation modes in diode lasers at constant a) power output, b) drive current [6].

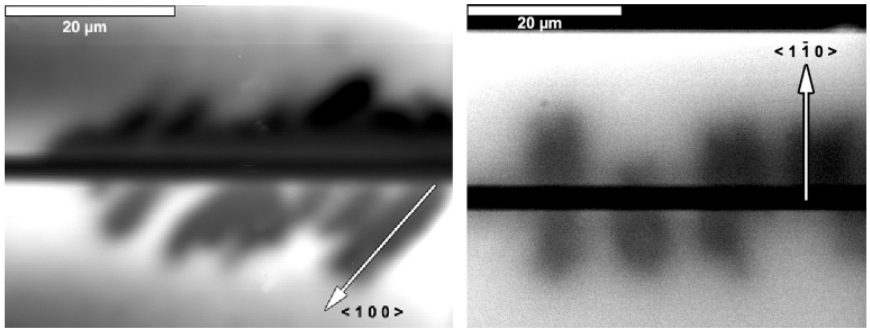
While the aforementioned degradation modes primarily affect the active region, it is worth noting that other parts of the device, such as solder, electrodes, and heat sink bonding, can also experience degradation[6],[7]. However, these additional degradation modes are beyond the scope of interest for this dissertation and will not be discussed.

1.2.1 Rapid Degradation

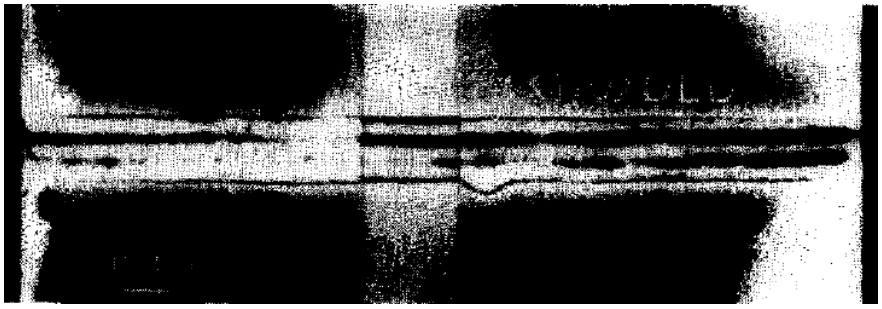
Rapid degradation is often linked to DLDs. These defects either emit minimal light or fail to emit any light at all. DLDs were observed as dark structures using cathodoluminescence (CL) and electron beam induced current (EBIC) techniques, oriented along specific crystallographic directions, typically in $\langle 100 \rangle$ $\langle 110 \rangle$, and occasionally in $\langle 1\bar{1}0 \rangle$ direction, as shown in Figure 1.7a and Figure 1.7b [9][10][11][12][13]. Note that sometimes people do not distinguish between $\langle 110 \rangle$ and $\langle 1\bar{1}0 \rangle$ in the literature. Previous transmission electron microscopy (TEM) analysis shows that DLDs are three-dimensional networks of dislocation loops and helical dipoles, which originate from either threading or misfit dislocations [10][14] (Figure 1.7c). Threading dislocations arise during the crystal growth process, while misfit dislocations are introduced during handling and mounting procedures [14].

Rapid degradation occurs when there is a rapid growth of DLDs. The formation, diffusion, and motion of DLDs are thermally activated processes that generally proceed at a relatively slow rate [14]. However, the presence of non-radiative recombination can significantly accelerate these processes [15], a phenomenon known as recombination enhanced defect reaction (REDR). Two types of dislocation motions contribute to the formation of DLDs: recombination enhanced dislocation climb (REDC), which is responsible for DLDs formation in the $\langle 100 \rangle$, and recombination enhanced

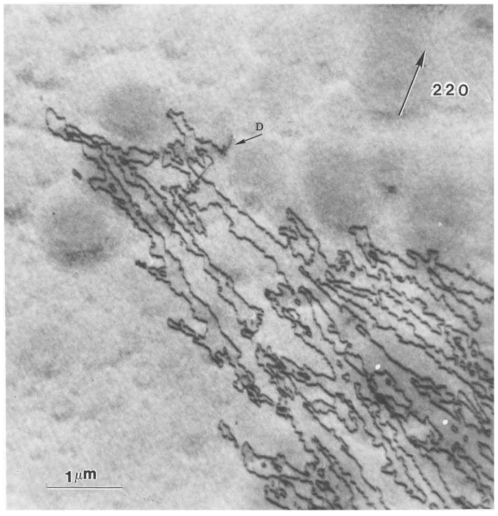
dislocation glide (REDG), which leads to DLDs formation in the ⟨110⟩. Notably, the growth speed of ⟨110⟩ DLDs is slower compared to that of ⟨100⟩ DLDs [14]. More details on REDR will be discussed in the next section.



(a) Panchromatic cathodoluminescence images showing ⟨100⟩ (left) and ⟨ $1\bar{1}0$ ⟩ (right) DLDs in an InGaAs/AlGaAs single mode laser [16].



(b) Electron beam induced current image showing ⟨110⟩ DLDs in a degraded InGaAsP/InP laser [17].

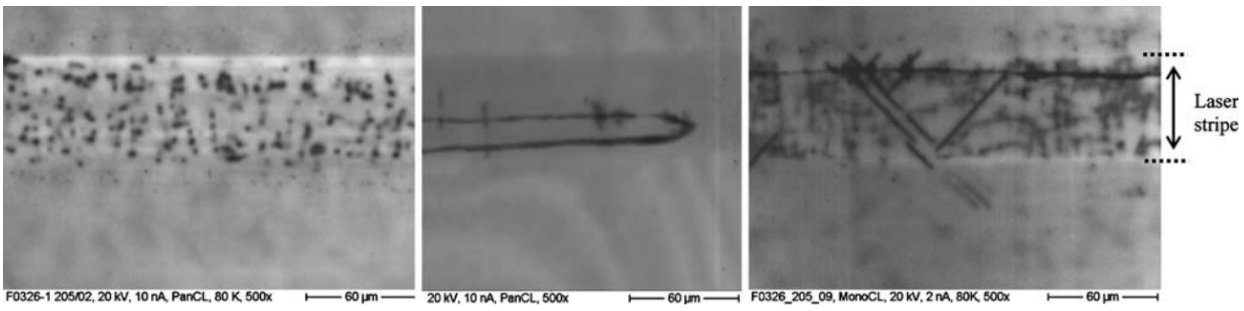


(c) TEM Image of DLDs in a Degraded GaAlAs/GaAs Diode Laser [18]

Figure 1.7: Cathodoluminescence, electron beam induced current and TEM images of DLDs.

1.2.2 Gradual Degradation

Gradual degradation in diode lasers has been attributed to the formation of point defect clusters, the development of dark spot defects (DSDs), and the propagation of DLDs [14][19][20][3][21]. In chapter 3 the relationship between DLDs growth and gradual degradation will be discussed in detail. The formation of point defect clusters and DSDs are correlated with REDR [14][3][22][23]. This process initiates from pre-existing point defect clusters, which act as non-radiative recombination centers. Through REDR, these defects generate additional point defects, which in turn facilitate further recombination events, creating a positive feedback loop. As a result, point defects migrate and condense into dislocation loops, which appear as DSDs These point defect clusters can interact with photons, thereby reducing the laser's optical output. Tomm et al. reported that gradual degradation is associated not only with an increase in point defect density but also with the induction of compressive strain within the laser's active region [24]. Cathodoluminescence images illustrating the effects of gradual degradation on lasers are presented in Figure 1.8. The rate of gradual degradation is affected by internal stress [14][25] and the concentration of deep levels [3][14][26].



(a)

Figure 1.8: Cathodoluminescence images of defects: (left) gradual degradation, (middle) rapid degradation, (right) COD after gradual degradation [19].

Possible approaches to mitigate gradual degradation include suppressing the introduction of deep-level defects during crystal growth and device fabrication, reducing the concentration of residual impurities during epitaxial growth, eliminating internal and external mechanical stress, and preventing the diffusion of metal atoms from electrodes into the active region [3][25].

1.2.3 Catastrophic Optical Damage

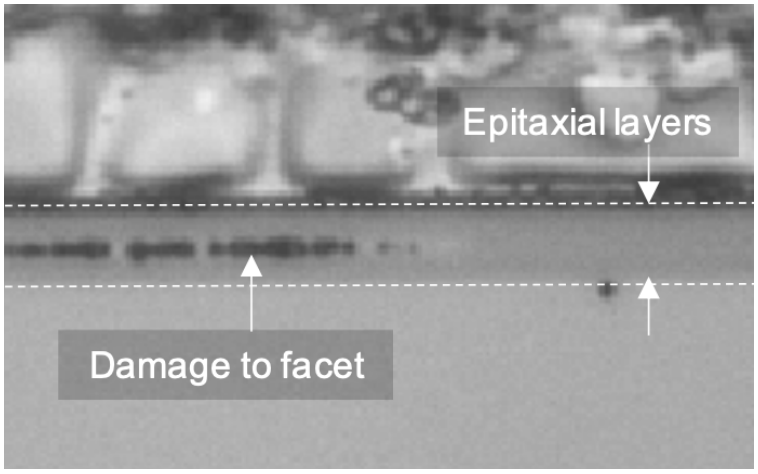
Catastrophic Optical Damage (COD), a rapid and abrupt phenomenon, is initiated by swift thermal runaway, stemming from prolonged temperature increases during laser aging [27][28][29]. Thermal



(b) Cavity EL after COBD [37]

Figure 1.9: Images of diode lasers after two types of COD.

runaway can happen either on the laser facet or in the laser cavity. Tang et al. identified that reaching a critical temperature is necessary to trigger this thermal runaway [30]. The temperature rise can occur on the laser facet due to several reasons, including surface recombination[31], surface current[32], facet oxidation[33], absorption of defects from cleaving[34], and the laser chip's 'overhang' relative to the heatsink[35]. Within the cavity, the absorption by point defect clusters of laser light can also elevate temperature. Once the critical temperature is attained [30], thermal runaway commences, leading to further temperature rises and eventually to COD.



(a) Facet image after COMD [36]

J.W. Tomm et al. and several other authors have dissected the thermal runaway process into two feedback loops (Figure 1.10) [12][29][38][39][40][41]. The intrinsic loop involves the band gap reduction of materials when local temperature reaches the critical temperature, which boosts inter-band absorption of laser light in that region. This results in additional electron-hole pair generation. Even with a steady proportion of these carriers undergoing non-radiative recombination, more heat is produced, perpetuating this intrinsic loop [27]. The extrinsic loop starts with elevated temperatures fostering the accumulation and formation of point defects. These defects act as absorbers, increasing laser light absorption and thus, non-radiative recombination and heat production. These loops can operate simultaneously in a device, culminating in COD. When the temperature in a local

area becomes sufficiently high, it inflicts irreversible damage on the semiconductor material, such as melting on the front facet (Figure 1.9a) and extended DLDs into the cavity (Figure 1.9b). The laser emission power at which COD starts is referred to as COD threshold or P_{COD}. As mentioned previously, COD is a very fast process which could happen within $\sim$ 160 μs [42], as shown in Figure 1.11.

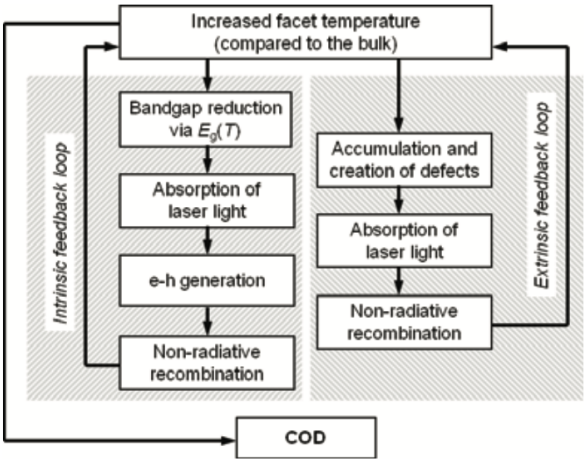


Figure 1.10: Two feedback loops in thermal runaway [38].

Many efforts have been made to prevent COMD from happening since the 1970s. Some well-konwn methods are:

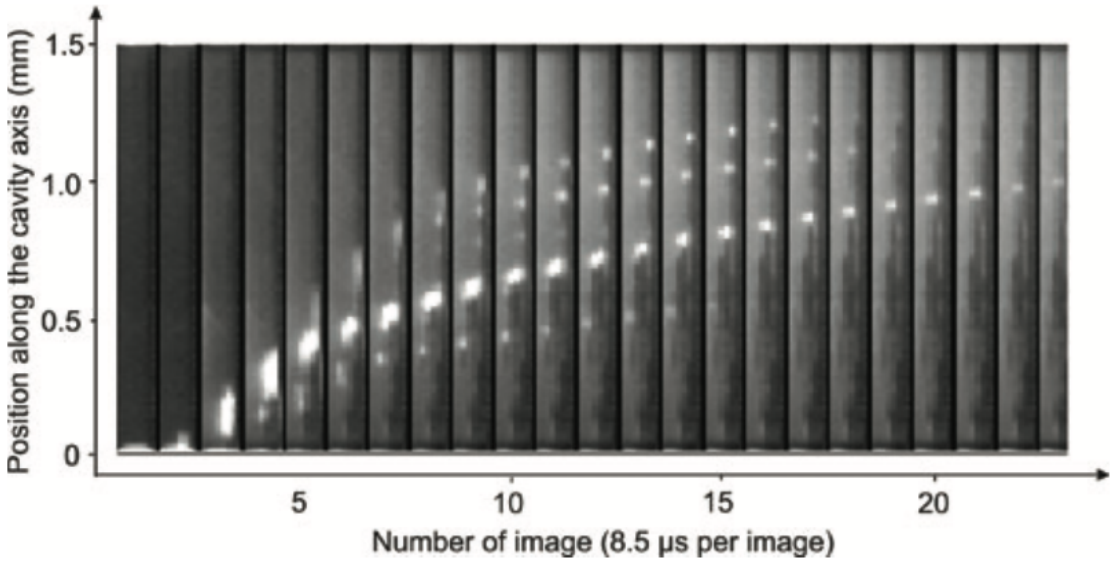


Figure 1.11: Sequential images of the entire COD, each image is 8.5 μs duration [42].

- **Surface passivation:** This technique is a well-established method for mitigating COMD by

reducing surface recombination [3][43], and reducing surface oxidation [44]. Various facet passivation approaches have been employed, including the deposition of barrier laser such as Al_2O_3 [45], Si [46], Al [47], and ZnSe [48]; sulphation treatment [43][49][50], and nitridation treatment [51][52].

- **Non-injecting facets:** This method reduces non-radiative surface recombination and consequently the facet temperature by lowering the current density at the front facet. A commonly used approach to achieve this is by introducing an unpumped (current blocking) region near the facet [40][53][54][55][56].

- **Non-absorbing facets:** This method aims to reduce optical absorption at the facets(a critical component of the thermal runaway feedback loop) by introducing window regions near the facets. These regions have a larger energy bandgap than the cavity's gain region, thereby photons generated in the gain region are not absorbed at the facet, effectively reducing facet heating. Quantum well intermixing techniques, such as selective growth [57][58], etch & regrowth [59][58], impurity-induced disordering (IID) [60][61][62], impurity-free vacancy disordering (IFVD) [63], implantation induced intermixing [64][65], and laser-induced disordering (LID) [66], are well-known ways to achieve this. Other approaches to achieve a larger bandgap include specialized waveguide structure designs [67] [68] and the use of relaxed biaxial tensile strain in the QW near facets [38].

- **Load reduction at facets:** This method reduces the optical power density at the front facet, thereby allowing the device to reach a higher P_{COD}. One approach to accomplish this is through the use of thicker waveguides, such as large optical cavities [69][70], and super-large optical waveguides [71][72]). An alternative strategy involves using regular waveguides in the central cavity region while incorporating widened waveguides near the facets to spread the optical mode and reduce facet loading [67][73].

1.3 Mechanisms of Dark Line Defect Propagation

As previously mentioned, the formation of DLDs is correlated with all three types of degradation in diode lasers. In each case, DLDs appear as regions of reduced emission. However, the nature of DLDs formed during COD differs from those generated during gradual and rapid degradation. In this section, we discuss the distinct propagation mechanisms associated with these two types of DLDs.

1.3.1 Dark Line Defect Propagation during COD

The entire COD process is broadly divided into three phases by Tomm [38], as shown in Figure 1.12. In the first phase, a localized region reaches the critical temperature necessary to initiate thermal runaway. The time required to reach this temperature can range from as little as 10 ns to several thousand hours, depending on factors such as facet protection and emission power density [38][74][75]. For example, a laser with a well-passivated facet operating at low current in CW mode may take over 1000 hours to reach the critical temperature (i.e. gradual degradation). In contrast, a laser with no facet protection driven at very high current may reach the critical temperature in as little as 10 ns.

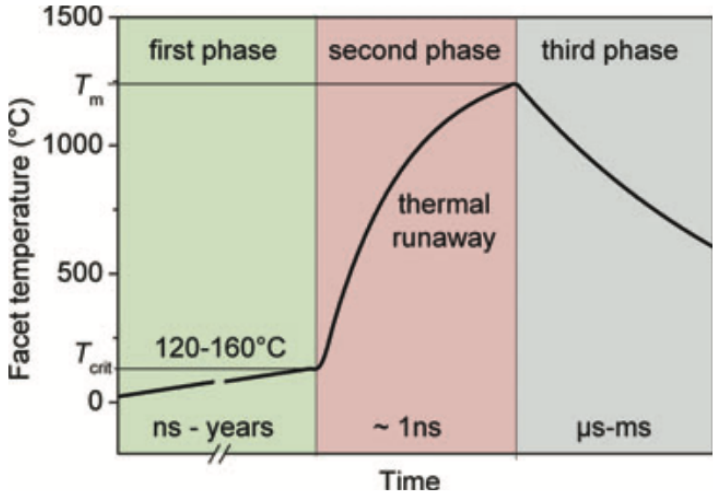


Figure 1.12: Schematic of the sequence of events during COD. Note that the temperature indicated on the y-axis does not necessarily correspond to hot spots on the facet; it can also represent hotspots located within the laser cavity [38].

The onset of thermal runaway marks the beginning of the second phase of the COD process. During this phase, the temperature at a localized spot increases rapidly, driven by the positive feedback loops described in 1.2.3, ultimately leading to localized melting. This phase has not yet been directly observed experimentally, as the process occurs too quickly to be resolved. However, model calculations suggest that this phase unfolds within a timescale of approximately 1 ns [38]. The thermal runaway process terminates when the laser emission sustaining it is substantially reduced due to the structural damage, thereby interrupting the feedback loop [76].

In the third phase, additional damage continues to develop, as the input current is typically not abruptly terminated. The DLDs (or dark bands), commonly observed in CL maps of post-COD devices, are formed during this phase. The propagation of these DLDs generally occurs over a timescale of microseconds to milliseconds. Jacob et al. observed the complete propagation process,

which lasted approximately 160 μs, as shown in Figure 1.11 [42]. The propagation velocity of DLDs following thermal runaway has been reported to range from 1-20 m/s [42][76][77][78][79][80][81]. These DLDs, generated during COD, typically consist of polycrystalline regions surrounded by dense dislocation networks [82][83][84]. The kinetics of the DLDs propagation can be described as follows: the molten region, initially formed by thermal runaway, propagates along the lasing axis with the absorption of laser light serving as the primary driving force. Owing to the very high absorption coefficient of the molten material, the melton region propagation direction is governed by the propagation direction of the optical mode rather than thecrystallographic orientation [83][85]. As the molten region propagates, the previously molten area rapidly quenches and recrystallizes with a large number of dislocation networks generated around the recrystallized region to compensate for the volume change during the liquid-to-solid phase transition [78][76]. However, it remains unclear whether the original melting temperature must be reached for continued propagation [38]. Snydar et al. suggested that propagation could occur at a lower temperature, assuming the molten region formed during thermal runaway is metal-rich [86]. In such cases, the increased electrical conductivity of the metal-rich zone could form an electrical bridge across the junction, leading to enhanced Joule heating, which provides additional energy to sustain the molten zone motion.

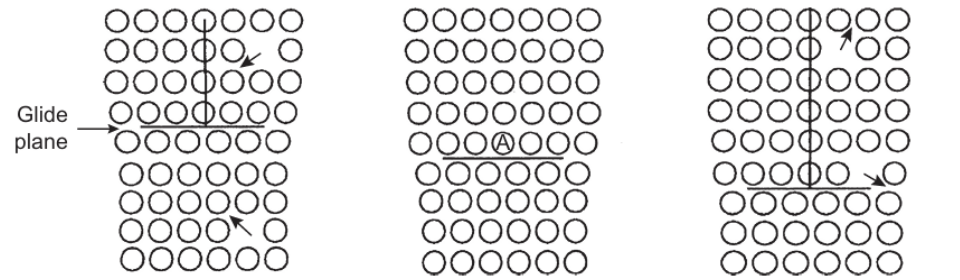
1.3.2 Dark Line Defect Propagation during Rapid and Gradual Degradation

Unlike the super fast propagation of DLDs observed during COD, DLDs propagation during rapid and gradual degradation occurs at a much slower velocity. Moreover, the nature of this propagation is fundamentally different. It is governed by dislocation climb and glide motions, rather than the motion of a molten region.

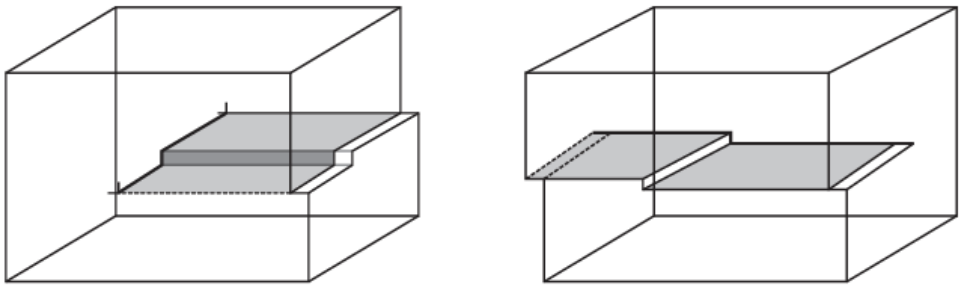
1.3.2.1 Dislocation Climb and Dislocation Glide

Dislocation climb occurs perpendicular to the slip (glide) plane, which is defined by the dislocation line and the Burgers vector. This motion requires interaction with vacancies in the crystal lattice. The emission or absorption of vacancies drives dislocation climb in opposite directions, as illustrated in Figure 1.13a. While dislocation climb may appear to involve the addition or removal of an entire row of atoms in Figure 1.13a, in reality, it proceeds through the formation of discrete steps known as jogs. A jog represents the smallest unit of climb, a localized step formed when a segment of the dislocation line moves out of the glide plane (Figure 1.13b).

Dislocation glide occurs within the slip (glide) plane. Unlike dislocation climb, glide motion does not require interaction with vacancies. Instead, the dislocation line moves within the slip plane, driven by applied shear stress, as illustrated in Figure 1.14a. Similar to climb, glide proceeds through discrete steps known as kinks, which represent localized segments of the dislocation line



(a)



(b)

Figure 1.13: Illustration of a) the climb motion of an edge dislocation, b) jogs that form the climb motion of a edge dislocation (left) and a screw dislocation (right) [87].

shifting in the glide plane (Figure 1.14b). The high-power diode lasers discussed in this dissertation are composed of III–V compound semiconductors with a zinc blende crystal structure. The slip plane is typically the plane with the highest atomic density; in III–V semiconductors, this is usually the (111) plane.

1.3.2.2 Recombination Enhanced Dislocation Motion

In diode lasers, the injection of minority carriers enhances both dislocation glide and dislocation climb. This enhancement is explained by the REDR mechanism, proposed by Weeks et al. [88]. In devices grown on the (001) crystallographic plane, two primary types of DLDs are commonly observed: $\langle 100 \rangle$ DLDs and $\langle 110 \rangle$ DLDs.

In devices with emitting stripe aligned along the $\langle 1\bar{1}0 \rangle$ direction, $\langle 100 \rangle$ DLDs are the result from complex dislocation networks formed by REDC. Previous studies have shown that the Burgers vector of $\langle 100 \rangle$ DLDs is $a/2\langle 011 \rangle$ [89]. These dislocation networks originate from threading dislocations in the substrate or stacking faults introduced during epitaxial layer growth [12]. When observed from the direction perpendicular to the (001) junction plane, the threading dislocation initially appears as a small dark spot. As the device undergoes aging, a dislocation dipole forms

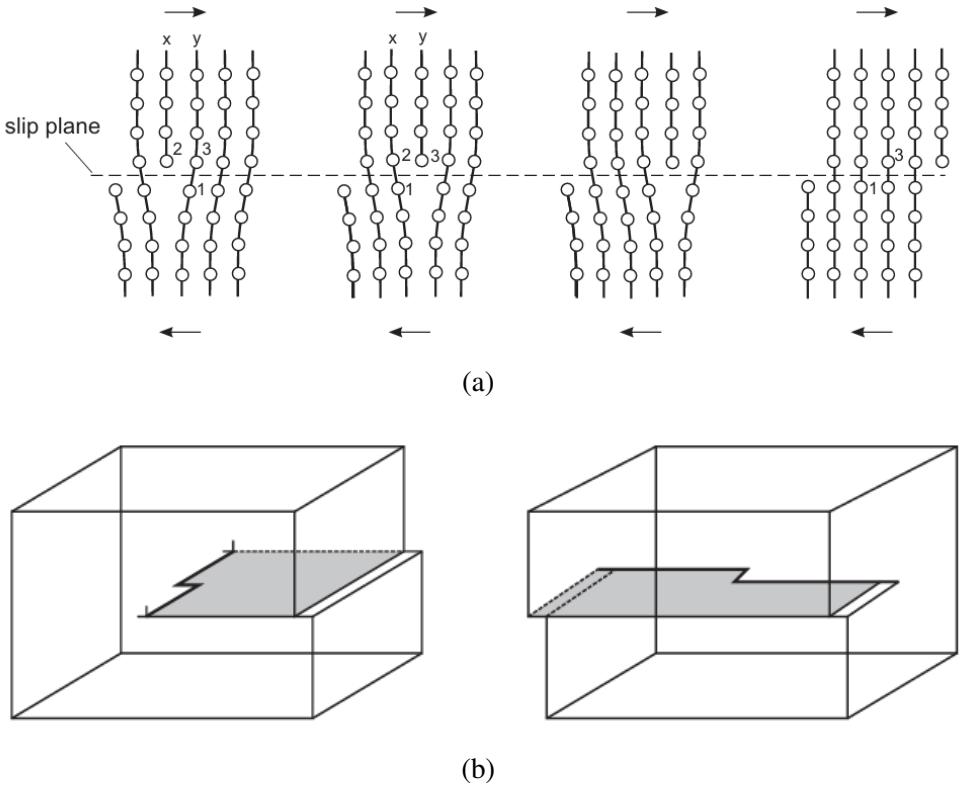


Figure 1.14: Illustration of a) the glide motion of an edge dislocation (arrows indicate the applied shear stress), b) kinks that form the glide motion of a edge dislocation (left) and a screw dislocation (right) [87].

via REDC from a segment of the threading dislocation, appearing as a larger dark spot in the (001) plane. With continued aging, dislocation climb in the $(0\bar{1}1)$ plane results in a complicated dislocation networks that project as a dark line propagating along the $\langle 100 \rangle$ in the (001) junction plane [90][12]. This $\langle 100 \rangle$ dark line is oriented at a 45° angle relative to the cavity direction, as shown in Figure 1.15. The propagation of DLDs can be mitigated by eliminating dislocation sources. This can be achieved by, for example, using substrates with low dislocation density [12], and performing epitaxial growth in a clean atmosphere with high-purity source materials [91]. Another method involves adding indium to the QW [92][93][94]; however, this method is effective only for GaAs-based QW, and is not applicable for InGaP or InGaAsP QWs.

On the other hand, $\langle 110 \rangle$ DLDs result from straight dislocation lines gliding in the (111) glide plane [95], whose projection onto the (001) junction lies along the $\langle 110 \rangle$ direction. These dislocations have been identified as stacking faults, misfit dislocations, and partial dislocation loops, which are typically induced by factors such as substrate contamination, mechanical damage, and stress introduced during fabrication [12][95][96][97]. Therefore, suppressing $\langle 110 \rangle$ DLDs is primarily linked to reducing mechanical stress during fabrication. One approach is to reduce

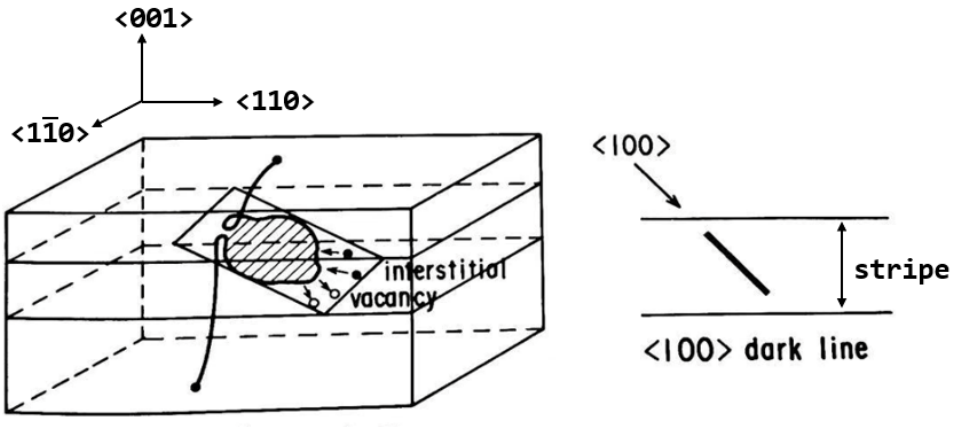


Figure 1.15: Elongation process of ⟨100⟩ DLDs [12].

bonding stress by using soft solder materials, such as In or Sn, which help to compensate for the thermal expansion mismatch between the laser chip and the heat sink [98]. However, soft solder materials may degrade over long-term aging, potentially compromising device reliability [12].

The propagation velocity of ⟨100⟩ and ⟨110⟩ DLDs is dependent on many factors and the value can vary between 0.01 μm/h to 1000 μm/h [99], both of which are much smaller than the propagation velocity of the dark band during COD. Previous studies have identified several extrinsic factors that affect the propagation velocities of ⟨100⟩ and ⟨110⟩ DLDs. It has been demonstrated that the DLD growth rate in laser diodes is linearly dependent on injected current density below threshold in diode laser devices [99][100][101]. While defect velocity and growth rate in a bulk material scales with the intensity of external excitation (such as laser beams or electron beams) [102][103][104]. Other key extrinsic factors affecting DLDs propagation velocity in bulk materials include test temperature and mechanical stress [103][104][102][105][28]. Some intrinsic factors that influence defect propagation velocity include doping type and material composition [104][102]. Details about the mechanisms behind REDR will be discussed in chapter 4.

1.4 Defect Characterization Methods for Diode Lasers

Numerous methods have been employed previously to characterize defects in diode lasers. This section will categorize them into destructive and non-destructive methods, which will be introduced individually.

1.4.1 Destructive Methods

1.4.1.1 Cathodoluminescence

Cathodoluminescence (CL) refers to the phenomenon where light is emitted by a material upon exposure to an electron beam, with energies ranging from 0.5 keV to 300 keV [106]. The irradiating electron beam's small spot size, just a few nanometers wide, allows CL to achieve excellent spatial resolution, down to tens of nanometers. This high resolution is particularly beneficial for characterizing defects in diode lasers [107]. However, the technique is usually applied to lasers that have already degraded. The technique is generally non-destructive at low beam currents; however, destructive sample preparations are required to expose the active region in the device interior (far from the facets) [16][108][109].

1.4.1.2 Transmission Electron Microscopy

Transmission Electron Microscopy (TEM) is a technique that distinguishes itself from CL by utilizing a high-energy electron beam capable of passing through the specimen. This passage allows some electrons to carry structural information of the specimen, which is then projected onto a fluorescent screen to create an electron image. The resolution of TEM is significantly influenced by the De Broglie wavelength of electrons, which is inversely proportional to the electron beam's applied accelerating voltage. Consequently, TEM's theoretical resolution can reach up to 0.3 nm [110], making it exceptionally suited for identifying the intricate structures of defects within diode lasers [18][111]. However, similar to CL, TEM is applied to lasers that have already degraded. This limitation arises because the high-energy electron beam may damage the laser's crystal structure. Additionally, specific preparations on the device are necessary before conducting TEM analysis, a process detailed in the work of Ruvimov et al. [111].

1.4.1.3 Atomic Force Microscopy

Atomic force microscopy (AFM) is not typically associated with defect characterization in diode lasers, yet it has been utilized to study v-defects in GaN-based LEDs [112] and, through its variant conductive atomic force microscopy (C-AFM), to investigate dislocations serving as current leakage pathways in GaN materials [113]. AFM measures the topographic features of a sample with a highly sensitive cantilever mounted on a piezoelectric scanner. The cantilever tip, adorned with atoms, hovers close to the sample surface. The repulsive forces between the tip atoms and the sample cause the cantilever to deflect and oscillate. Recording these deflections allows for the capture of precise topographical data. In contrast, C-AFM maintains direct contact between the tip and the sample surface. This mode enables the application of a voltage bias across the sample

and cantilever, facilitating the measurement of electrical current at each point of contact. This technique is particularly useful for mapping electrical conductivity variations across the sample surface, offering valuable insights into the electrical behavior of defects.

1.4.2 Non-destructive Methods

As many defect-related processes result in the generation of heat, thermal characterization offers an alternative approach to defect characterization.

1.4.2.1 Raman Spectroscopy

Raman Spectroscopy is a technique that exploits the inelastic scattering of photons by vibrational molecules or crystal lattices. Interactions between photons and matter include absorption, transmission, and scattering [114]. In absorption, the energy of the photon must align with the energy gap between two real electron states. Scattering, however, allows for the photon energy to be less than this energy gap, leading to the excitation of the electron to a transient virtual state. This excited electron swiftly returns to a stable state, during which a photon is emitted.

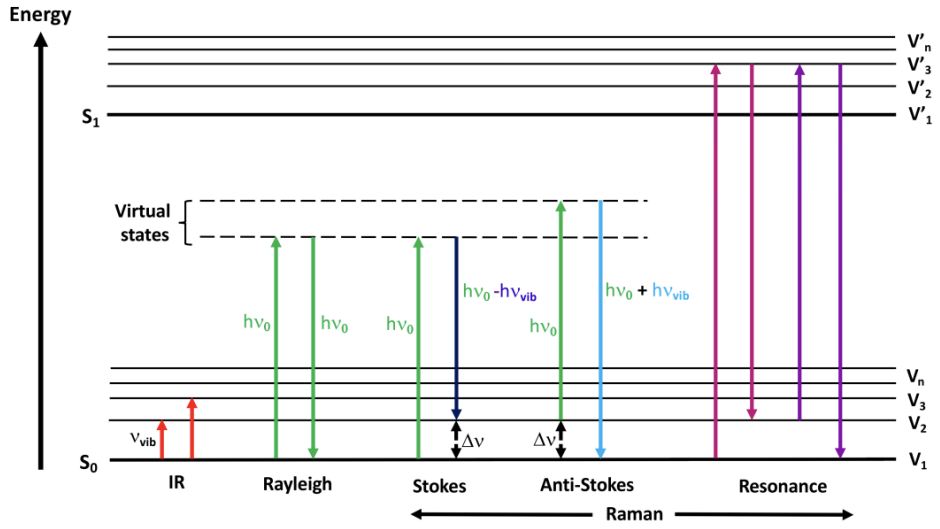


Figure 1.16: Energy diagram of photon matter scattering [115].

As shown in Figure 1.16, the process whereby an electron returns to its original state and emits a photon with the same wavelength as the incident photon is known as Rayleigh scattering. Alternatively, when the electron relaxes back to a state of higher energy than its initial state, the emitted photon exhibits a longer wavelength than the original, a phenomenon referred to as Stokes scattering. In contrast, anti-Stokes scattering occurs when the electron moves to a lower energy state than its original, resulting in the emission of a photon with a shorter wavelength than

that of the incoming photon. Stokes and anti-Stokes scattering are key processes harnessed in Raman spectroscopy to reveal vibrational, rotational, and other low-frequency modes in a system. Furthermore, when the energy of the incoming photon suffices to excite the electron to a real energy state rather than a virtual one, the process is termed Resonance scattering, which is the basis of Resonance Raman spectroscopy.

Measuring temperature via Raman spectroscopy can be achieved in two primary ways. Firstly, by monitoring the shift in the position of the Raman peak [38]. This shift occurs because temperature changes affect the lattice constant of a material, which in turn alters its vibrational modes, leading to a change in the Raman peak position. Secondly, the intensities of the Stokes and anti-Stokes peaks can be analyzed, a method grounded in Bose-Einstein statistics [116]. In Raman spectroscopy, the intensity of a peak reflects the density of phonons in a specific vibrational mode. Therefore, the ratio between the intensities of Stokes and anti-Stokes peaks serves as a function of temperature, alongside the photon and phonon frequencies, as illustrated in equation 1.2.

$$\frac{I_{AS}}{I_S} = (\frac{\nu_L + \nu_V}{\nu_L - \nu_V})^4 exp(\frac{-\hbar\nu_V}{k_B T}) \tag{1.2}$$

where I_{AS} and I_S are intensities of anti-Stokes scattering and Stokes scattering correspondingly, ν_L is the frequency of the incoming photon, ν_V is the frequency of phonon (vibrational mode), and T is the temperature.

The spatial resolution of micro-Raman spectroscopy, which is usually used in the thermal characterization of diode laser facet [33][117][118][119], can achieve approximately 1 μm, primarily constrained by the diffraction limit of the irradiating light [120]. While Raman spectroscopy is generally regarded as non-invasive, the concentration of high-energy laser light onto a small area can still cause heating and potential damage to the sample[116]. Also, heating on the sample surface will lead to measurement error, which limits the temperature resolution of this technique. This localized heating can also introduce measurement inaccuracies. Another limitation of Raman spectroscopy is its point-based analysis approach. This means it can only produce discrete data points across a 2-D surface, rather than a continuous 2-D profile, which may restrict its applicability in providing comprehensive surface characterization.

1.4.2.2 Infrared Radiation Thermometry

Infrared Radiation Thermometry stands out as a widely recognized technique for measuring temperature. It has also been used in the thermal characterization of diode lasers under some circumstances [121][109]. This method determines an object's temperature by quantifying its emitted thermal radiation. All matter with a temperature above absolute zero emits electromagnetic waves. The power of this emission per unit area is linked to the object's emissivity and its temperature, as

described by equation 1.3.

$$E_{thermal} = \epsilon \int_0^\infty \frac{2\pi hc^2}{\lambda^5(exp(\frac{hc}{\lambda k_B T}) - 1)} d\lambda \\ = \epsilon\sigma T^4 \tag{1.3}$$

where ϵ is the emissivity of the surface, h is the Planck's constant, c is the speed of light in vacuum, and σ is the Stefan-Boltzmann constant.

In practical applications, while infrared radiation thermometry offers a rapid and non-invasive approach to thermal characterization, it faces several significant limitations. A primary challenge is the calibration of surface emissivity, which varies with the surface's composition, roughness, and the viewing angle [122]. Additionally, the absorbtivity of the medium between the object's surface and the sensor needs meticulous calibration. Moreover, according to Wien's displacement law, the wavelength of light that predominates at room temperature is more than 5 μm (equation 1.4), limiting the spatial resolution of infrared radiation thermometry. This resolution constraint restricts its effectiveness in resolving finer thermal details or gradients within the laser structure. So, its primary application is to measure the bulk temperature of diode lasers.

$$\lambda_{max} = \frac{b}{T} \tag{1.4}$$

where b is Wien's displacement constant.

1.4.2.3 Thermoreflectance Microscopy

Thermoreflectance (TR) microscopy is a well-established non-contact temperature measurement technique that is based on the impact of temperature on the reflectivity of a reflective surface. Since Epperlein et al. applied this technique to the thermal characterization of diode laser facet [123][117], it has been widely used for thermal characterization of different kinds of small-scale electronics [124][125][126][127][128]. Details of this technique will be illustrated in chapter 2.

1.4.2.4 Other Techniques

Other techniques have been employed to characterize defects in diode lasers alongside those previously mentioned. For instance, photonluminescence (PL) spectroscopy offers a temperature resolution of approximately 1K and a spatial resolution around 1 μm, making it a valuable tool for measuring local temperatures within the laser structure [129]. Additionally, laser beam induced current (LBIC) is utilized to determine defect densities by assessing the local current flow induced by photon interaction [23].

1.5 Defect Characterization Methods used in this Dissertation

In this dissertation, the foremost objective is to characterize the defect evolution process in diode lasers, necessitating repeated measurements from the onset of their operational life through to several hundred hours post-aging or until their end of life. To achieve this, the chosen characterization methods must be non-destructive, ensuring that the laser remains unharmed during defect characterization. Additionally, these methods must offer a high resolution alongside the capability for 2D profiling to accurately pinpoint the exact location and intricacies of defects. As previously discussed, defect formation and growth can occur both on the laser facet and within its cavity. Therefore, to comprehensively understand the defect evolution in diode lasers, it is essential to conduct measurements in both areas.

For defect characterization on the laser facet, thermoreflectance TR microscopy was chosen due to its non-destructive nature, relatively high resolution, and capability for 2D profiling. This makes it arguably the most appropriate method for examining the delicate laser facet throughout the aging process. For defect characterization within the cavity, none of the previously mentioned techniques are applicable. However, for characterizing defects within the cavity, the methods previously discussed are not suitable. Unlike the approach for facet measurement, a technique for examining the cavity's active region must also penetrate a 150 μm thick substrate. While thermoreflectance microscopy initially seemed like an optimal choice, its effectiveness is compromised by a broadband near infrared (NIR) emission from the laser cavity itself, which overwhelms the TR signal. Consequently, a novel technique that leverages this broadband NIR emission from the cavity has been developed specifically for analyzing defect evolution within laser cavities. The details of this new method and its application will be elaborated upon in chapter 3.

CHAPTER 2

Temperature Profiling of a High-Power Diode Laser Facet During Aging

2.1 Physics Behind Thermoreflectance

As described in Chapter 1, Thermoreflectance TR microscopy is a non-contact, non-destructive temperature measurement technique. The basis of this technique is that the band structure of a material changes with a temperature variation. The temperature increase of a material will lead to a shift in the band gap energy, as shown in equation 2.1:

$$E_g = E_0 - \frac{\alpha T^2}{T + \beta} \tag{2.1}$$

where E_g is the band gap, E_0 is the band gap at 0K, α and β are constants that depends on the material [130]. Then based on the empirical relation in equation 2.2, which was proposed by T.S. Moss [131].

$$n^4 E_g = constant \tag{2.2}$$

A perturbation of the temperature of a sample will lead to a change in its refractive index n. Then, according to the Fresnel equation, when light is normally incident to a surface from the air, the relationship between the reflectance and the refractive index is shown in equation 2.3. The change of the temperature eventually leads to the change of the reflectance of the surface.

$$R = \left| \frac{n-1}{n+1} \right|^2 \tag{2.3}$$

A more rigorous explanation of this phenomenon involves the study of the complex dielectric function shown in equation 2.4 [126][7]. Here, we provide a theoretical derivation of the relationship between temperature change and reflectance change. It is important to note that, in practical

applications, the coefficient in this relationship typically cannot be determined analytically and instead requires careful experimental calibration.

$$\hat{\varepsilon}(E) = \varepsilon_1(E) + i\varepsilon_2(E) \tag{2.4}$$

Based on Maxwell's equation real and complex parts of this dielectric function can be expressed in terms of the refractive index n and the extinction coefficient k, which are the real and imaginary parts of the complex refractive index $\hat{n} = n + ik$, as in equation 2.5:

$$\begin{aligned} \varepsilon_1 &= n^2 - k^2 \\ \varepsilon_2 &= 2nk \end{aligned} \tag{2.5}$$

Solving equation 2.5, one write the refractive index n and the extinction coefficient k in terms of ε_1 and ε_2, as in equation 2.6.

$$\begin{aligned} n &= \left(\frac{(\varepsilon_1^2 + \varepsilon_2^2)^{\frac{1}{2}} + \varepsilon_1}{2} \right)^{\frac{1}{2}} \\ k &= \left(\frac{(\varepsilon_1^2 + \varepsilon_2^2)^{\frac{1}{2}} - \varepsilon_1}{2} \right)^{\frac{1}{2}} \end{aligned} \tag{2.6}$$

The reflectance R of a material has the form in equation 2.7

$$R = \frac{(n-1)^2 + k^2}{(n+1)^2 + k^2} \tag{2.7}$$

In thermoreflectance microscopy, the relative reflectance ($\frac{\Delta R}{R}$) is measured. And $\frac{\Delta R}{R}$ can be calculated by differentiating equation 2.7:

$$\frac{\Delta R}{R} = \frac{4(n^2 - k^2 - 1)\Delta n + 8nk\Delta k}{((n+1)^2 + k^2)((n+-1)^2 + k^2)} \tag{2.8}$$

where Δn and Δk are the changes of n and k, which is induced by the change of temperature. After plugging equation 2.6 into equation 2.8, equation 2.9 is yielded.

$$\frac{\Delta R}{R} = \alpha\Delta\varepsilon_1 + \beta\Delta\varepsilon_2 \tag{2.9}$$

with

$$\begin{aligned} \alpha &= \frac{2A}{A^2 + B^2} \\ \beta &= \frac{2B}{A^2 + B^2} \end{aligned} \tag{2.10}$$

where

$$\begin{aligned} A &= n(n^2 - 3k^2 - 1) \\ B &= k(3n^2 - k^2 - 1) \end{aligned} \tag{2.11}$$

It has been found that when temperature increases, the energy gap will shift and so will the band structure broaden [132]. Considering both effects, $\Delta\hat{\varepsilon}$ can be written in forms of equation 2.12

$$\Delta\hat{\varepsilon} = \frac{d\hat{\varepsilon}}{dE_g}\frac{dE_g}{dT}\Delta T + \frac{d\hat{\varepsilon}}{d\Gamma}\frac{d\Gamma}{dT}\Delta T \tag{2.12}$$

where Γ is the broadening parameter. The broadening effect is negligible, comparing to the total shift [132]. So we can assume that $\frac{d\Gamma}{dT} = 0$, which makes the modulation of reflectance a first-order modulation in equation 2.13.

$$\frac{\Delta R}{R} = \left(\frac{1}{R}\frac{\partial R}{\partial T}\right)\Delta T = \kappa\Delta T \tag{2.13}$$

where κ is the thermoreflectance coefficient (TRC) whose value is typically of the order of $10^{-2} - 10^{-5}K^{-1}$. In our application, this coefficient depends on the material property of the reflective surface, the geometry of the multilayer surface, the wavelength of irradiating light, and the optical property of the experimental setup. And as mentioned above, a careful experimental calibration is needed to find the value of the coefficient because it is crucial in the conversion of relative reflectance change and temperature change.

2.2 CCD-based Thermoreflectance

Thermoreflectance techniques can be distinguished both by how the data is acquired, through point-by-point scanning or CCD-based imaging, and by whether they target transient or steady-state thermal behavior. [133][134].In the point-based approach, a laser beam serves as the illumination source, targeting specific points on the surface. The reflected light from these points is then captured by a highly sensitive photodiode, coupled with a lock-in amplifier, allowing the detection of changes in reflectivity less than $\Delta R/R = 10^{-6}$. Due to the high sensitivity of photodiodes, point-based measurement approaches often exhibit a relatively superior signal-to-noise ratio. However, this technique is notably time-consuming and lacks the capability for 2D profiling; acquiring a 500 x 500 pixel image can take up to an hour [126]. Several approaches have been employed to reduce acquisition time while maintaining high sensitivity. One method involves using a photodiode array with synchronous multi-point bandwidth filtering [133], while another utilizes dual galvanometric mirrors to rapidly scan the device under test [135]. The former approach can acquire a spatially

resolved thermal image within minutes, achieving a temperature resolution of 10 mK. However, the resulting image contains only 16×16 pixels, significantly fewer than what is typically provided by a standard CCD [126][136]. The latter approach can achieve a spatial resolution of approximately 300 nm, but the high temperature modulation frequency required may limit the amplitude of temperature modulation [126].

In the CCD-based approach, an LED serves as the illumination source, with its incoherent light focused onto the sample by an objective lens. The light reflected from the sample surface, modulated by surface temperature changes, is captured by a CCD camera. This data is then processed to generate a 2D temperature profile of the surface. The spatial resolution of this method is affected by the wavelength of the illumination LED. However, opting for a shorter wavelength isn't always advantageous for thermoreflectance measurements; to achieve an optimal signal-to-noise ratio, dR/dT for the specific sample at the chosen illumination wavelength must be maximized.

In this dissertation, we want to measure the temperature change of a laser facet when operating in comparison with not operating. Therefore CCD-based thermoreflectance microscopy is used. The temperature modulation is induced by the modulation of the laser drive current, which is phase-locked to the CCD-frame trigger. Assume the modulation signal is a sinusoidal function with period T, and the modulation frequency be f, the reflectance can be written as:

$$R(x, y, t) = R_0(x, y, t) + \frac{\Delta R(x, y, t)}{2} cos(2\pi f t + \varphi(x, y) + \psi) \tag{2.14}$$

where R_0 is the time-independent background reflectance, $\frac{\Delta R}{2}$ is the amplitude of the small modulation, $\varphi(x, y)$ is the phase shift due to thermal modulation and ψ is an arbitrary uniform phase shift accounting for any overall delay between the modulation signal and the camera trigger [134]. Note that the modulation term in Equation 2.14 is not limited to sinusoidal signals; in this dissertation, for example, a square wave is employed. In a 4-bucket scheme, which is mostly used, the camera is triggered at $f_c = 4f$. So that four images are taken in one period T of the temperature (current) modulation: two images when the laser is on and two images when the laser is off (Figure 2.1). The intensities of these four images can be represented by four integrals (equation 2.15) [137].

$$\begin{aligned} I_1 &= \int_0^{\frac{T}{4}} R(x, y, t)dt & I_2 &= \int_{\frac{T}{4}}^{\frac{T}{2}} R(x, y, t)dt \\ I_3 &= \int_{\frac{T}{2}}^{\frac{3T}{4}} R(x, y, t)dt & I_2 &= \int_{\frac{3T}{4}}^{T} R(x, y, t)dt \end{aligned} \tag{2.15}$$

When the modulation function is a square wave, the following expressions can be readily derived by combining the four integrals:

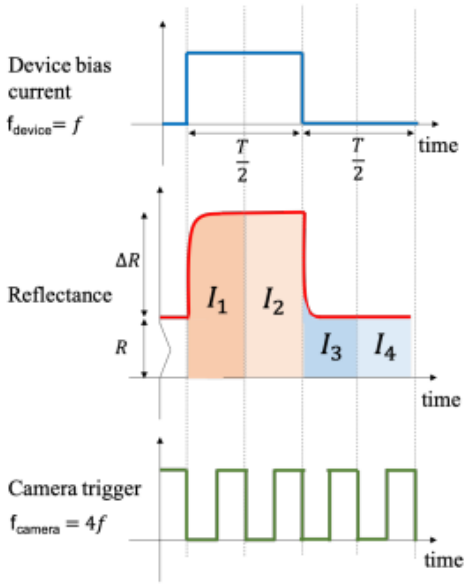


Figure 2.1: A Schematic of the 4-bucket thermoreflectance imaging technique [36].

$$\Delta T = \kappa^{-1}\frac{\Delta R}{R} = \kappa^{-1}\frac{1}{\sqrt{2}}\frac{\sqrt{(I_1 - I_3)^2 + (I_2 - I_4)^2}}{\frac{(I_1+I_2+I_3+I_4)}{4}}$$
$$\varphi(x, y) + \psi = arctan\left(\frac{I_1 - I_2 - I_3 + I_4}{I_1 + I_2 - I_3 - I_4}\right) \tag{2.16}$$

Note that, these expressions could be different if the temperature modulation signal is other kinds of waves.

The sensitivity of a CCD camera is significantly influenced by its bit depth. In this case, a 14-bit camera was employed, capable of detecting changes in reflectivity $\frac{\Delta R}{R} \geq 2^{-14}$, which is comparatively large relative to the typical strength of thermoreflectance signals. However, this limitation does not make the CCD camera inadequate for measuring reflectance changes induced by small temperature modulation. The phenomenon of Stochastic Resonance, driven by the inherent readout noise of the CCD, facilitates the detection of these subtle signals [138]. Through the process of averaging multiple measurement iterations, the weak thermal reflectance signal can be successfully captured. The required number of iterations is determined by the camera's bit depth and the thermoreflectance signal strength, typically ranging between $10^3 - 10^5$ [139].

2.3 Experimental Setup and Protocol

2.3.1 Device Under Test

The diode laser being aged and measured in this work is a 3.75 W rated C-mount single emitter with wavelength near 780 nm and p-side down. An image of the device under test and the microscopic images of its facet is shown in Figure 2.2. Standard anti-reflection/high-reflection (AR/HR) coatings were applied to the laser, but no additional treatments (e.g., passivations) were applied to decrease facet absorption. The stripe width is 180 μm and the cavity length is 1500 μm. The threshold current is 0.65A. While the timescale for unpassivated laser degradation is different than that for passivated laser degradation and may be more localized at the facet (versus the cavity) than in the passivated device, using an unpassivated laser has the practical advantage (for testing purposes) of a more rapid degradation and likely exhibits mechanisms that also occur in passivated devices.

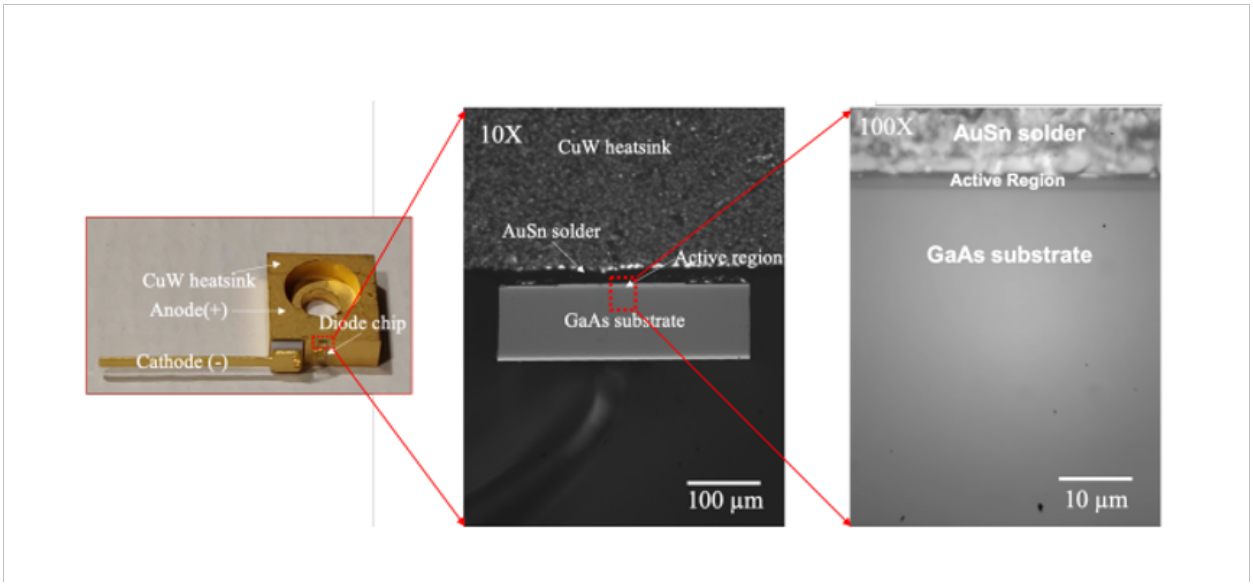


Figure 2.2: Image of the device under test, along with microscopic images of its facet captured at 10× and 100× magnification [36].

2.3.2 Thermoreflectance System

The thermoreflectance (TR) setup we used in this experiment is shown in Figure 2.3. The diode laser is mounted on a stage that maintains a set temperature using a feedback-controlled thermoelectric cooler (TEC). A λ = 470 nm blue LED light with $\Delta\lambda$ = 20 nm full-width half maximum (FWHM) is used as an illumination source. The 470 nm wavelength was selected because GaAs-based materials, which the diode laser is made of, exhibit a strong thermoreflectance response at this wavelength. Moreover, it is the shortest wavelength that provides both a strong thermoreflectance

signal and high spatial resolution. The blue light is incident on the laser diode facet after passing through a pair of condenser lenses with f = 20.1 mm (Koehler illumination), an adjustable aperture iris, a 50:50 beamsplitter, a dichroic mirror (Semrock edge-pass λ = 680 nm) and finally a 50X Mitutoyo infinity-corrected objective. The dichroic mirror is chosen to reflect laser light and transmit LED light. The reflected laser light is directed into a thermopile-based power meter (Gentec-EO) to measure the optical output power. The reflected LED light is collimated by the objective and focused by a f = 200 mm tube lens onto a 14-bit CCD camera sensor (Allied Vision Prosilica GT 1920). More than 99% of the laser light is reflected by the dichroic mirror to a power meter, while the residual laser emission is filtered out by an OD6 band-pass filter in front of the camera. A fiber optic spectrometer is fixed near the laser facet to monitor its emission wavelength. This setup can provide a spatial resolution of ~0.5 μm and temperature resolution of ~ 0.2 K.

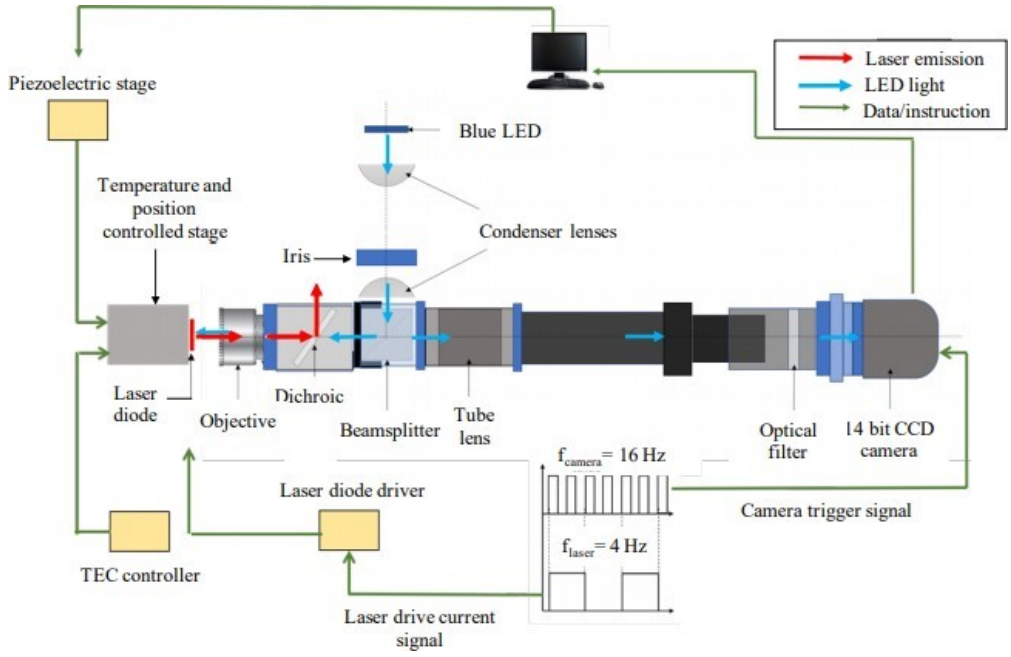


Figure 2.3: CCD-based thermoreflectance imaging setup used in this experiment.

2.3.3 Thermoreflectance Coefficient Calibration

As mentioned previously, the thermoreflectance coefficient κ of a surface is dependent on the material properties, illumination wavelength, and optical properties of the experimental setup. It effectively accounts for the complexities of the material band structure and the optical properties of the material and other optical components in the experimental setup with typical values ranging between 10^{-6} to 10^{-3}. Hence, its value needs to be determined uniquely through calibration experiments for a given combination of sample and experimental setup.

In a typical thermoreflectance calibration experiment, a known temperature change is induced in a material and the thermoreflectance signal is measured. Equation 2.13 then allows the calculation of κ. The high-power diode laser used in this work emits near 800 nm and can be grouped into three main constituents: the GaAs substrate (upon which the epitaxial layers are grown), the waveguide, and the cladding. In order to measure κ for each of these constituents, witness samples of the substrate, waveguide, and cladding (including AR coating) were mounted on a TEC. The TEC was driven by a square wave current and the sample temperature was measured using a micro-thermocouple. Unlike the 4-bucket technique described above, a 2-bucket thermoreflectance measurement is employed for the calibration experiment (Figure 2.4). In this scheme, the camera is phase-locked with the current input and triggered at a frequency of $f_c = 2f$, capturing two frames per cycle, one during the high-temperature state and one during the low-temperature state.

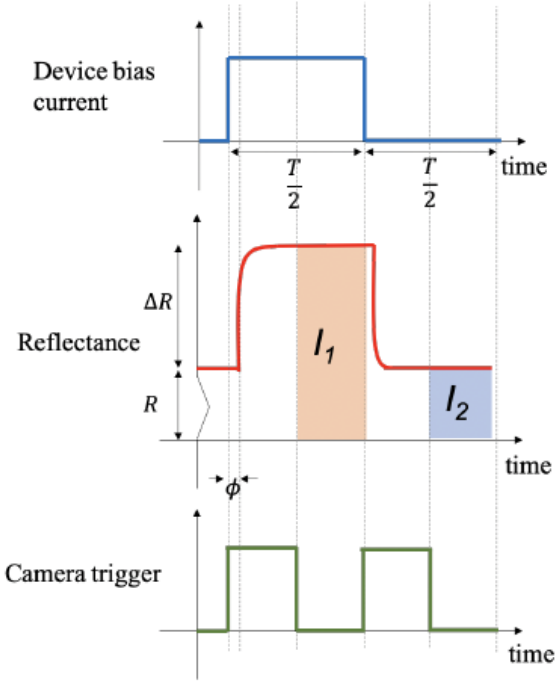


Figure 2.4: A schematic of the 2-bucket thermoreflectance imaging technique.

By modulating the mean and amplitude of the current signal, the temperature of the tested witness sample oscillated around four temperature points (T_{mean}) between 20 °C and 65 °C. ΔT was calculated from the recorded sample temperature. For a known ΔT (~5 K), the dR/R image of the sample was recorded and κ was calculated using Equation 2.13.

The results of calibration experiments with diode laser witness samples are plotted in Figure 2.5. The mean values of κ for substrate, cladding and waveguide of the diode laser at room temperature (with ± sigma uncertainty) were measured to be 2.19×10^{-4} ± 5%, 1.28×10^{-4} ± 7.2% and 1.16×10^{-4} ± 3.2% respectively. We also noticed that there was no significant change in the

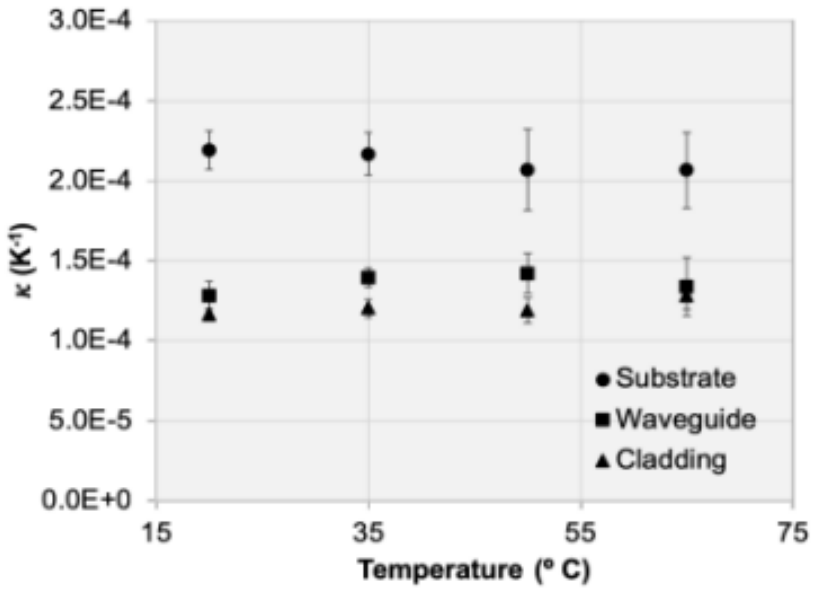


Figure 2.5: Thermoreflectance coefficients of substrate, waveguide, and cladding materials.

thermoreflectance coefficient value for any material as the mean sample temperature varies. Based on the spatial resolution of the thermoreflectance images, we averaged the waveguide and cladding values for κ to yield a single value that we define as the active region κ.

2.3.4 Experimental Protocol

The TR measurement starts from a fresh device and proceeds as follows: First, the TEC stage is set to be 25 °C. Then, we run the laser in CW mode at one of thirteen current points from 0.1 A to 4 A. The current sweep was performed in 0.1 A increments from 0.1 A to 0.6 A, and in 0.5 A increments from 1 A to 4 A. For each current point, we take a set of characteristic data including the optical power, centroid wavelength of the laser emission light, voltage applied at the laser electrodes, and actual TEC temperature. Due to steady state error in the TEC controller, there is a small difference ($\sim$ 0.2 °C) between the actual heat sink temperature and the set temperature. Next, we run the laser in QCW mode at one of the thirteen current points mentioned above and collect thermoreflectance data. In this QCW mode, the laser is biased by a 4 Hz square wave that alternates between zero current and the specified current point. After the characteristic measurements and thermoreflectance measurements, we age the laser under conditions shown in Table 2.1. Note that the aging step durations and conditions are not identical because they were modified over the course of the aging process in response to laser characteristics that at some times exhibited fast degradation and at other times exhibited slow degradation.

As shown in Table 2.1, there are two kinds of aging conditions. Under the regular aging condition, the laser is aged at the rated current (3.75 A), with TEC temperature at 20 °C. Under an accelerated aging condition, the aging current is increased to 4A. In order to minimize temperature induced acceleration under this condition, we lower the TEC temperature to 16.5 °C such that the emission centroid wavelength is the same as that under the regular aging condition. The laser experienced failure during the measurements at 768 hours. The optical output of the laser dropped from ~ 97% of the original power to ~ 32% of the original power due to the failure. Afterwards, additional aging under the accelerated condition was performed up to 1262 hours and several sets of data were taken.

Laser Age (hours)	Aging Step (hours)	Current (A)	TEC Temperature (°C)
0-84	12	3.75	20
84-102	18	3.75	20
102-258	12	3.75	20
258-402	24	3.75	20
402-502	100	4	16.5
502-550	24	4	16.5
550-575	25	3.75	20
575-599	24	3.75	20
599-624	25	4	16.5
624-672	24	4	16.5
672-768	48	4	16.5
Laser Failure at 768 Hours			

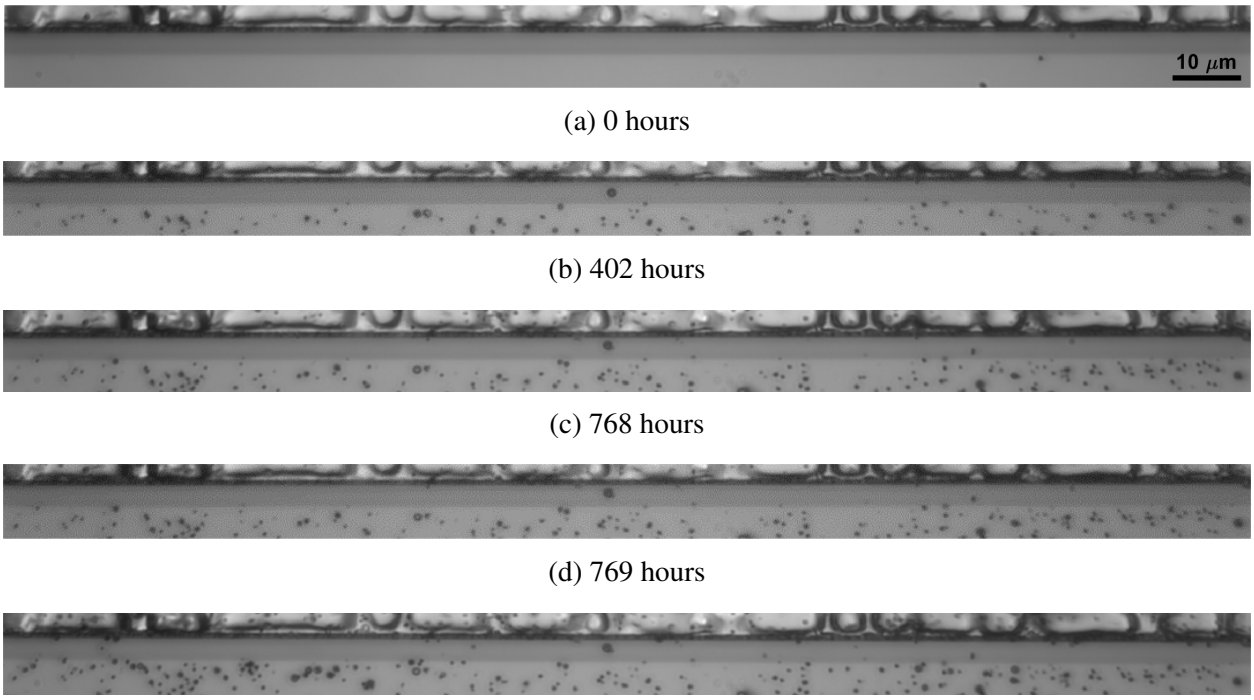
Table 2.1: Aging conditions and aging steps over the laser lifetime

2.4 Results

2.4.1 DC Images and SEM Images of the Laser

Figure 2.6 shows DC images (calculated as the average image intensity during the entire sequence of captured images) at important milestones: fresh device (0 hours; 2.6a), before accelerated aging (402 hours; 2.6b), just before failure (768 hours; 2.6c), just after failure (769 hours; 2.6d) and the last measurement (1262 hours; 2.6e). A comparison of Figure 2.6c and 2.6d doesn't show the

creation of a melted region on the facet that would indicate COMD, suggesting that COD might occurr in the cavity (i.e., COBD). After failure, we used scanning electron microscopy to inspect the laser facet under much larger magnification, as shown in Figure 2.7a. Thirty SEM images were taken in total to cover the entire active region. Nothing unusual was observed in the scanning electron microscopy (SEM) images that would indicate catastrophic mirror degradation. We also observed the deposition of foreign matter (dark spots) on the surface, which occurred from the surrounding environment and was not related to laser operation. Based on energy-dispersive X-ray analysis results of these dark spots after COD (Figure 2.7b and 2.7c), the foreign matter is likely particulates, which contains Si, deposited from the air. Possible sources of Si include thermal grease and rubber gaskets used in other lab equipment within the same room, which may contain silicone. These foreign materials did not appear to impact laser failure, presumably because they do not absorb light at the laser wavelength, as will be discussed later.



(a) 0 hours

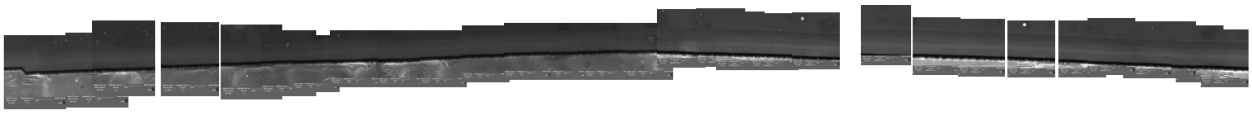
(b) 402 hours

(c) 768 hours

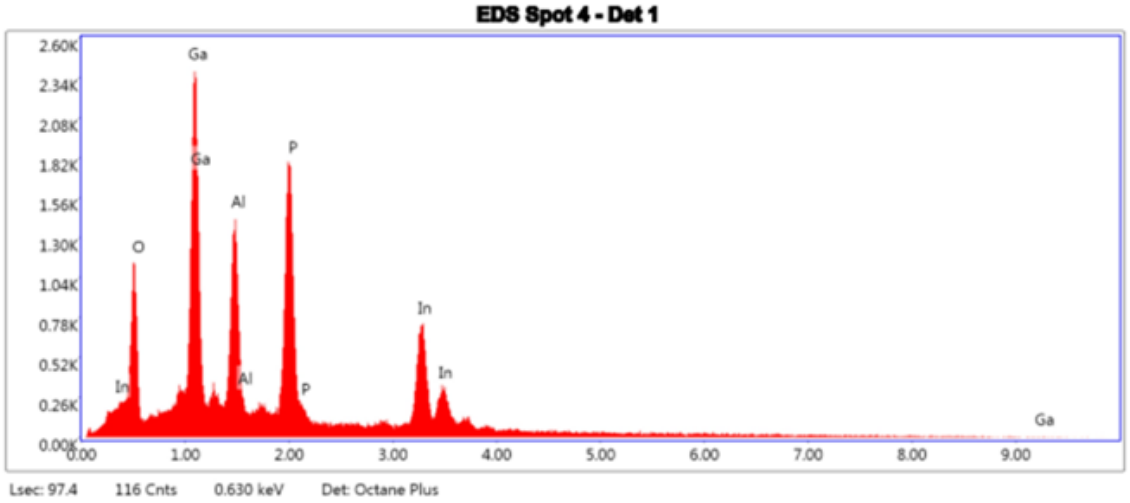
(d) 769 hours

(e) 1262 hours

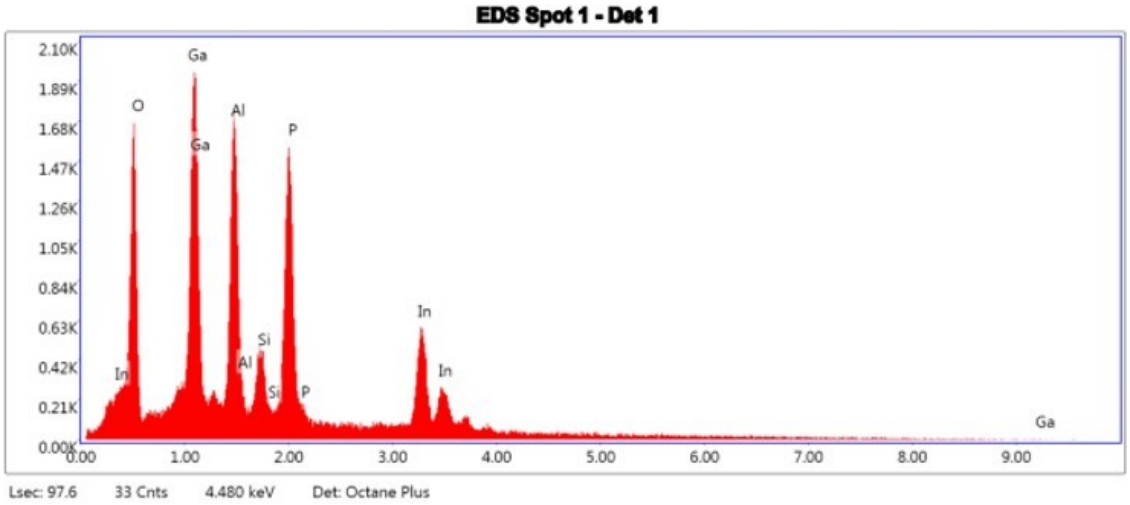
Figure 2.6: DC images of the laser facet, including the active region, a small portion of the substrate, and a small portion of the solder.



(a)



(b)



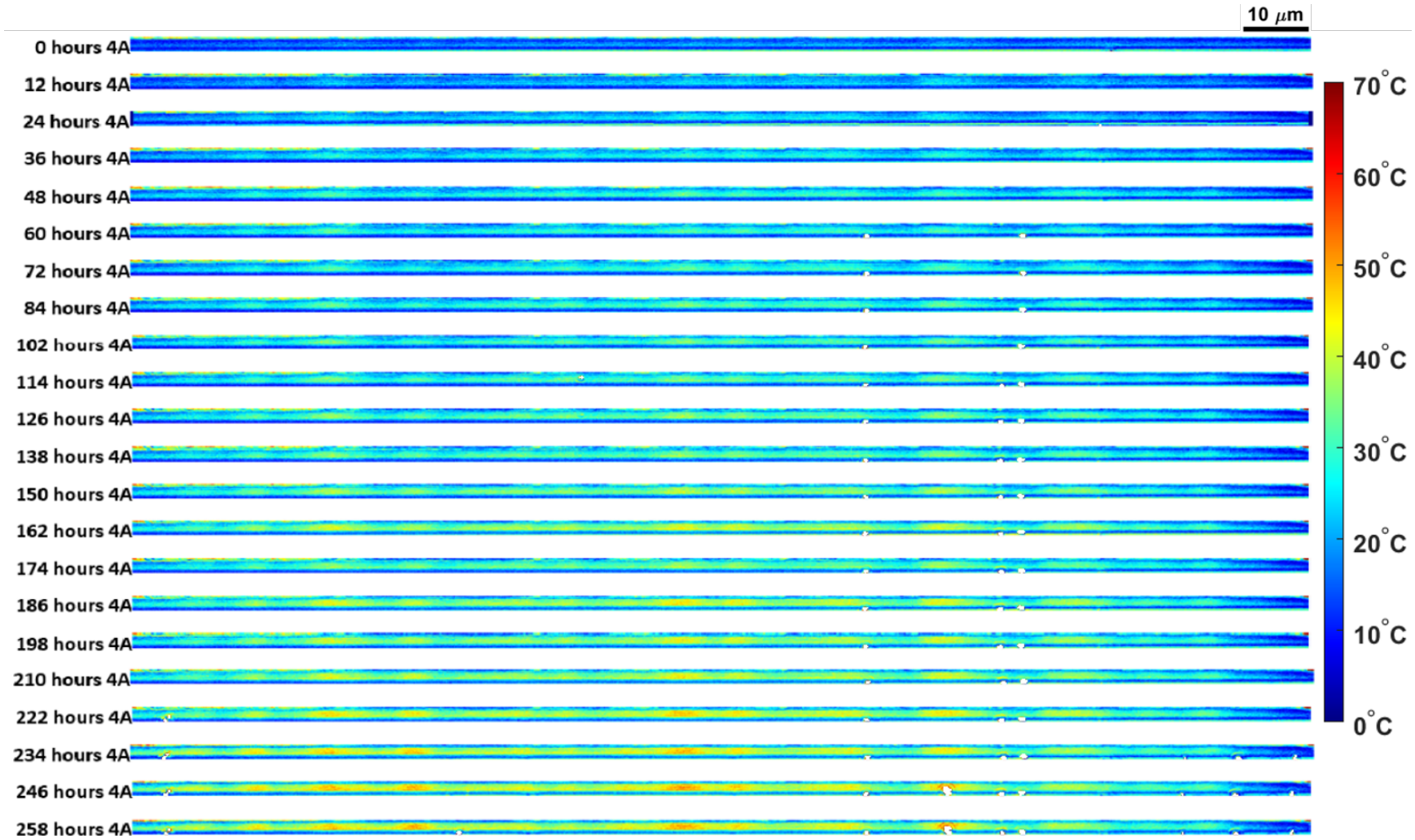
(c)

Figure 2.7: a) SEM images of the front facet stitched together, b) chemical composition of a point on the facet without foreign matter, c) chemical composition of the foreign matter in the middle of the facet.

2.4.2 Temperature Maps

2.4.2.1 Thermal Maps from Thermoreflectance Measurement

Thirteen thermal maps at the corresponding current points were taken after every aging step. 2D thermal maps at 4A from 0 to 1262 hours are presented in Figure 2.8. The solid white spots are associated with the foreign matter mentioned above; the white color doesn't represent the actual temperature of these spots, since their thermoreflectance coefficient is unknown. The foreign matter does not seem to have influenced the formation of hot spots since hot spots near the foreign matter began arising prior to the foreign matter being deposited. As shown in Figure 2.9, from 0 to 502 hours the average facet temperature increased gradually, while several hot spots (A, B, C and D) with substantially higher temperature showed up on the facet. After 502 hours, the average facet temperature fluctuated somewhat, and the hot spot in the middle of the facet (Hot spot B) started becoming concentrated into a smaller region with even higher temperature. The laser experienced COD during the TR measurement at 768 hours when the input current was 4A, so the 3.5A thermal map is plotted instead of a 4A thermal map. In this 3.5A thermal map, we can see the highly concentrated hot spot clearly on the left of the large circular foreign matter.


10 μm
0 hours 4A
12 hours 4A
24 hours 4A
36 hours 4A
48 hours 4A
60 hours 4A
72 hours 4A
84 hours 4A
102 hours 4A
114 hours 4A
126 hours 4A
138 hours 4A
150 hours 4A
162 hours 4A
174 hours 4A
186 hours 4A
198 hours 4A
210 hours 4A
222 hours 4A
234 hours 4A
246 hours 4A
258 hours 4A
70°C
60°C
50°C
40°C
30°C
20°C
10°C
0°C


Dark Spots
282 hours 4A
306 hours 4A
330 hours 4A
354 hours 4A
378 hours 4A
402 hours 4A
502 hours 4A
526 hours 4A
550 hours 4A
563 hours 4A
575 hours 4A
599 hours 4A
624 hours 4A
648 hours 4A
672 hours 4A
720 hours 4A
768 hours 3.5A
Hot spot A
Hot spot B
Hot spot C
Hot spot D
70°C
60°C
50°C
40°C
30°C
20°C
10°C
0°C
Laser Failure

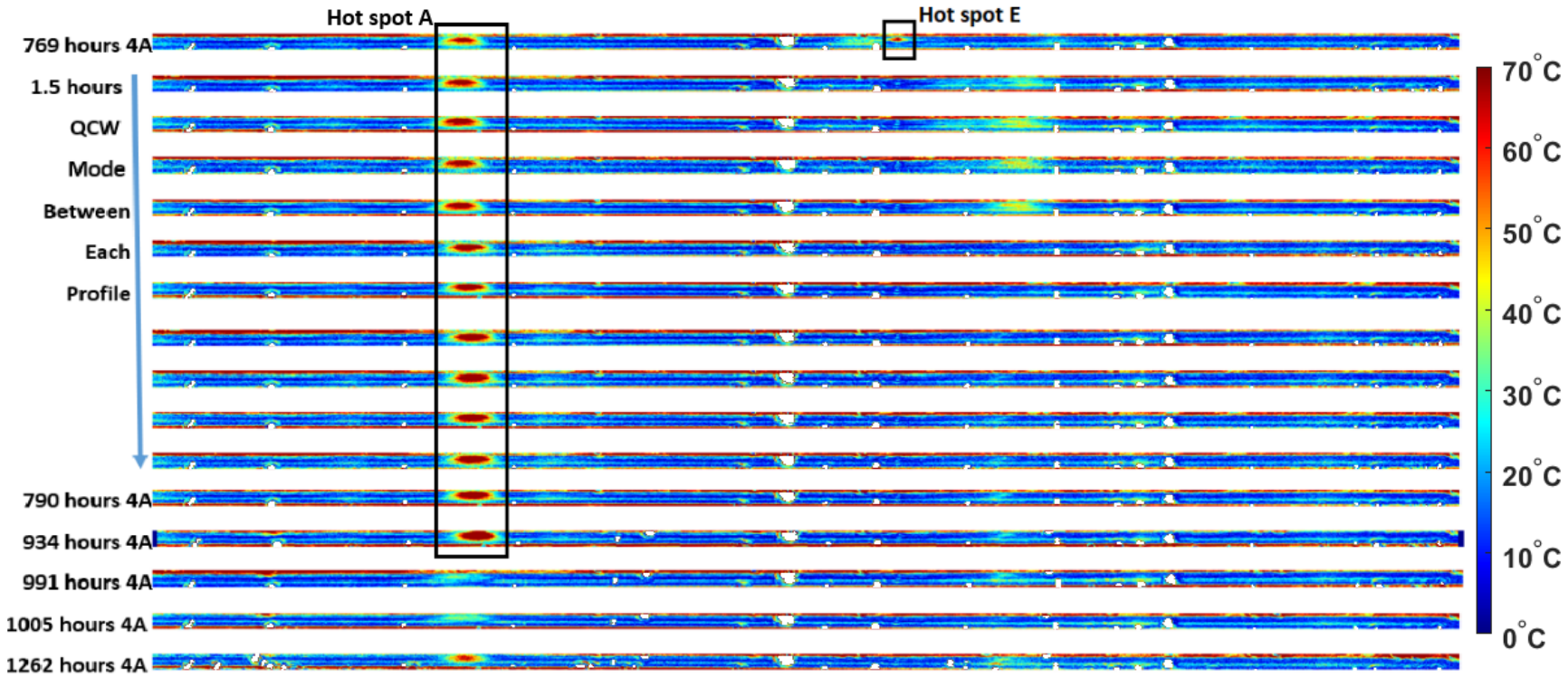


Figure 2.8: 2D thermal maps at 4A from 0 to 1262 hours. The laser failed during TR measurement at 768 hours when current was 4A. Due to that reason, at 768 hours the 3.5A thermal map is presented instead.

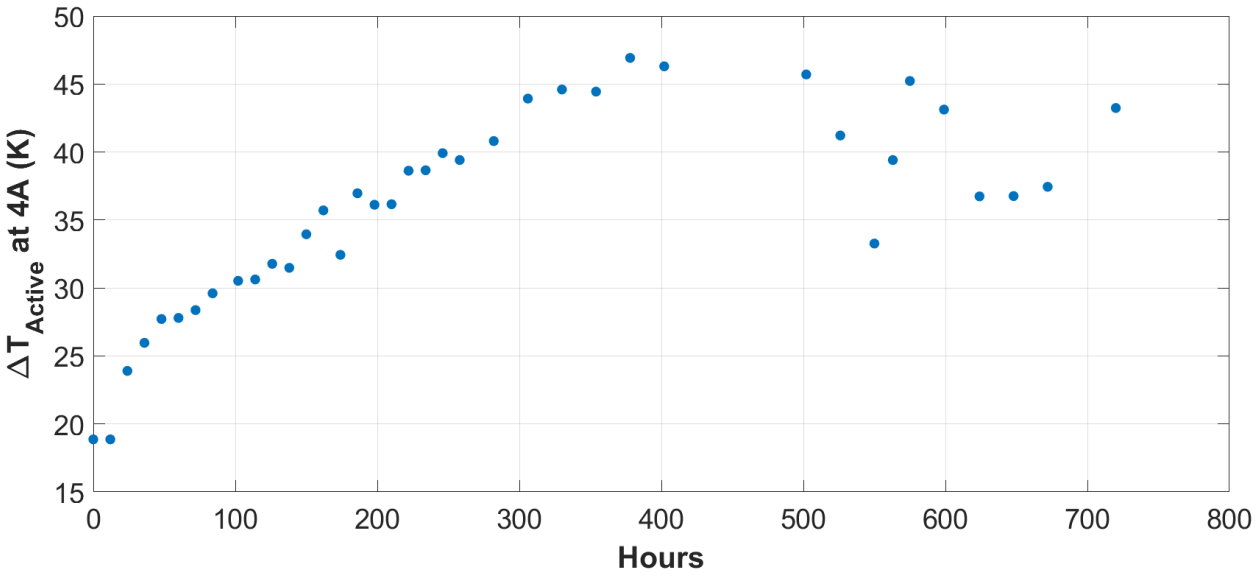


Figure 2.9: Average temperature increase across the active region at 4A (relative to average off-state active region temperature) before laser failure.

In the TR measurement taken just after laser failure, most of the facet has cooled down, except two extreme hot regions. The larger one is on the left side of the facet (hot spot A), while the smaller one is in the middle part of the facet (Hot spot E). While hot spot A arose long before failure, hot spot E appeared only after failure. Optical power declined rapidly after COD, as shown in Figure 2.12a. In order to see the change of temperature distribution of the laser facet during that decline, ten consecutive TR measurements at 4A were taken with 1.5 hours in QCW mode between each measurement. From the 769 hours thermal map to the next thermal map, the large hot spot was still present and the small hot spot disappeared. In the following nine thermal maps, no obvious difference was observed. After the tenth consecutive thermal map, the laser was aged under 4A, CW mode until the laser emission power decreased by a significant amount. The thermal map didn't change much in this period, except that hot spot A started to fade away after 901 hours. One possible reason for this fading away of hot spot A is that the defects there grew deeper into the cavity, shifting the parasitic optical absorption in that area from the facet to the cavity.

2.4.2.2 Average Temperature of Selected Regions

Six regions of interest (labeled in Figure 2.10a) were identified on the facet and the average temperature of each region was calculated. Region 2 is a control region with no hot spot behavior observed throughout the laser lifetime, while the other five regions contain obvious hot spots. Note that, when calculating the average temperature, all the data corresponding to foreign matter were removed. In Figure 2.10b we plot the average ΔT of all six regions over the experimental

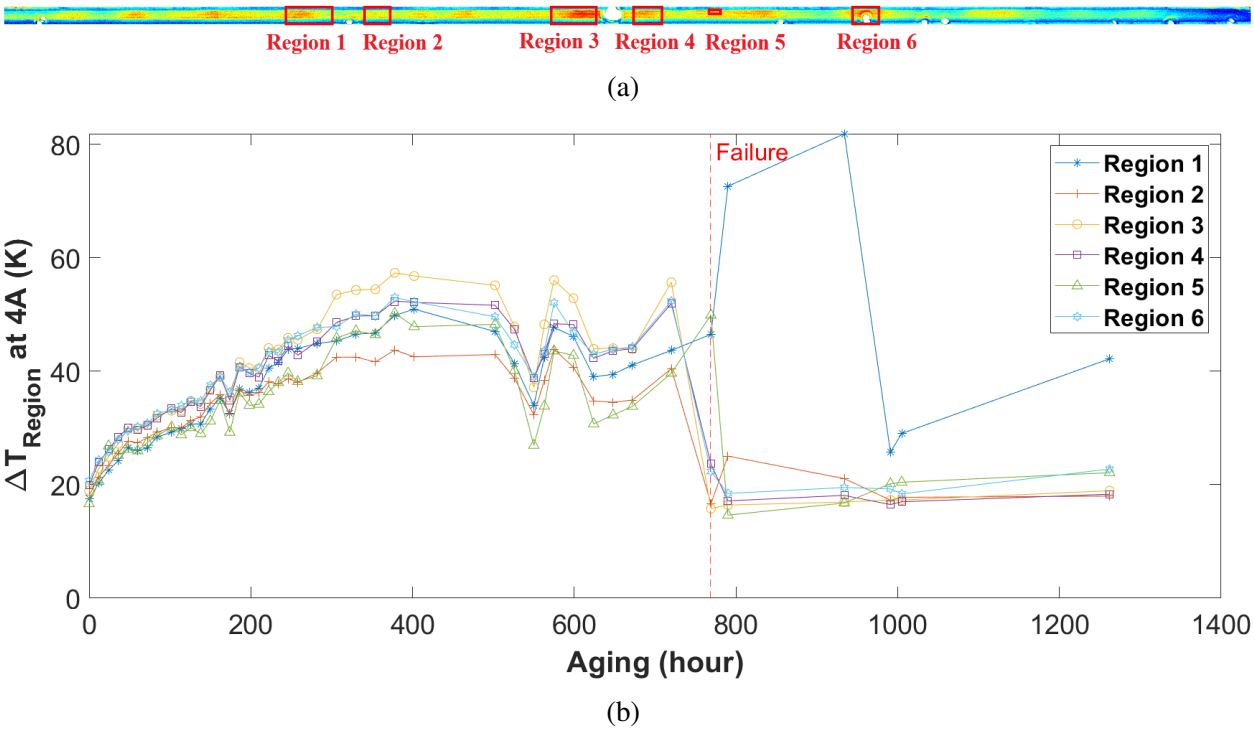


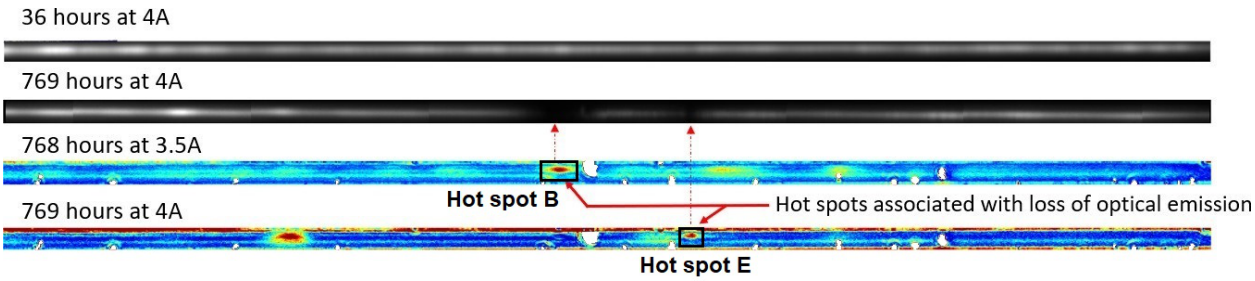
Figure 2.10: a) Six selected regions on the facet (region 2 is a control region in which no hot spot is observed). b) average temperature increase across a given region at 4A from 0 to 1262 hours.

timeline. The average temperatures of all six regions were the same at the beginning, indicative of uniform temperature across the facet. From 0 to 502 hours, the average temperatures of all regions increased and gradually diverged, indicating the facet temperature became more and more non-uniform. Region 3 (hot spot B in Figure 2.8) has the highest average temperature out of all regions. From 502 hours to failure (768 hours), the average temperatures of the regions fluctuated. At 769 hours, all the regions cooled down, except regions 1 (hot spot A in Figure 2.8) and 5 (hot spot E). After 769 hours, region 5 also cooled down. Region 1 heated up more after the failure and then cooled down after 991 hours.

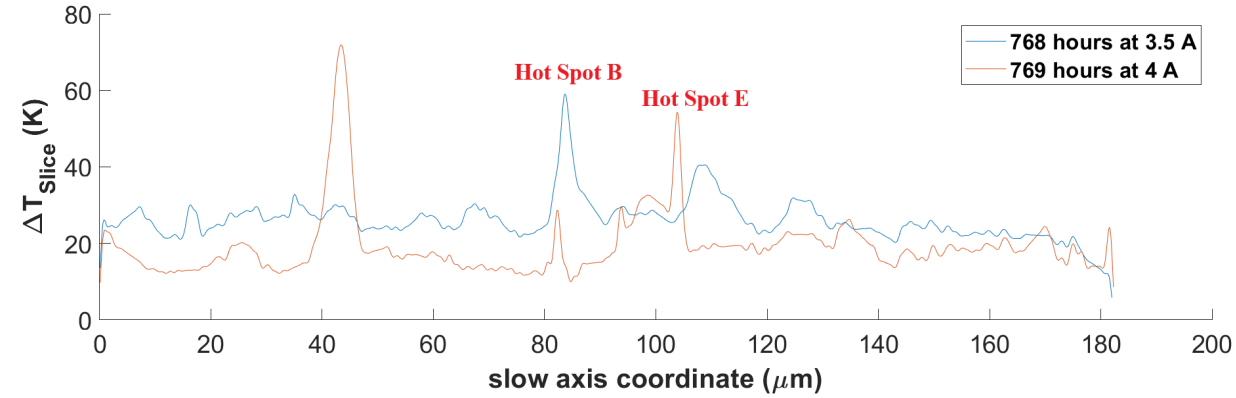
2.4.3 Laser Emission Profile

Figure 2.11a shows two laser emission profiles, one acquired at 36 hours (almost fresh), another at 769 hours (just after failure). It's clear that two regions of the lasers stopped emitting after failure. Hot spot B is a defect that formed long before failure and eventually caused COD, while hot spot E is a defect that formed just after laser failure. If we compare the emission profile just after failure (Figure 2.11b) with the thermal maps taken just before and after failure (Figure 2.11c), we can correlate the dark regions in the emission profile with the two concentrated hot regions (hot spots

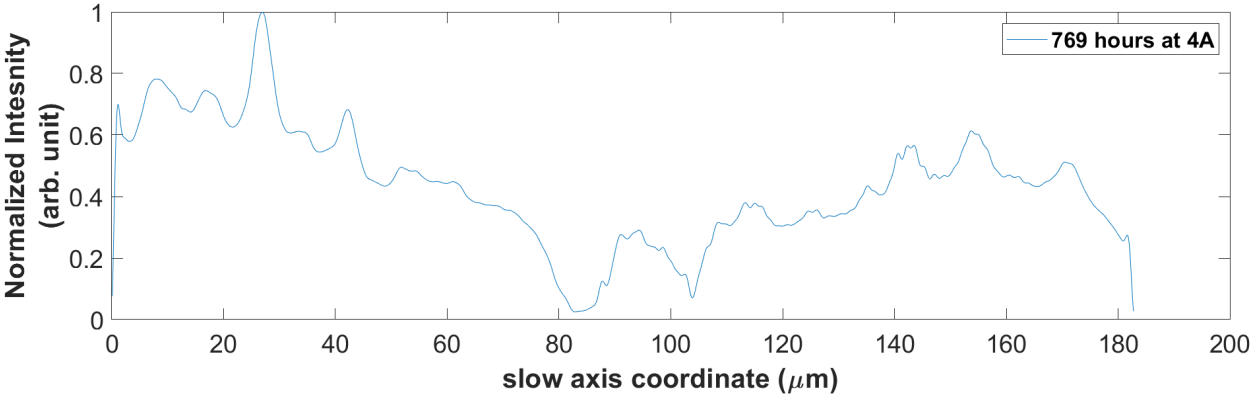
B and E).



(a)



(b)



(c)

Figure 2.11: a) Laser emission profile at 36 hours and 769 hours in comparison with temperature profile just before and after laser failure. b) Temperature profiles (averaged in the fast axis direction) within the epitaxial layers at the facet along the slow axis direction just before and after failure. (c) Normalized emission profile within the epitaxial layers at the facet along the slow axis direction just after failure.

2.4.4 PIV Data

The laser PIV characteristics, including optical power, centroid emission wavelength and voltage between laser electrodes were recorded after each aging step. In Figure 2.12a, 2.12b, 2.12c the optical power's percentage of its original (fresh) value is shown. The optical power decreased gradually from 0 to 702 hours (as the average facet temperature increased gradually), suggesting a gradual degradation process. Before COD, the laser had lost approximately 2.5% of its optical power. After the catastrophic degradation at 768 hours, there is a larger decrease of optical power, as shown in Figure 2.12c. The laser lost approximately 68% of its optical power due to COD, after which the optical power dropped quickly (74% loss) in the first several hours and then slowly to about 78% loss.

Figure 2.12d shows that the centroid emission wavelength at 4A is very stable from 0 to 720 hours. After failure, the emission spectrum of the laser is unstable, so no centroid wavelength can be acquired. The emission wavelength is determined by the bandgap of the quantum well material, which is temperature dependent. Therefore, from the change of the emission wavelength we can estimate the change of the bulk temperature in the laser cavity. The coefficient for this linear relationship has been estimated to be 0.26 nm/°C for ~800 nm devices [140]. In the plot, the centroid wavelength remains at 783.4±0.1 nm. The bulk temperature change is thus negligible, while the facet temperature shows a gradual increase.

In Figure 2.12e we plot the voltage between the laser electrodes at 4A from 0 to 1262 hours. The voltage increased rapidly in the first 100 hours from ~1.885 V to ~1.897 V. After 100 hours, the voltage is very stable until failure. Similar to the optical power there is a large sudden decrease of the voltage due to COD, when it dropped to ~1.88 V. It declined quickly in the first few hours thereafter, and then slowly declined to ~1.874 V.

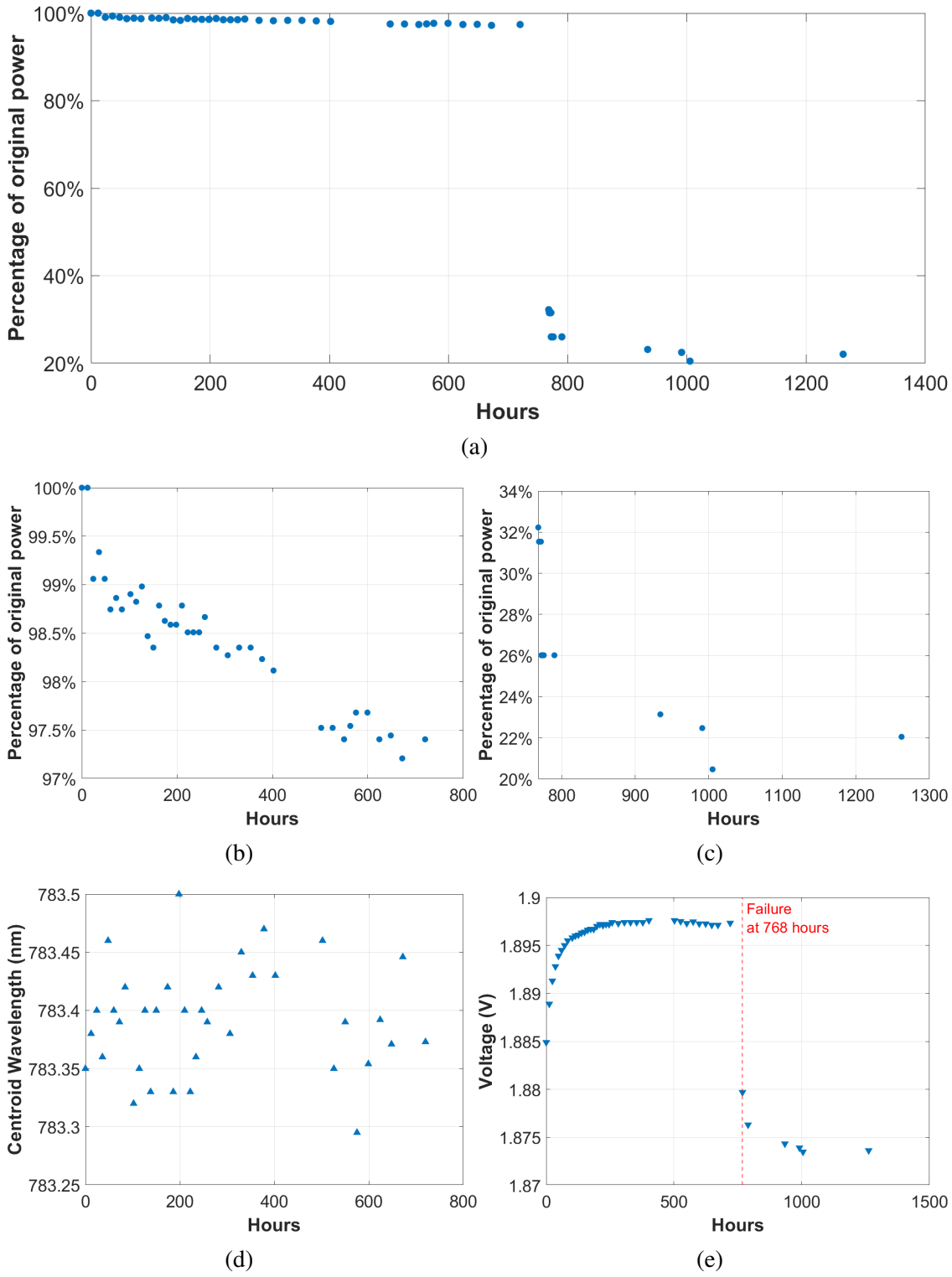
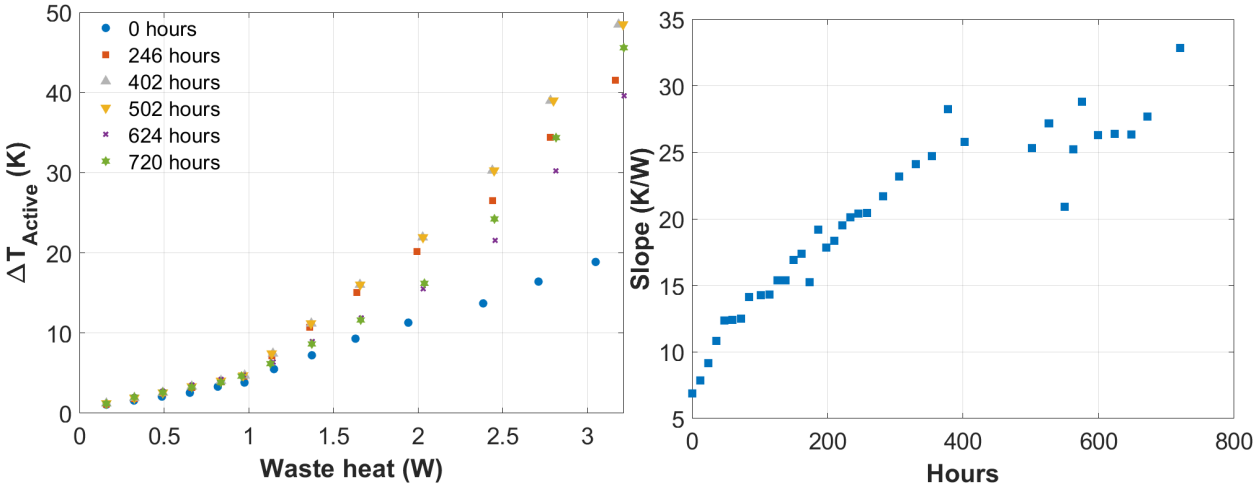


Figure 2.12: PIV characteristics of the laser under test over its lifetime, a) optical power percentage (relative to initial state) at 4A. b) optical power percentage at 4A before failure, c) optical power percentage at 4A after failure, (d) centroid wavelength at 4A, (e) voltage between laser electrodes at 4A.

2.4.5 Facet Optical Absorption

In previous work Jha et al. introduced a method to measure facet optical absorption using the slope of average active region ΔT vs. waste heat [141], in which a linear fitting is used to calculate the slope and waste heat is calculated by subtracting the optical power from the input electrical power. While that study used a fresh device, in this aging study we found (see Figure 2.13a), that the above threshold part of the ΔT vs. waste heat relationship became more and more non-linear with aging (precluding a linear fit), while the below-threshold part didn't change significantly.

Note that ΔT here is an average value of the entire active region with all the pixels corresponding to foreign material removed; the nonlinearity may be related to the temperature distribution becoming increasingly inhomogeneous. Therefore, instead of using a linear fit, we used a second order polynomial fit and calculated the slope at the maximum waste heat value (corresponding to a current of 4A), as shown in Figure 2.13b. The slope value increased gradually from 0 to 502 hours. From 502 to 720 hours, there were some fluctuations, similar to those found in the thermal maps during that time. Still, the overall trend of the slope at 4A is increasing.



(a) (b)

Figure 2.13: a) ΔT of active region vs. waste heat for above and below threshold current points. b) Slope of 2nd order polynomial fitting line at 4A from 0 to 720 hours, as an indicator of facet absorption.

2.4.6 Discussion of Facet Temperature Profiling

This part of the dissertation provides a spatially resolved thermal map of a high-power laser facet with high resolution over its lifetime, which can be used to assess the formation and evolution of defects on the front facet. First, gradual degradation (~2% optical power loss) was observed during

the aging process, as evidenced by gradual facet temperature increase (Figure 2.11b), gradual optical power decrease (Figure 2.12b), and gradual facet optical absorption increase (Figure 2.13b), with no visible damage on the facet in both DC images and SEM images (Figure 2.6).

While the facet temperature gradually increased, the bulk temperature (measured by wavelength shift) stayed roughly constant with aging (Figure 2.12d). Note that, although the bulk temperature is stable, it is possible that hot spots exist within the laser cavity. These cavity hot spots can be seen in the facet thermal map if they are very close to the facet. Therefore, the observed gradual degradation in optical power is likely due to a gradual accumulation of defects at or near the facet.

Because of the high spatial resolution of our thermal imaging approach, we were able to see many local hot spots appear on the facet (Figure 2.8). As mentioned above, these hot spots may be due to defects that are close enough to the facet to create an increase in temperature there, but not so close as to be visible in SEM. Alternatively, they may be defects on the facet that are too small to be visible by SEM (i.e., nanoscale), but produce enough non-radiative heating to be visible on the thermal map [27].

Second, catastrophic optical degradation was observed after 768 hours of aging. We saw a sudden large decrease in optical power (Figure 2.12c) and operation voltage (Figure 2.12e) and a large temperature drop across most of the facet (Figure 2.8). The dramatic voltage decay is likely attributed to the formation of the metal-rich zone during COD as mentioned in 1.3.1, which acts as an electrical bridge across the junction. Optical emission ceased in two regions of the facet after COD, and both were associated with hot spots with very high temperature in the thermal map, likely reaching the critical temperature required to trigger thermal runaway (Figure 2.11). The spot that appeared before laser failure (hot spot B) had been present since very early testing; it fluctuated in intensity over time but in general was the hottest area of the facet, while hot spot E appeared after failure. Because hot spot B was likely the spot that led to device failure, we note that this likely precursor to eventual COD was apparent on the laser facet after 72 hours of aging. However, no morphology change can be observed under 50X microscope (Figure 2.6) and 40000X SEM after failure, which agrees with prior work that found an increase in facet temperature due to the creation of point defect clusters with aging, but observed no visible damage in the active region on the facet [119]. The results of prior work suggest that these two hot spots may be associated with dark line defects (or dark band) that started very close to the facet, propagated into the cavity in the $< 110 >$ direction, and resulted in COD. DLDs in prior works were observed (using CL) only in the cavities of lasers that had experienced COD [16],[119],[109] and were composed of highly non-radiative complex dislocation networks, as mentioned in 1.3.1 [14],[84]. The device tested in this chapter was not analyzed for the presence of cavity DLDs.

Based on these results, our interpretation of the aging process in this particular device is that point defect clusters are first formed gradually with aging, primarily at or near the facet. These point

defect clusters absorb laser light and cause broad (non-localized) facet heating. This broad heating facilitates the formation of more point defect clusters and hence further facet heating. Some point defect clusters are very near the facet and can cause localized hot spots on the facet. One hot spot in particular is prominent in this positive feedback loop; when the defect density and/or temperature there reaches a critical value, thermal runaway is triggered, leading to the formation of a molten zone near the facet. The molten subsequently propagates into the cavity, ultimately resulting in laser failure. In this way, an intense hot spot is observed on the facet without accompanying visible facet damage. The gradual and minor 2% loss in optical power before laser failure observed in this chapter appears to result from facet absorption of the laser. However, as will be shown in the next chapter (chapter 3), results from simultaneous cavity and facet measurements indicate that the propagation of dark line defects (DLDs) within the laser cavity is the primary contributor to the gradual degradation process. Similar conclusions about the contributor of gradual degradation were reached in studies on the same type of devices conducted by our collaborators at LLNL [142].

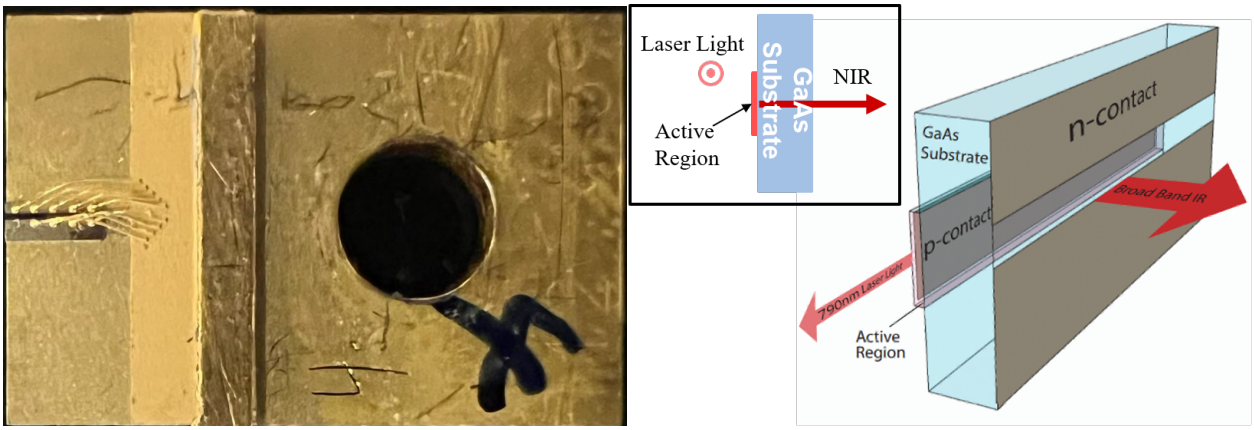
CHAPTER 3

Defect Characterization of High-Power Diode Lasers Cavities During Aging

In this chapter, we delve into the characterization of defects within the laser cavity. As highlighted in Chapter 1, existing characterization methods are insufficient to fully address the specific requirements of our investigation. Although thermoreflectance microscopy initially appeared promising, its utility was compromised by broadband near infrared (NIR) emissions originating from the core layers (waveguides and quantum well) of diode lasers, which overwhelmed the thermoreflectance signal. This challenge, however, led to the innovation of a technique that utilizes this broadband NIR emission to image the formation and evolution of DLDs through the substrate of high-power diode lasers. The imaging wavelength lies in the mid-gap region, more than 200 nm longer than the lasing wavelength. This approach is in situ, non-destructive, and enables 2D defect profiling with relatively high spatial resolution ($\sim 1\mu m$), allowing long-term aging studies from the fresh device state through failure. In the following section, the NIR defect imaging technique will be described in detail.

3.1 Broad Band NIR Emission

Broad band NIR that is not at the fundamental laser wavelength was observed in diode lasers previously and has also been used in the analysis and characterization of diode lasers operating at various fundamental wavelengths (980nm, 808nm, 650nm) from the facets and edges [143][144][145][146][147][148][149][150][151]. Using a state-of-the-art SWIR camera, we were able to expand the use of this parasitic NIR to enable high-resolution imaging of DLDs in diode laser cavities through the substrate.



(a) (b)

Figure 3.1: a) Image of a device undergoing cavity defect characterization. b) Schematic of the high-power diode laser being measured (top left inset shows the front view).

3.1.1 Device Under Test

The diode laser devices being aged and measured in this work are 3.75 W-rated CT-packaged single emitters with a wavelength near 790 nm and junction side down. They were grown on GaAs substrate via solid-source molecular beam epitaxy from phosphide-based epitaxial materials. Standard anti-reflection/high reflection (AR/HR) coatings were applied to the facets correspondingly without further treatment. The stripe widths are ~190 μm and the cavity lengths are 1500 μm. The threshold currents are ~0.65A. In order to image defects in the cavities, a 100 μm wide window was fabricated on the n-contact of each laser. An important parameter concerning the window devices is the concentration of oxygen dopant in the active region. There are three distinct oxygen levels: Level 0 (L0) indicates no artificial oxygen doping ($[O] = 0.7 \times 10^{15}\, cm^{-3}$); Level 1 (L1) signifies a moderate amount of oxygen doping ($[O] = 2.2 \times 10^{15}\, cm^{-3}$); and Level 2 (L2) represents a higher concentration of oxygen doping ($[O] = 2.5 \times 10^{15}\, cm^{-3}$). Additional details regarding the oxygen concentration can be found in the work published by our collaborators at LLNL [142]. An image of the CT-packaged laser and a schematic of the structures being measured are shown in Figure 3.1a and Figure 3.1b.

3.1.2 Experimental Setup

The diode laser is mounted on a stage that maintains a set temperature using a feedback-controlled TEC. As mentioned above, broadband NIR originating from the laser cavities is used to image the defect growth. So, the n-contact window is oriented towards the camera. The broad band NIR emitted from the laser cavity has energy smaller than the GaAs substrate bandgap, and therefore

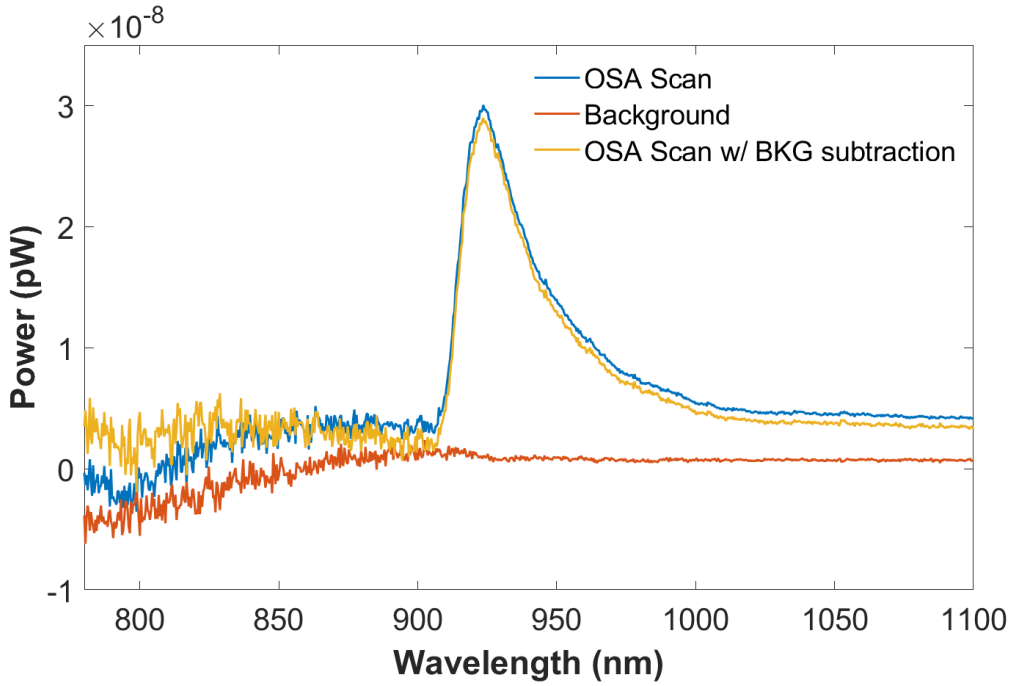
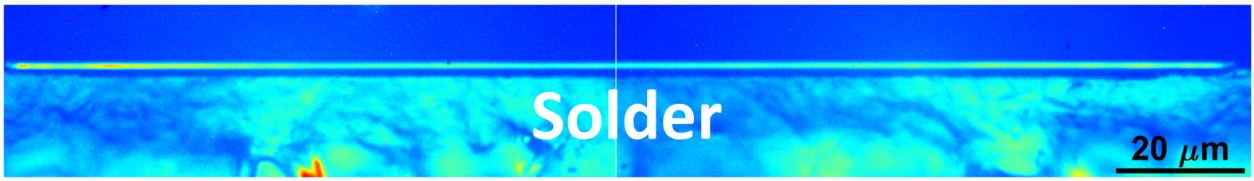


Figure 3.2: Spectrum of the broadband NIR from the n-contact window.

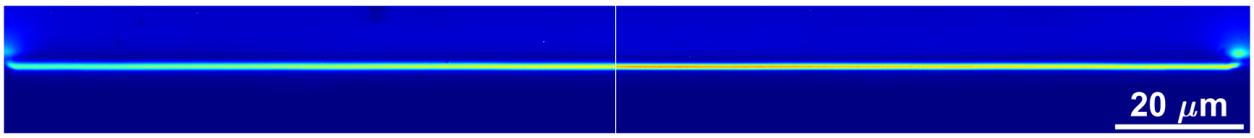
can pass through the substrate without being absorbed. It is collimated by a 10X Mitutoyo NIR infinity-corrected objective and focused by a f =200 mm tube lens onto a 14-bit high sensitivity SXGA SWIR camera sensor. Although almost no 790 nm laser light could leak through the over 100 μm-thick GaAs substrate, two OD4 970 nm band-pass filters in front of the camera guaranteed that no 790 nm laser light is received by the camera. A fiber optic spectrometer is fixed near the laser facet to monitor the laser light wavelength, while the camera is oriented toward the n-contact window. This setup provides a spatial resolution of ~1 μm.

3.1.3 NIR Properties

A spectrum of the broad band NIR is shown in Figure 3.2, which is measured by an optical spectrum analyzer (OSA). In the spectrum, a peak that is not at the device lasing wavelength (~790 nm) is present starting at ~910 nm (1.36 eV), reaching a maximum at 925 nm (1.34 eV) and then decaying slowly. The asymmetric lineshape of the peak is likely due to strong electron-phonon coupling at the defect [152][153]. Broadband NIR from a high-power quantum well laser with a similar spectrum has previously been observed with its source attributed to a buffer layer adjacent to the n-cladding layer [143]. This does not appear to be the case for our devices, based on PL) and electroluminescence (EL) imaging of the facet in which the NIR emission appeared (Figure 3.3a and 3.3b). Note that the PL measurement was performed on the whole front facet, with excitation



(a)



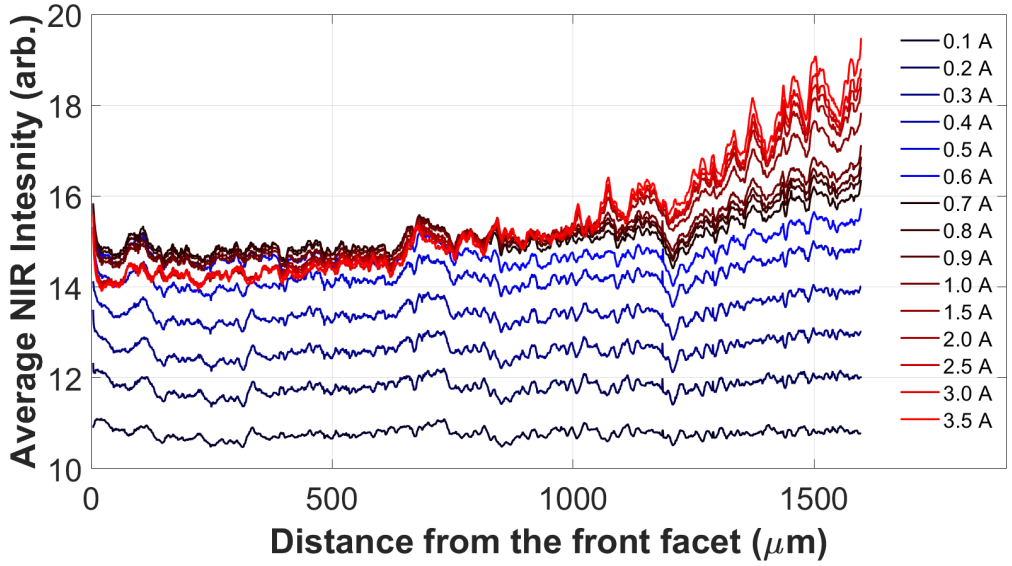
(b)

Figure 3.3: a) Photoluminescence intensity map of NIR emission measured from the laser facet under a 100X objective (Excitation wavelength at 970 nm). b) Electroluminescence intensity map of NIR emission measured from the laser facet under a 100X objective (I_{Laser} = 500 mA).

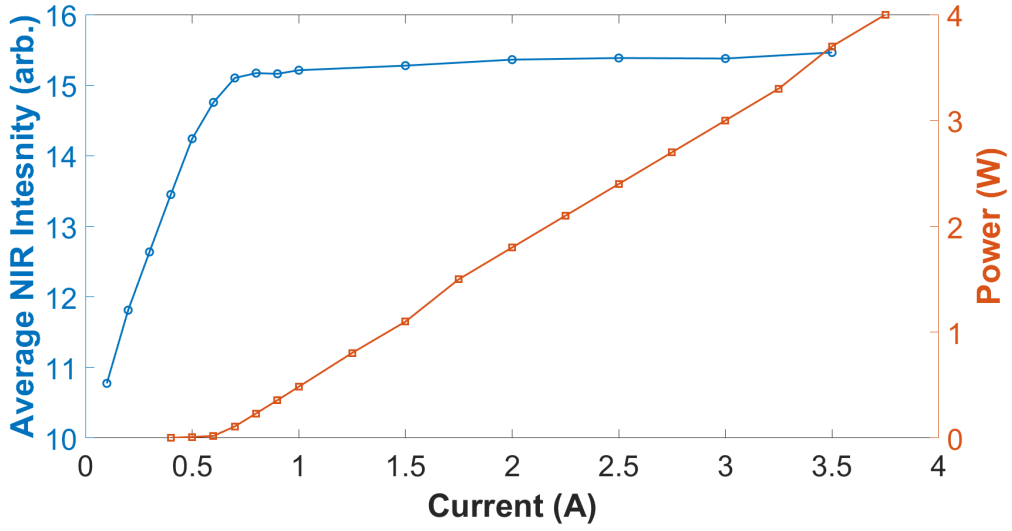
wavelength at 970 nm. In the PL image (Figure 3.3a), the bright region below the core region is the AuSn solder on the p-side reflecting the light. The dark line between the core region and solder is the p-cladding layer. After comparing the measured thickness and width of the bright stripe in these intensity maps with structural information regarding the device epi layers, we believe that the broad band NIR originates primarily from the QW, with a small portion from the waveguide core.

As shown in Figure 3.4a, the NIR emission has an intensity gradient along the cavity that increases with current. This intensity gradient is likely due to the carrier density gradient along the longitudinal direction, induced by the longitudinal spatial hole burning effect [154][155]. The spatial average of NIR intensity across the area defined by the p-contact saturates for currents above threshold (Figure 3.4b), indicating that this NIR emission is related to carrier density which also saturates above threshold. The slowly increasing intensity above threshold can be explained by the non-clamping of carrier density in the waveguide. A similar saturating phenomenon has been reported by Hempel et al. and Ziegler et al. for SWIR near 1 eV and 1.3 eV [144][148]. Other spectroscopic measurements (photocurrent spectroscopy with illumination from the facet or through the substrate and n-side window) of devices fabricated from the same epitaxial material show deep-level trap absorption with optical absorption bands spanning from 0.8 to 1.4 eV, which is consistent with reported deep level optical spectroscopy of our waveguide material [156]. Previous work also reported oxygen-related deep states near 1.2 eV in an AlInP lattice [157]. Other groups have reported related similar emission spectra in other devices or bulk materials and also attributed it to deep levels [144][145][158]. A more recent work by Tomm et al. reported three parasitic NIR emission peaks in 808 nm and 650 nm devices, and attributed the first peak (located very near the fundamental emission wavelength) to the Urbach tail of the QW, and both the second peak at 1.4

eV and the third peak at 1 eV to the GaAs substrate [149]. The work of Hempel et al. in 2014 assigned an observed 1.3 μm peak in a 980 nm device to different species of native point defects in the active region [147]. Based on our observations we believe that the observed NIR signal is associated with spontaneous emission from deep levels in the QW and waveguide core layer of our devices, which is similar to the reasoning of Hempel et al.



(a)



(b)

Figure 3.4: a) Average intensity of NIR in p-contact region along the cavity of device CTNW5 at 0 hour. Different lines represent data collected at currents below and above threshold. b) Average NIR intensity of the entire p-contact region (blue) and L-I curve (orange) of device CTNW5 at 0 hours.

3.2 In situ, Non-destructive NIR Imaging Technique

During defect imaging, the laser is powered in CW mode at different currents, below and above the threshold current. For each current point we take a set of characteristic data, including the optical power, centroid laser wavelength, voltage between laser electrodes, and actual TEC temperature, as we did during the facet measurements. Then we bring the p-contact into focus through the cavity window, since it is very close to the active region that we are interested in, and a snapshot is taken using the SWIR camera to acquire an intensity map of the NIR emission. Figure 3.5 shows what this intensity map looks like. The darker p-contact is surrounded by a bright unpumped region. We believe the brightness of the unpumped region is a result of light being scattered by the epitaxial ridge and front facet; when a long DLD was formed, the intensity in the corresponding bright stripe decreased. After these measurements, we age the laser (e.g., 50 hours or 100 hours) at a steady current and steady TEC temperature. For the regular aging condition, the current is 3.75 A and the TEC set temperature is 20 °C. For level 1 accelerated aging, the current is 4 A, and the TEC temperature is decreased to maintain the centroid wavelength at the same value it has at 20 °C. For level 2 accelerated aging, the current is 4 A and the TEC set temperature is 50 °C.

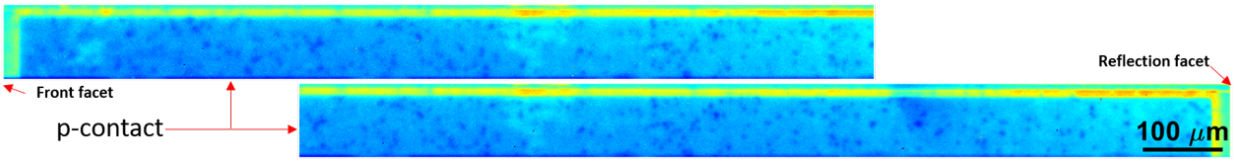


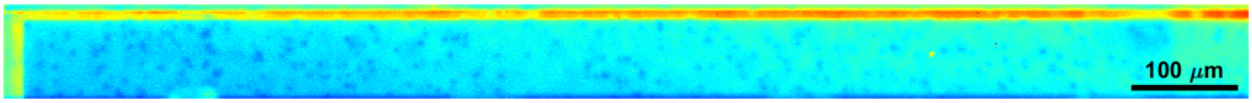
Figure 3.5: Intensity maps of NIR emission from the n-contact window under a 10X objective (CTNW5 at 0.7A after 100 hours of aging). Only three fourths of the total cavity length can be seen in one image due to a limited camera field of view.

3.2.1 Time-resolved NIR Intensity Maps

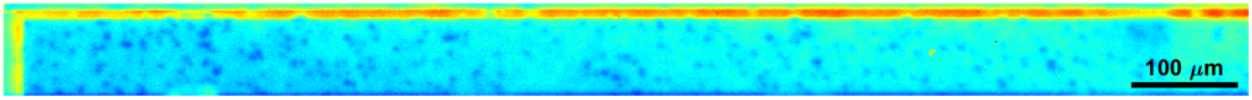
We measured nine devices in total (CTNW2, CTNW3, CTNW4, CTNW5, CTNW 10, CTNW 11, CTNW33, T120Z9, T120TA) from the initial of their lifetimes following the experimental protocols mentioned above. Due to minor alignment variability between the n-contact window and p-contact stripe among the devices, slightly different parts of the p-contact were seen through the window. The NIR intensity maps of these devices during aging will be presented in this section. In some devices, dark spots and dark lines (along the $\langle 1\bar{1}0 \rangle$ cavity direction) that we considered as defects can be seen. We particularly examine intensity maps on the front facet end since most of the dark line activities were observed to occur on this side. The intensity maps at 0.7 A are shown here because they give the best view of dark spots and dark lines due to intensity clamping above threshold and intensity gradient along the cavity.

3.2.1.1 CTNW2

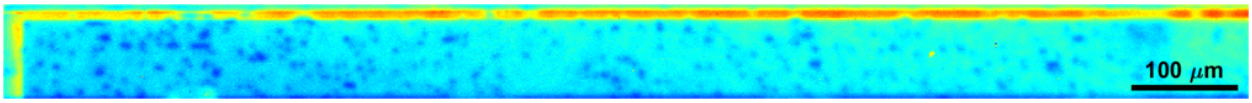
Device CTNW2 is an L0 device and was measured with the TEC stage kept at 25 °C, and subjected to level 2 accelerated aging from 0 to 850 hours. Figure 3.6 shows the IR intensity maps of the device at 0.7A over the entire aging period. Numerous small dark spots were observed in the 0-hour (fresh) intensity map of device CTNW2. Some of these initial dark spots developed into dark lines that propagate along the $\langle 1\bar{1}0 \rangle$ cavity optical axis after aging. Some of these dark lines grew longer after further aging. Propagation was observed toward both the front (AR) facet or the reflecting (HR) facet; however, more propagation activities occurred near the front facet. After each aging step, either new dark lines were formed or existing dark lines propagated further, although not every existing dark line propagated after every aging step. A notable aspect of device CTNW2 was the emergence of a dark line at/near the front facet after 100 hours of aging, which subsequently extend into the cavity. Thermoreflectance microscopy revealed a corresponding hot spot at this location on the front facet, a topic discussed in greater detail in 3.2.4.7. Consistent with the formation and propagation of the dark lines, the optical power output of device CTNW2 declined by 41.46% of its initial value during each aging step (Figures 3.15a). The decline followed a non-linear trend, with a fast initial decay that gradually diminished over time. The underlying cause of this nonlinearity decay remains unclear. As the rate of optical power reduction became less pronounced, a corresponding decrease in the occurrence of dark spot propagation was observed. The laser's wavelength also red-shifted by 3.39 nm, indicating an increase of approximately 13.04 $^{\circ}C$ in average cavity temperature (3.15b).



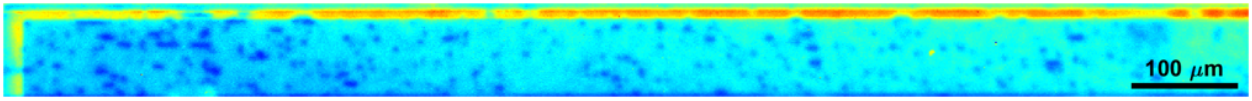
(a) 0 hours



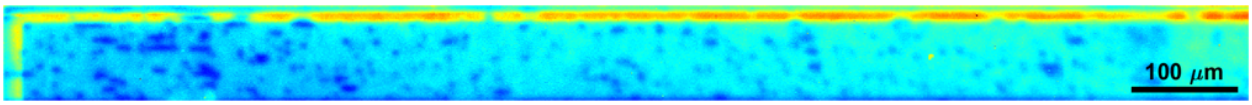
(b) 50 hours



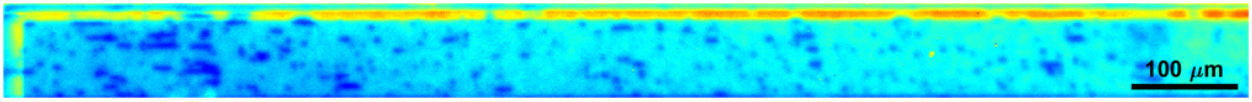
(c) 100 hours



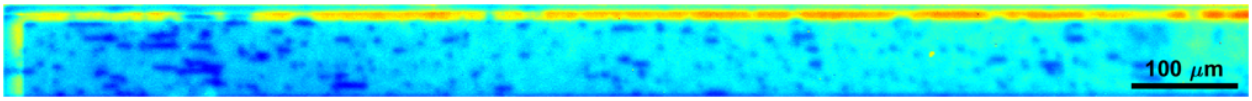
(d) 150 hours



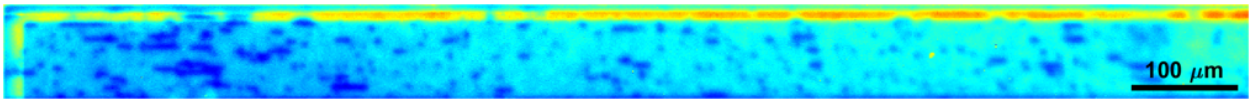
(e) 200 hours



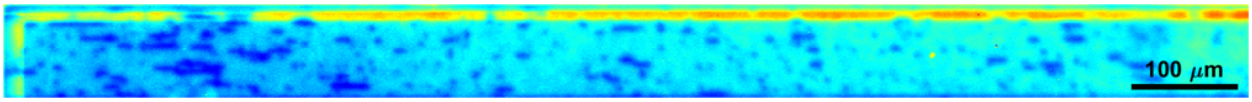
(f) 250 hours



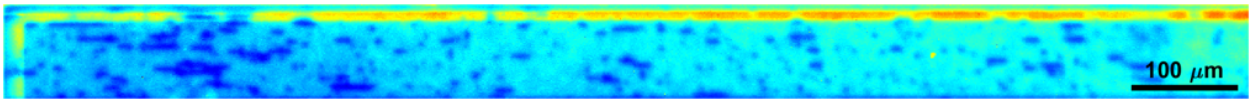
(g) 300 hours



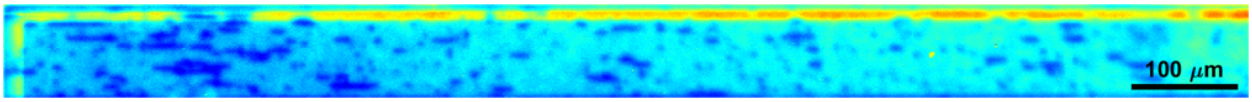
(h) 350 hours



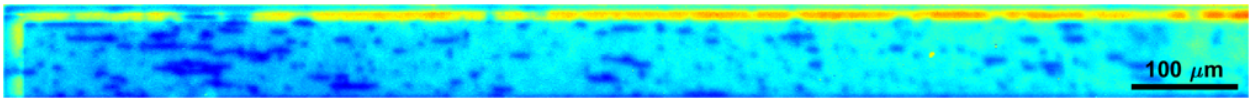
(i) 400 hours



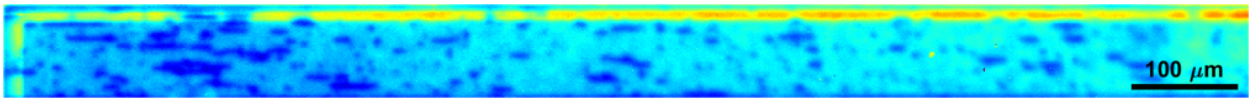
(j) 450 hours



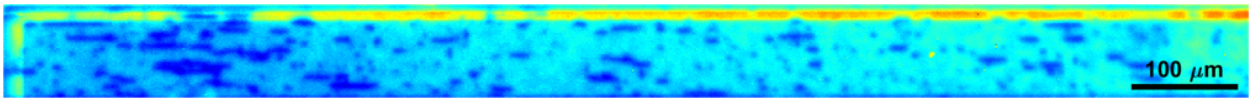
(k) 500 hours



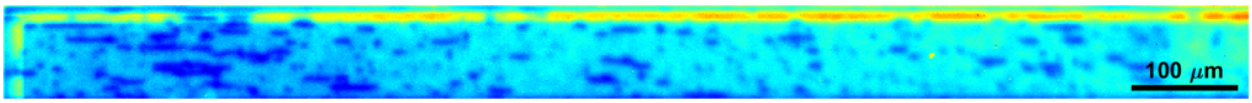
(l) 550 hours



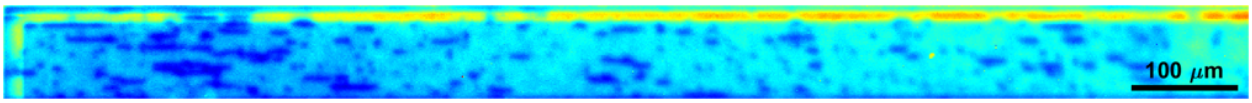
(m) 600 hours



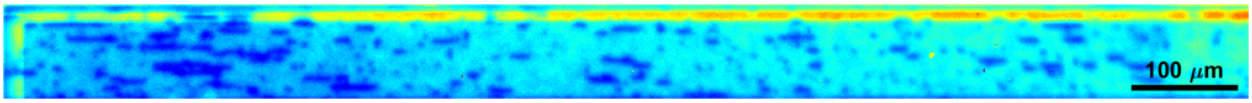
(n) 650 hours



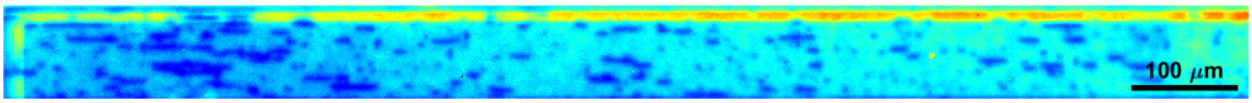
(o) 700 hours



(p) 750 hours



(q) 800 hours

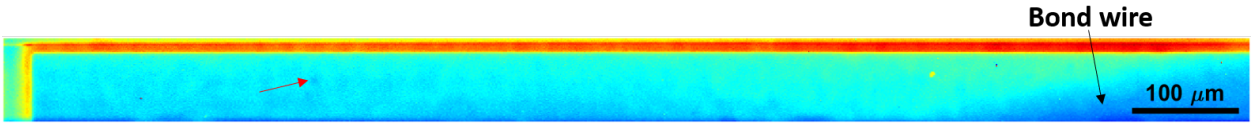


(r) 850 hours

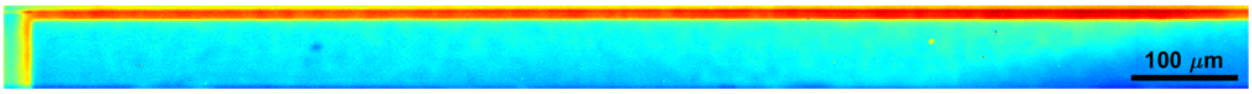
Figure 3.6: Intensity maps of the NIR emission from the n-contact window of device CTNW2 from 0 to 850 hours (10X, $I_{laser} = 0.7A$).

3.2.1.2 Device CTNW3

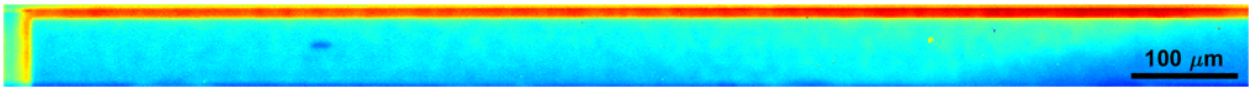
Device CTNW3 is an L0 device and was measured with the TEC stage kept at 25 °C and subjected to level 2 accelerated aging from 0 to 750 hours. Figure 3.7 presents the NIR intensity maps of device CTNW3 at 0.7 A from 0 to 700 hours. A single small dark spot was observed in the 0-hour (fresh) intensity map, as indicated by the red arrow in Figure 3.7). Note that the large dark region on the right side of the image corresponds to a bond wire obstructing the camera view. The initial small dark spot developed into a dark line after aging, with propagation observed after each aging step. After 400 hours of aging, another dark line, originating from the same initial dark spot and located very close to the first dark line, started to propagate. Between 700 hours and 750 hours, the second dark line exhibited a significant propagation length of approximately 460 μm. Throughout the aging period from 0 to 700 hours, device CTNW3 exhibited a slow decrease of 4.65% in optical power output, along with a 0.71 nm redshift in the lasing wavelength, corresponding to an average temperature increase of approximately 2.73 $^{\circ}C$. However, the optical power output decay rate and the laser wavelength shift rate are much smaller than in device CTNW2 during this period (Figures 3.15a & 3.15b). From 700 to 750 hours, CTNW3 experienced a sudden and pronounced drop in optical power (12.55%), accompanied by a sharp increase of in 0.718 nm lasing wavelength, and thus an average cavity temperature increase of approximately 2.76 $^{\circ}C$, indicating COBD.



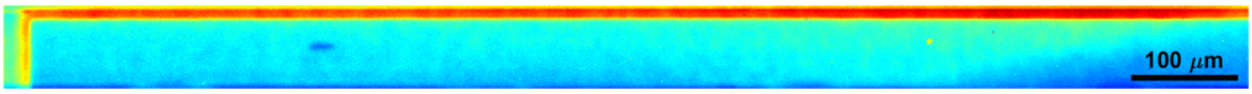
(a) 0 hours



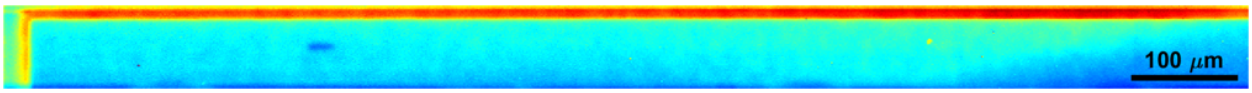
(b) 50 hours



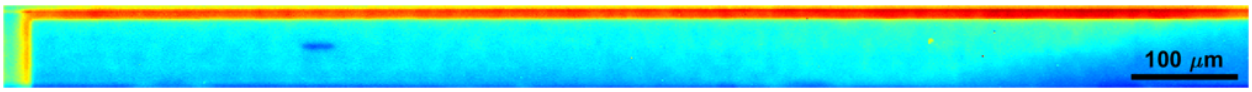
(c) 100 hours



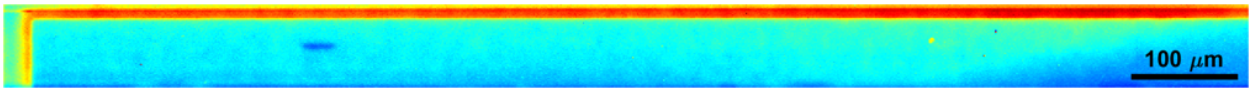
(d) 150 hours



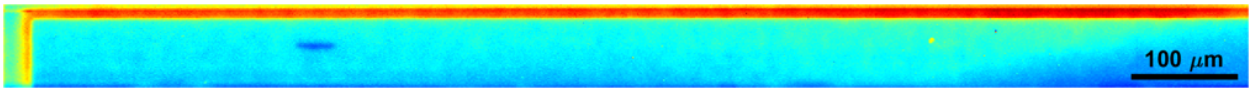
(e) 200 hours



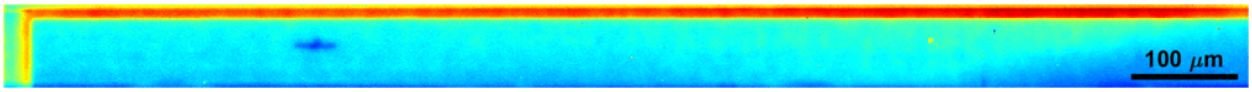
(f) 250 hours



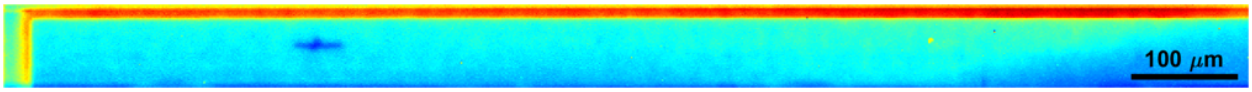
(g) 300 hours



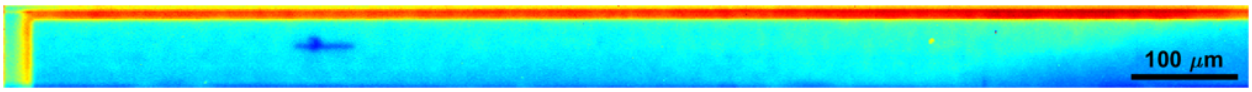
(h) 350 hours



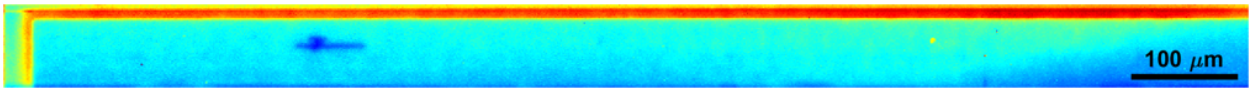
(i) 400 hours



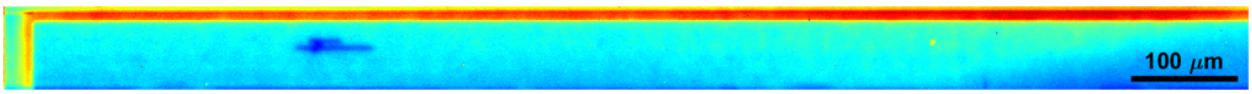
(j) 450 hours



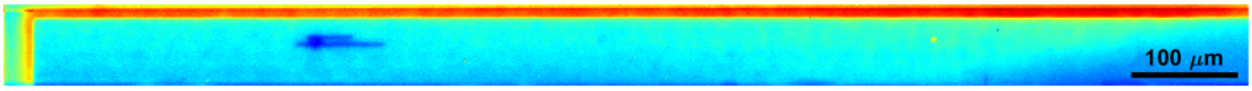
(k) 500 hours



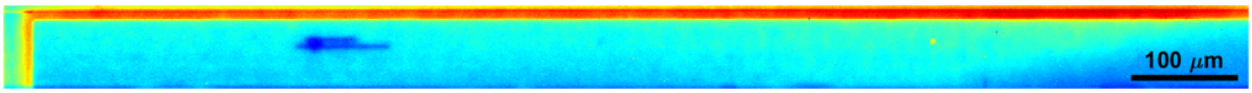
(l) 550 hours



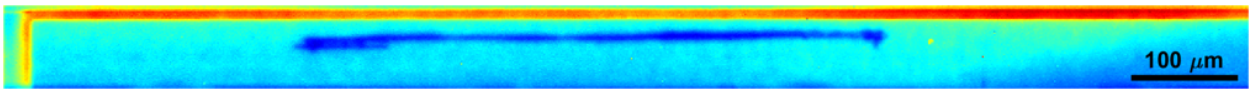
(m) 600 hours



(n) 650 hours



(o) 700 hours



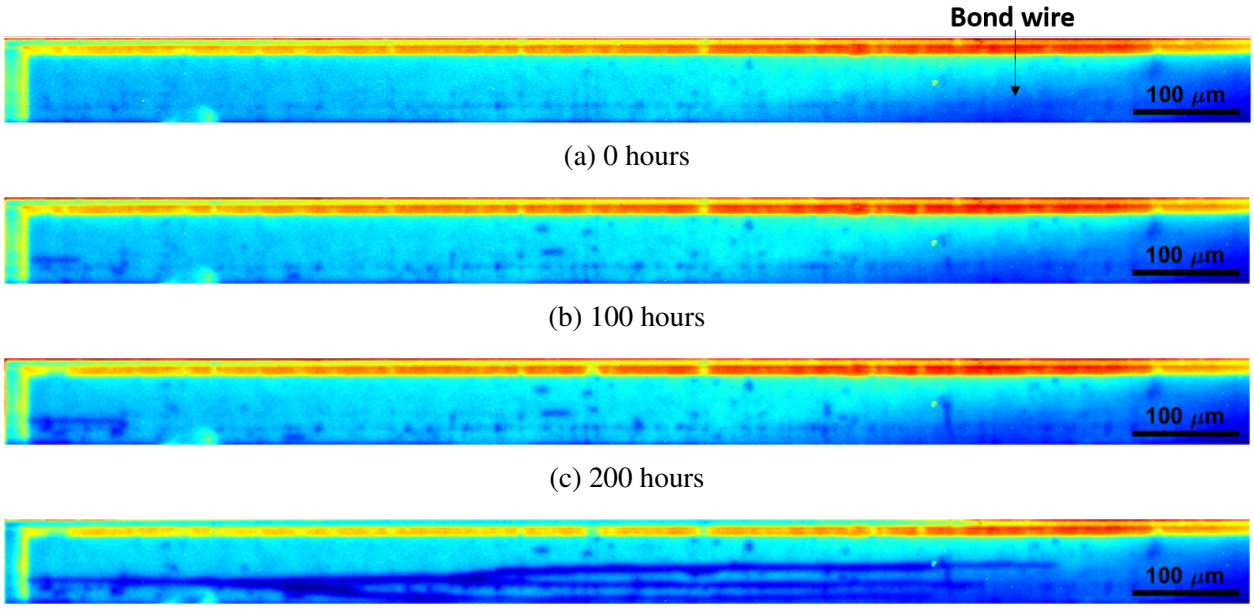
(p) 750 hours

Figure 3.7: Intensity maps of the NIR emission from the n-contact window of device CTNW3 from 0 to 750 hours (10X, $I_{laser} = 0.7A$)

3.2.1.3 Device CTNW4

Device CTNW4 is an L0 device and was measured with the TEC stage kept at 25 °C and subjected to level 2 accelerated aging from 0 to 201 hours. Figure 3.8 shows the NIR intensity maps of device CTNW4 at 0.7 A from 0 to 201 hours. The large dark region on the right side of the intensity maps corresponds to a bond wire blocking the camera view. Some dark spots were observed in the 0-hour (fresh) intensity map, and some were aligned along a thin dark line. During the first 200 hours, several of these dark spots propagated into dark lines. Notably, one dark line near the front facet exhibited fast propagation. Between 200 and 201 hours, this dark line triggered a COBD. One branch of the DLDs formed during the COBD event coincided with the initially observed thin dark line. From 0 to 200 hours, device CTNW4 experienced a gradual optical power decay of 8.13% relative to its initial value, along with a 0.58 nm redshift in lasing wavelength, corresponding to an average temperature increase of approximately 2.2 $°C$. When COBD occurred, the optical

power dropped abruptly by 36.9% of its initial value, and the wavelength redshifted by 1.634 nm, corresponding to an average cavity temperature increase of 6.28 $°C$ (3.15a and 3.15b). The thin dark line observed in the fresh device is likely due to contamination on the substrate and appears to be closely associated with the short lifetime of this device.



(a) 0 hours

(b) 100 hours

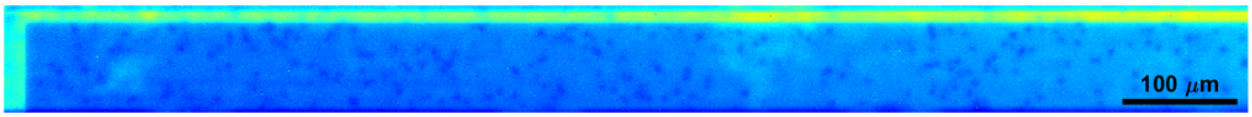
(c) 200 hours

(d) 201 hours

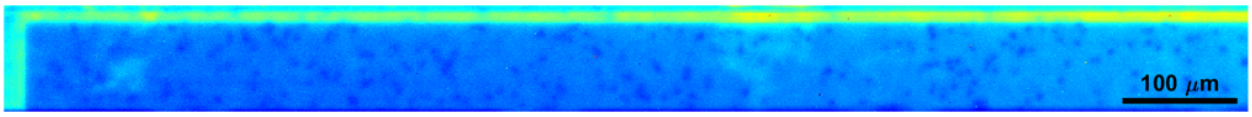
Figure 3.8: Intensity maps of the NIR emission from the n-contact window of device CTNW4 from 0 to 201 hours (10X, $I_{laser} = 0.7A$)

3.2.1.4 Device CTNW5

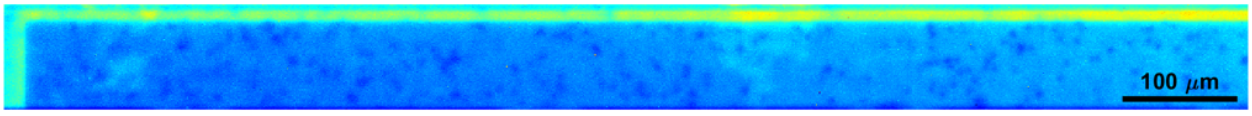
Device CTNW5 is an L0 device and was measured with the TEC stage kept at 10 °C and subjected to regular aging from 0 to 50 hours and level 1 accelerated aging from 50 to 700 hours. Figure 3.9 shows the NIR intensity maps of device CTNW5 at 0.7 A from 0 to 700 hours. Similar to observations in device CTNW2, many small dark spots were observed in the 0-hour (fresh) intensity map of device CTNW5. However, the number of initial dark spots was lower than that observed in CTNW2. Similar to the dark spots observed in previous devices, some of the initial dark spots in device CTNW5 developed into dark lines that propagated with continued aging. A 22.7% decline in optical power during the entire aging period was observed, as shown in Figure 3.15a. The optical power decay in device CTNW5 is slower than that of device CTNW2 but faster than that of device CTNW3, and followed a linear trend. Also, the lasing wavelength redshifted by 0.99 nm over time, indicating a 3.81 $°C$ increase in average cavity temperature, as shown in Figure 3.15b.



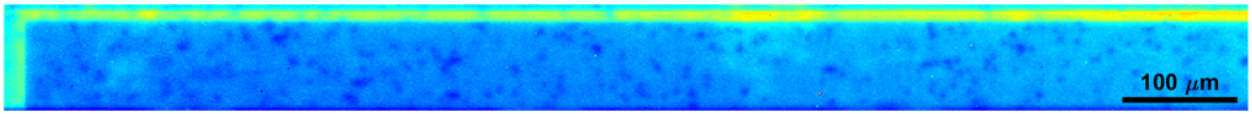
(a) 0 hours



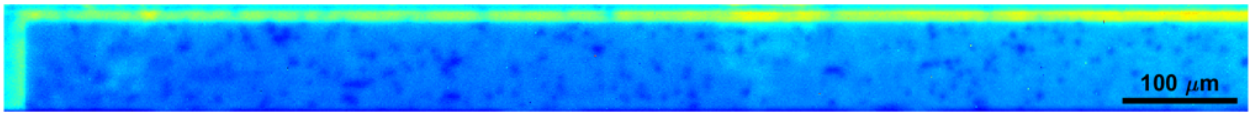
(b) 50 hours



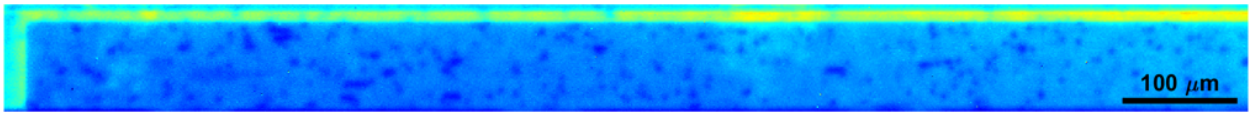
(c) 100 hours



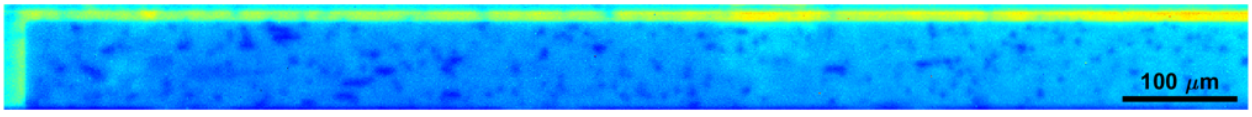
(d) 150 hours



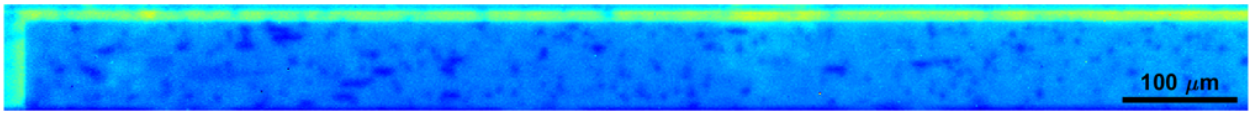
(e) 200 hours



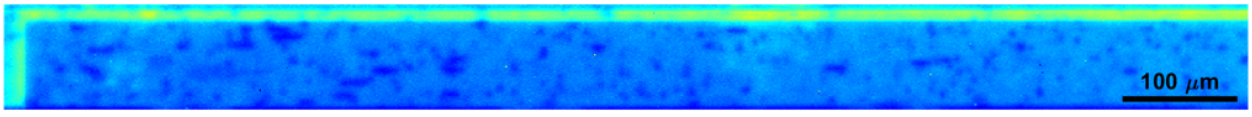
(f) 250 hours



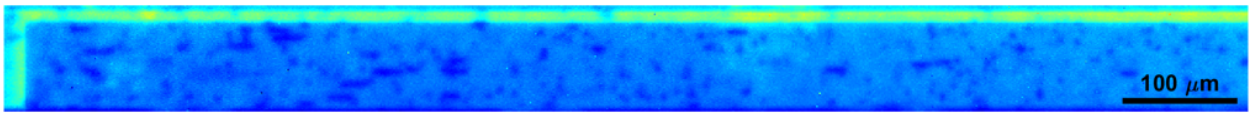
(g) 300 hours



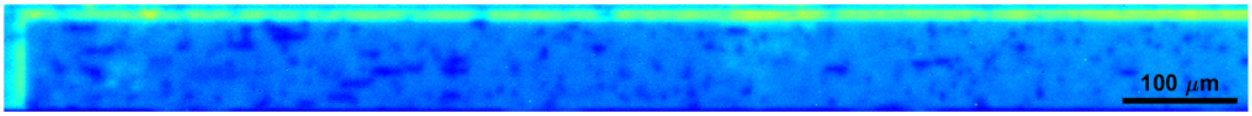
(h) 350 hours



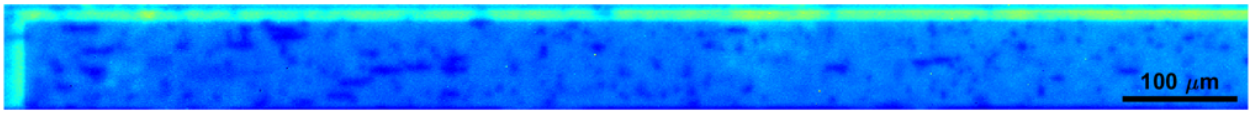
(i) 400 hours



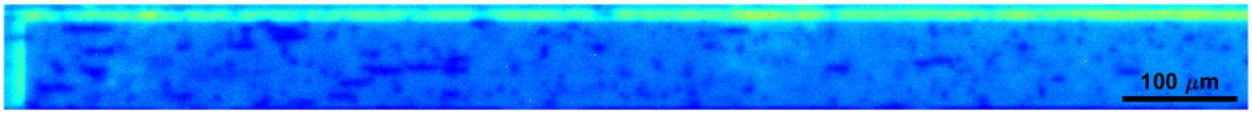
(j) 450 hours



(k) 500 hours



(l) 600 hours

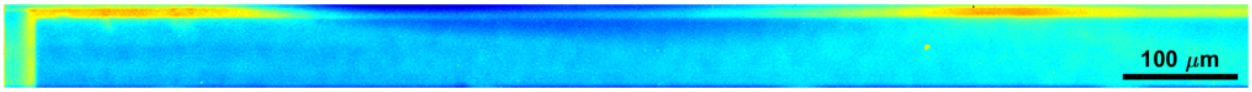


(m) 700 hours

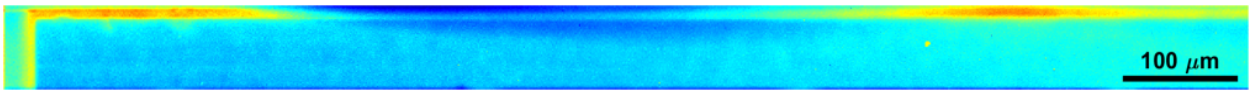
Figure 3.9: Intensity maps of the NIR emission from the n-contact window of device CTNW5 from 0 to 700 hours (10X, $I_{laser} = 0.7A$)

3.2.1.5 Device CTNW10

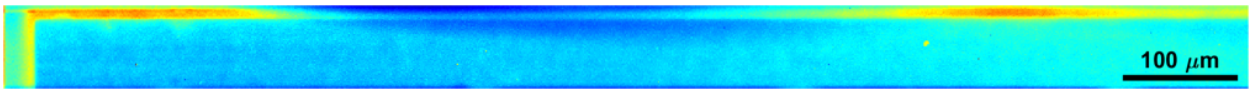
Device CTNW10 is an L0 device and was measured with the TEC stage maintained at 25 °C and subjected to level 2 accelerated aging from 0 to 500 hours. Figure 3.10 displays the NIR intensity maps of the device at 0.7 A over the aging period. Unlike the devices described above, no dark spots were observed in the cavity of device CTNW10 in its fresh state. Furthermore, no dark line formation was observed even after 500 hours of aging. Despite the absence of visible defect propagation, the optical power output of this device declined by 1.36% over the 500-hour period. Concurrently, the lasing wavelength redshifted by 0.78 nm, indicating an approximate 3 $°C$ increase in average cavity temperature (Figures 3.15a & 3.15b). Although dark spots and dark lines are not observed within the 100 μm window region, they may still be present in areas outside the field of view.



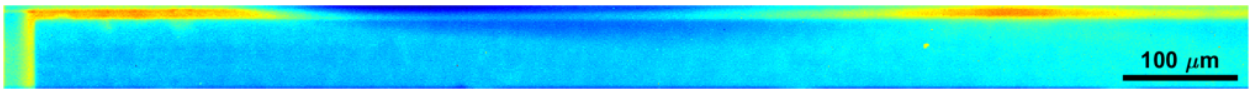
(a) 0 hours



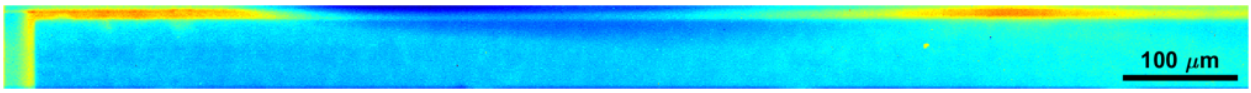
(b) 100 hours



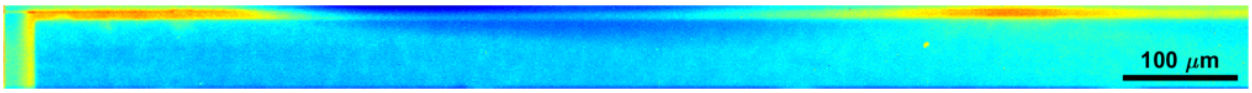
(c) 200 hours



(d) 300 hours



(e) 400 hours

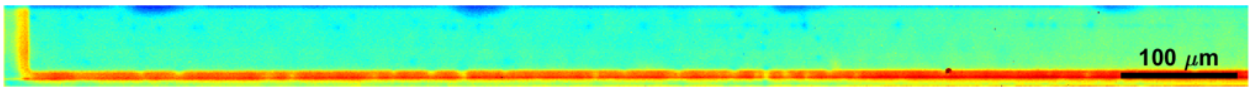


(f) 500 hours

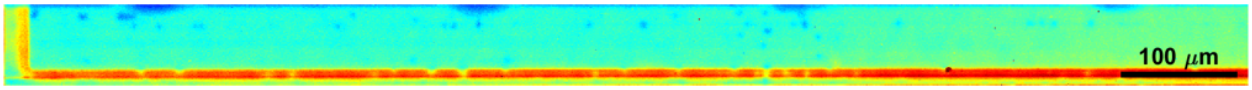
Figure 3.10: Intensity maps of the NIR emission from the n-contact window of device CTNW10 from 0 to 500 hours (10X, $I_{laser} = 0.7A$)

3.2.1.6 Device CTNW11

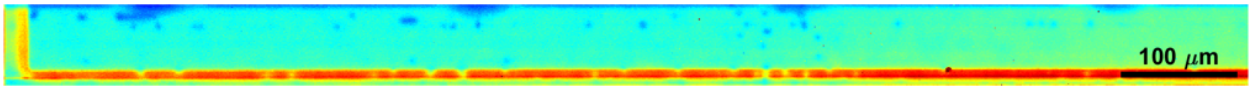
Device CTNW11 is an L0 device and was measured with the TEC stage kept at 25 °C and subjected to level 2 accelerated aging from 0 to 800.5 hours. Figure 3.11 shows the NIR intensity maps of at 0.7 A over the aging process. Several small dark spots were observed in the 0-hour (fresh) intensity map. Similar to observations in previously tested devices, some of these initial dark spots evolved into dark lines that propagated with continued aging. A dark line emerging from the front facet was observed after 300 hours of aging and gradually extended into the cavity by 700 hours. Concurrently, a hot spot was detected at the same location on the front facet, the details of which will be discussed in 3.2.4.7. Over the first 800 hours, the optical power output of device CTNW11 declined by 7.28%, as shown in Figure 3.15a. Simultaneously, the lasing wavelength redshifted by 0.65 nm over time, corresponding to a 2.5 $^{\circ}C$ temperature increase, as shown in Figure 3.15b. Between 800 and 800.5 hours, one of the dark lines triggered a COBD event, resulting in a rapid 6.68% drop in optical power and a 0.18 nm increase in lasing wavelength, corresponding to a 0.69 $^{\circ}C$ increase of average cavity temperature. The optical power drop and lasing wavelength redshift were abrupt but relatively small, likely due to the limited length of the DLDs formed during COBD.



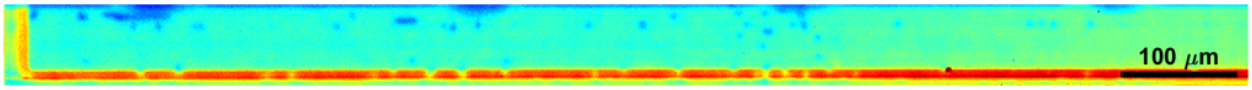
(a) 0 hours



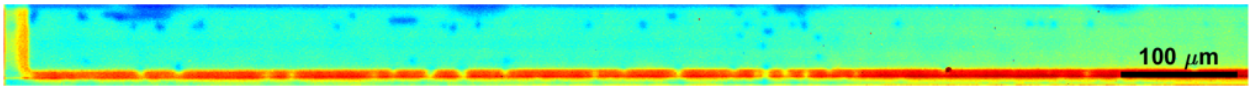
(b) 100 hours



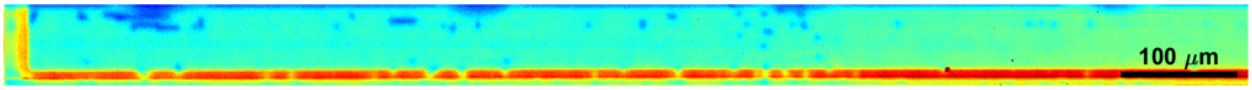
(c) 200 hours



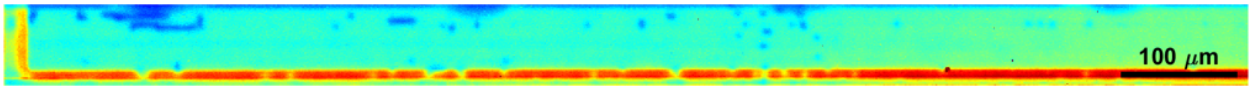
(d) 300 hours



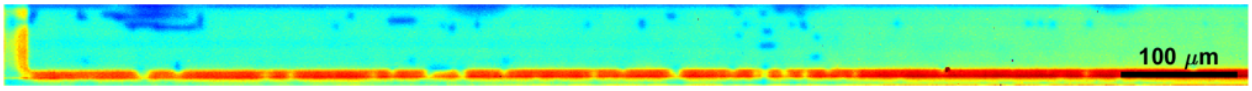
(e) 400 hours



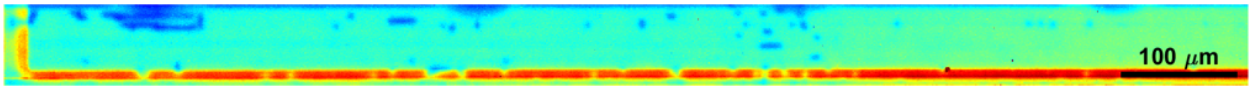
(f) 500 hours



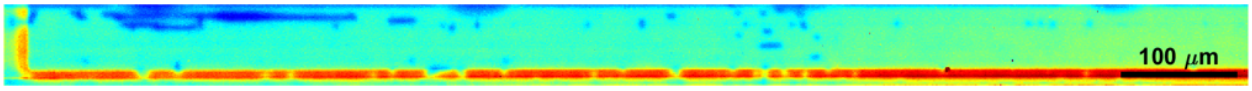
(g) 600 hours



(h) 700 hours



(i) 800 hours

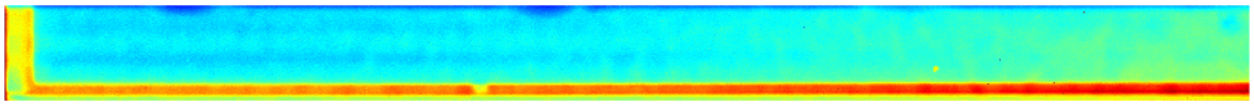


(j) 800.5 hours

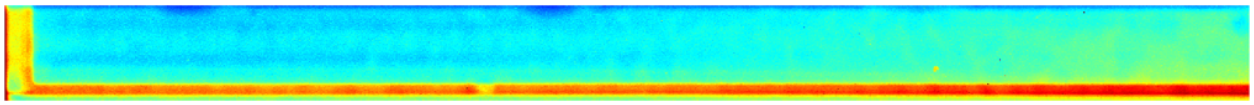
Figure 3.11: Intensity maps of the NIR emission from the n-contact window of device CTNW11 from 0 to 800.5 hours (10X, $I_{laser} = 0.7A$)

3.2.1.7 Device CTNW33

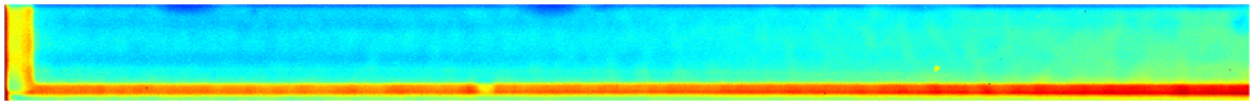
Device CTNW33 is an L1 device and was measured with the TEC stage kept at 10 °C. Figure 3.12 shows the NIR intensity maps of device CTNW33 at 0.7A from 0 to 500 hours. From 0 to 200 hours, device CTNW33 was aged using the regular aging condition. From 200 to 500 hours, it was aged using level 1 accelerated aging condition. No dark spots were observed in the device cavity when its fresh. Also, no dark lines were observed even after 500 hours of aging. Meanwhile, the optical power output fluctuated near 100% over the entire 500-hour aging process. The laser wavelength fluctuated a little in the first 100 hours but stayed nearly the same after that (Figures 3.15a & 3.15b).



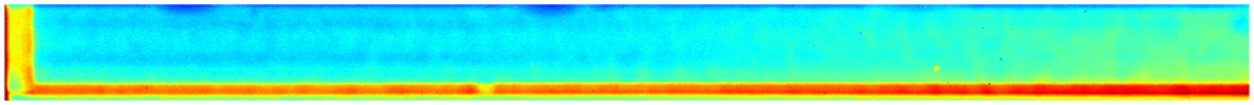
(a) 0 hours



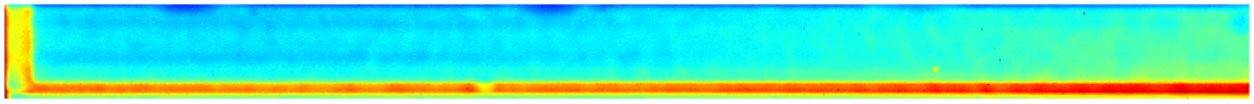
(b) 50 hours



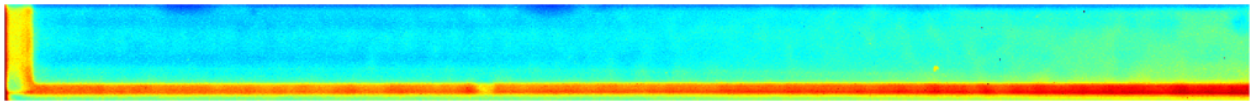
(c) 100 hours



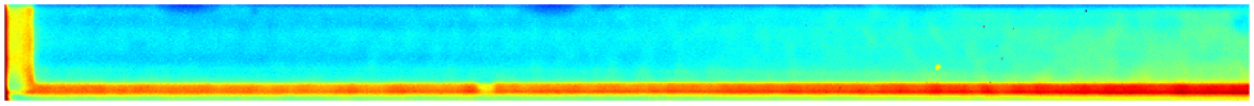
(d) 150 hours



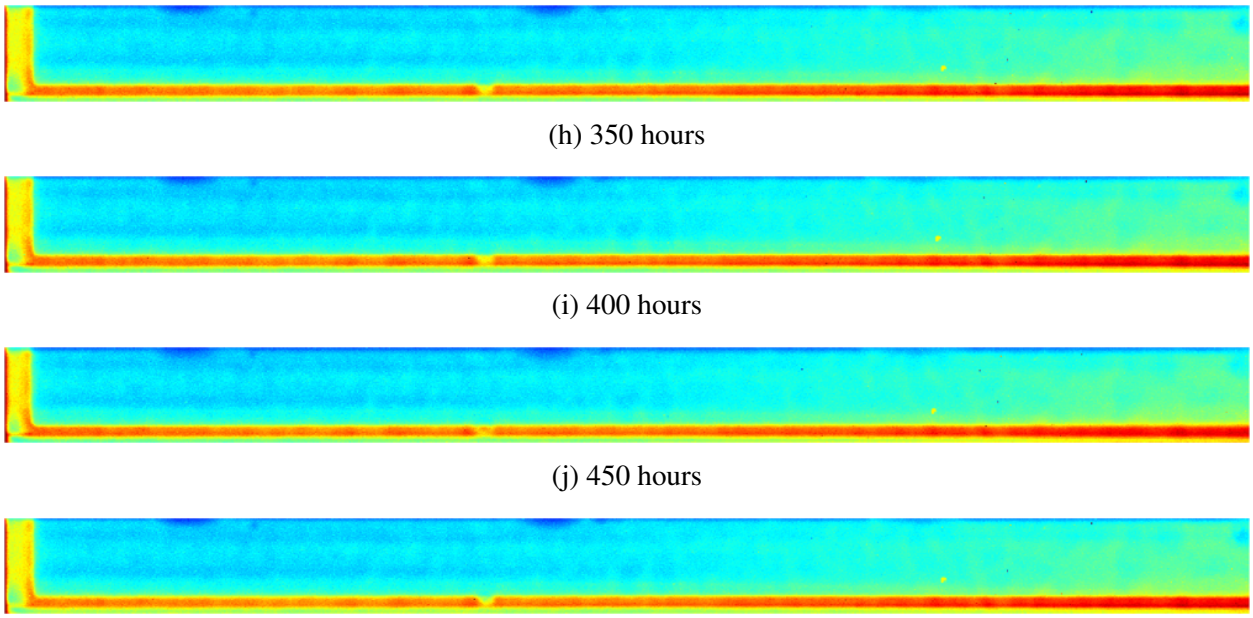
(e) 200 hours



(f) 250 hours



(g) 300 hours



(h) 350 hours

(i) 400 hours

(j) 450 hours

(k) 500 hours

Figure 3.12: Intensity maps of the NIR emission from the n-contact window of device CTNW33 from 0 to 500 hours (10X, $I_{laser} = 0.7A$)

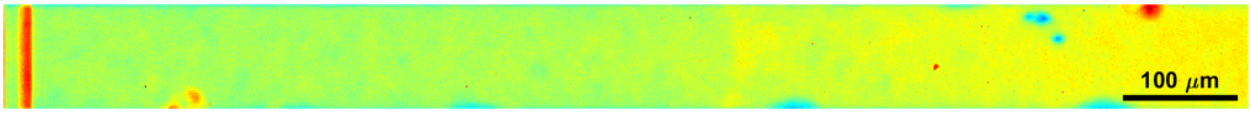
3.2.1.8 Device T120TA

Device T120TA is an L2 device and was measured with the TEC stage kept at 25 °C. Figure 3.12 presents the NIR intensity maps of the device at 0.7 A from 0 to 596 hours. The device underwent level 2 accelerated aging condition over this period. In its fresh state, two dark spots were observed within the cavity region. From 0 to 500 hours, one of the dark spots developed into a dark line that propagated toward both the AR and HR facets. The optical power output increased by 5.28% during the first 200 hours, then declined gradually by 1.21% from 200 to 500 hours, as illustrated in Figure 3.15a. Simultaneously, the lasing wavelength initially blueshifted by 0.27 nm, corresponding to a 1 $^{\circ}C$ decrease in average cavity temperature, but subsequently redshifted by 0.125 nm from 100 to 500 hours, indicating a 0.5 $^{\circ}C$ increase in temperature (Figure 3.15b). Between 500 and 595.5 hours, the device experienced COMD. Multiple dark line (or dark band) branches formed, originating from a point at or near the front facet. This event resulted in a sharp 41%, drop in optical power and a 1.47 nm redshift in the lasing wavelength. After an additional 30 minutes of aging, further propagation of the existing dark lines was observed, and a new dark line emerged from the front facet. During this final stage, the optical power decreased by an additional 31.21%, and the lasing wavelength redshifted by 0.378 nm, corresponding to a 1.45 $^{\circ}C$ increase in average cavity temperature. The initial increase in optical power was also observed in similar

L2 oxygen devices by our collaborators at LLNL and has been described as an incubation period [142].



(a) 0 hours



(b) 100 hours



(c) 200 hours



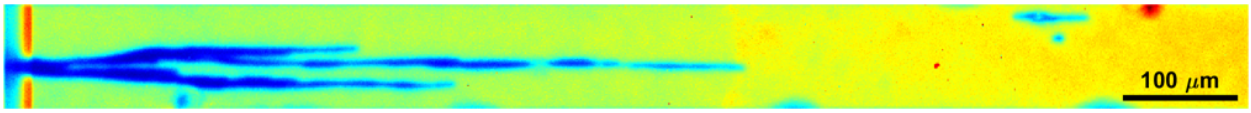
(d) 300 hours



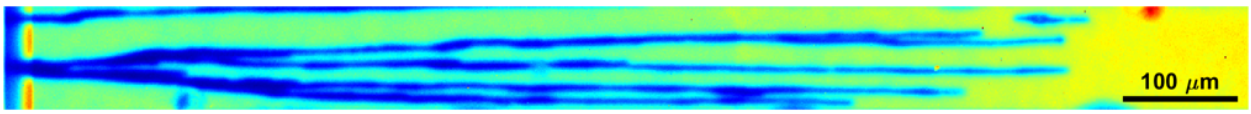
(e) 400 hours



(f) 500 hours



(g) 595.5 hours



(h) 596 hours

Figure 3.13: Intensity maps of the NIR emission from the n-contact window of device T120TA from 0 to 596 hours (10X, $I_{laser} = 0.7A$)

3.2.1.9 Device T120Z9

Device T120Z9 is an L2 device and was measured with the TEC stage kept at 25 °C. Figure 3.14 shows the NIR intensity maps of the device at 0.7 A from 0 to 2202.5 hours. The corresponding aging conditions are summarized in Table 3.1. No dark spots were observed in the cavity of the fresh device, and no dark lines were detected even after 2202.5 hours of aging. After 2202.5 hours, the aging current was increased to 5.5 A, which immediately triggered COMD.

Hours	Aging Current (A)	TEC temperature ($^{\circ}C$)
0-250	3.75	20
250-1900	4	50
1900-1950	4.25	50
1950-2000	4.5	50
2000-2050	4.75	50
2050-2200	5	50
2200-2200.5	4.25	25
2200.5-2201	4.5	25
2201-2201.5	4.75	25
2201.5-2202	5	25
2202-2202.5	5.25	25
above 2202.5	5.5	25

Table 3.1: Aging conditions over the lifetime of device T120Z9

Numerous dark lines (or bands) originating from the facet were observed in the intensity map at 2202.5 hours. This failure was attributed to the optical power reaching the COD threshold (P_{COD}) discussed in 1.2.3. It is important to note that aging was paused after 250 hours, and the device was stored in a drybox during this interval, which lasted several months. During the initial 250-hour aging period, the optical power output fluctuated around 100% of its original value. A slight blueshift in the lasing wavelength was observed during the first 100 hours, which then stabilized. After aging resumed and the device was aged up to 300 hours, the optical power increased to 103.58% of its initial value, accompanied by a 0.313 nm blueshift in the lasing wavelength. This behavior suggests that some degree of annealing may have occurred during the storage period, potentially contributing to the observed increase in optical power and wavelength blueshift. From 300 hours to 2200 hours, the optical power increased by 2.65%, and the lasing wavelength exhibited a slight redshift of 0.095 nm. Notably, no significant gradual degradation was observed over the

2200-hours aging period. The underlying mechanism responsible for the apparent annealing effect remains unknown at this time. After the COMD event, the optical power declined by 92.32%, and the lasing wavelength reshifted by 6.023 nm, corresponding to a 23.16 $^{\circ}C$ increase in average cavity temperature (Figures 3.15a & 3.15b).



(a) 0 hours



(b) 50 hours



(c) 100 hours



(d) 150 hours



(e) 200 hours



(f) 250 hours



(g) 300 hours



(h) 400 hours



(i) 500 hours



(j) 600 hours



(k) 700 hours



(l) 800 hours



(m) 900 hours



(n) 1000 hours



(o) 1100 hours



(p) 1200 hours



(q) 1300 hours



(r) 1400 hours



(s) 1500 hours



(t) 1600 hours



(u) 1700 hours



(v) 1800 hours



(w) 1900 hours



(x) 1950 hours



(y) 2000 hours



(z) 2050 hours



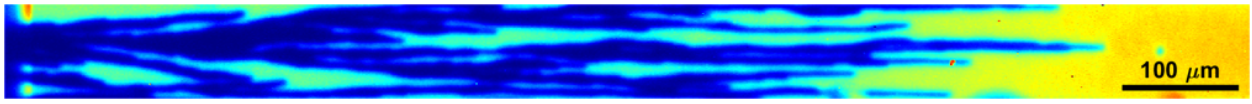
(aa) 2100 hours



(ab) 2150 hours



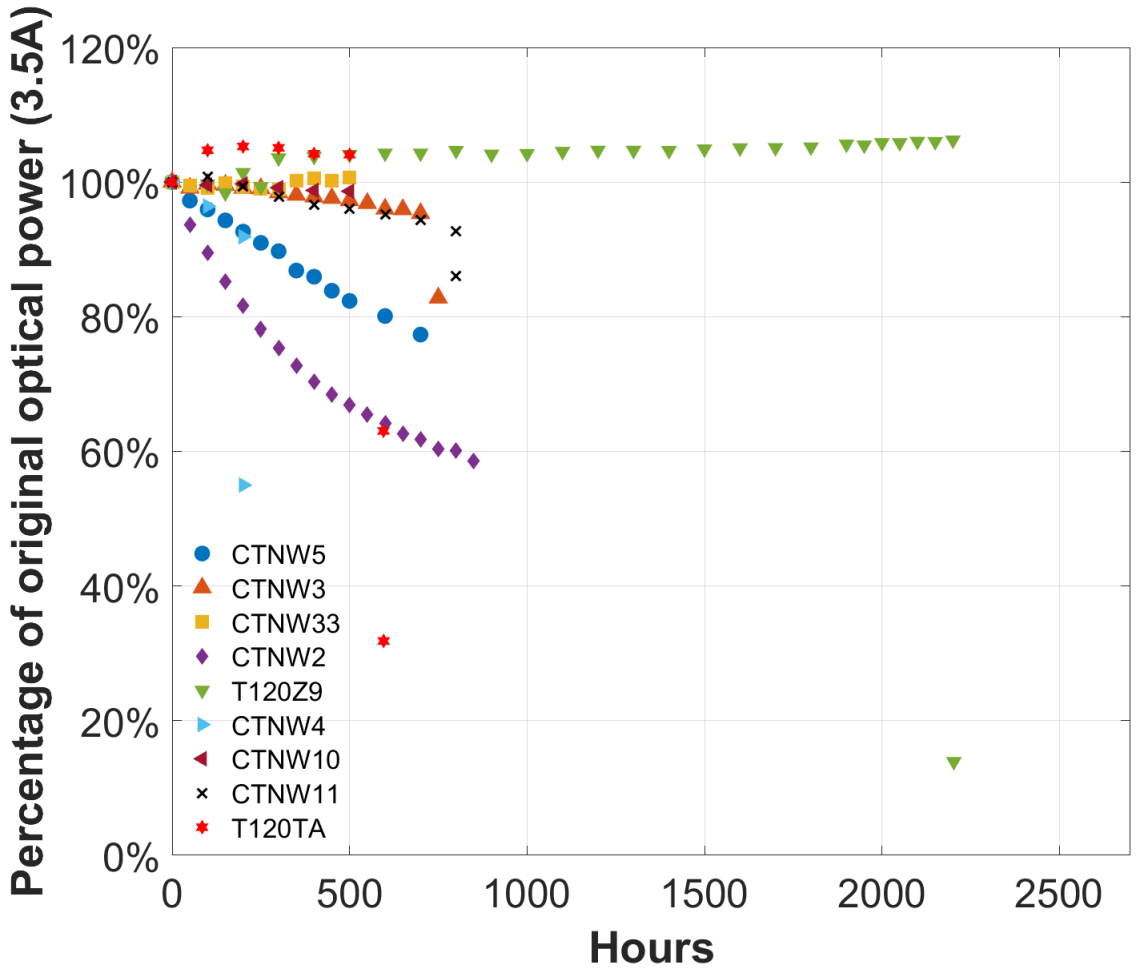
(ac) 2200 hours



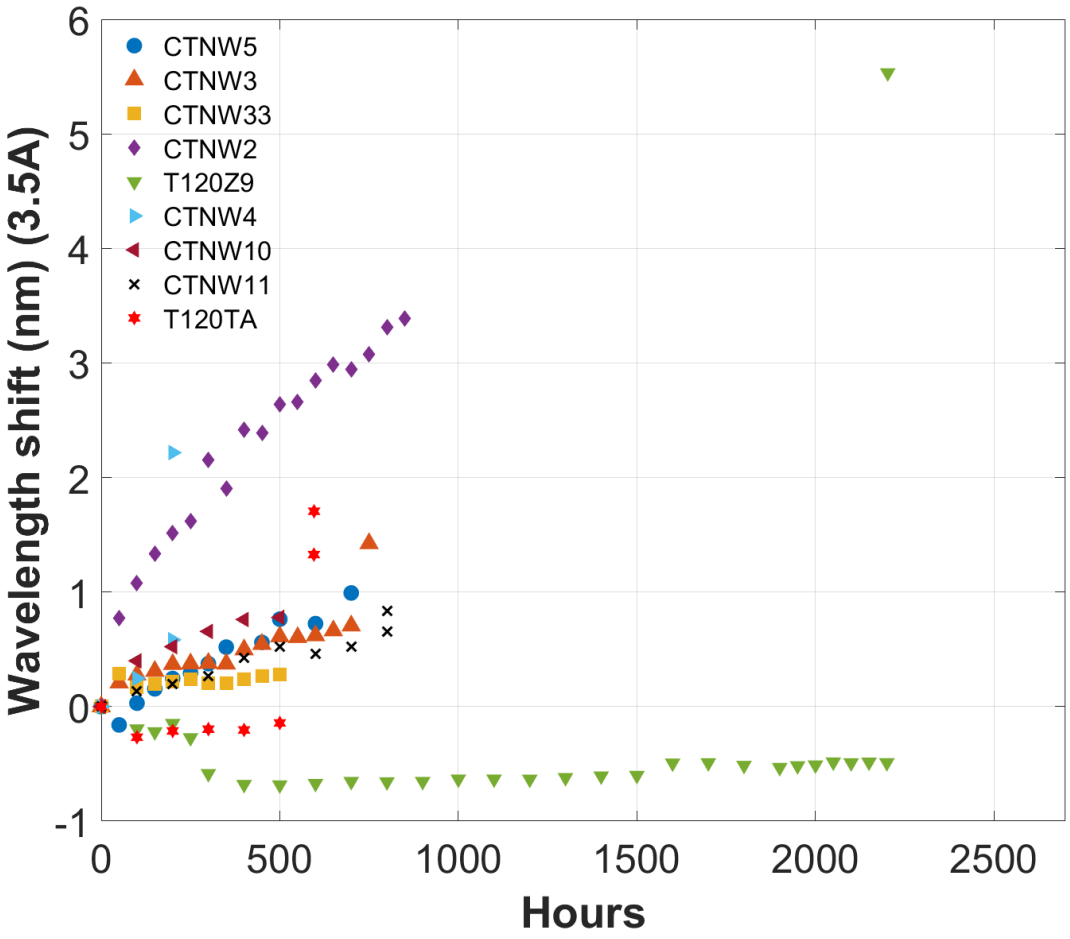
(ad) 2202.5 hours

Figure 3.14: Intensity maps of the NIR emission from the n-contact window of device T120Z9 from 0 to 2202.5 hours (10X, $I_{laser} = 0.7A$)

3.2.2 Optical Power and Centroid Wavelength Shift



(a)



(b)

Figure 3.15: a) Optical power change vs. aging at 3.5A. b) Wavelength shift from fresh device condition at 3.5A.

Although the TEC stage was kept at different temperatures while measuring these devices, it does not affect how the intensity maps, optical power, and lasing wavelength change with aging. So, it is reasonable for us to compare the optical power change and wavelength shift of these devices. Comparing the trends in optical power output and lasing wavelength shift in Figure 3.15a & 3.15b, it is clear that there is a strong correlation between the number of dark lines in the cavity and device degradation. A greater number of dark lines (or a longer length of dark line propagation) is correlated with a more rapid decay in optical power output decay, and a greater lasing wavelength redshift (i.e., a hotter cavity). The correlation is further supported by the plot shown in Figure 3.16, where the x-axis represents the optical power measured after each aging step, and the y-axis denotes the number of "dark" pixels caused by DLD propagation (defined as pixels with intensity reductions greater than 4.5%).

This correlation between the dark line propagation in NIR intensity maps and device performance

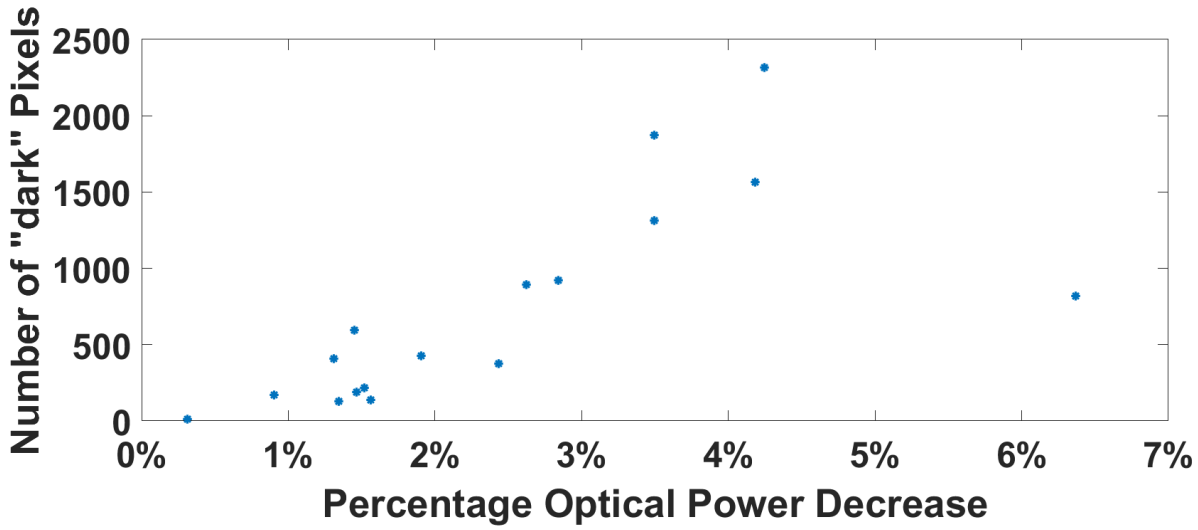


Figure 3.16: Correlation between the number of ”dark” pixels caused by DLD propagation and the optical power decrease for device CTNW2.

degradation suggests that the dark spots and dark lines are defects that cause increased local non-radiative recombination for both deep-level transitions (NIR emission) and interband transitions (fundamental laser emission). Thus, a distribution profile of defects that cause device degradation can be acquired by imaging in the NIR range.

3.2.3 LBIC Results

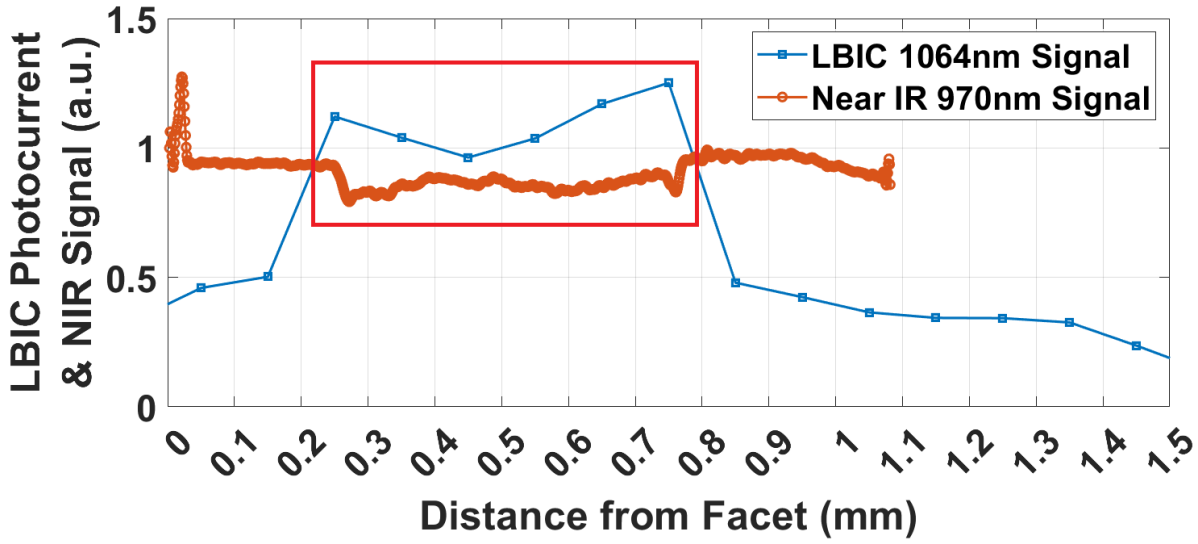


Figure 3.17: Comparison of NIR emission and laser beam induced current (LBIC) signals along the optical axis of device CTNW3 at 750 hours of aging with the region in which a large dark line is observed indicated by a red box.

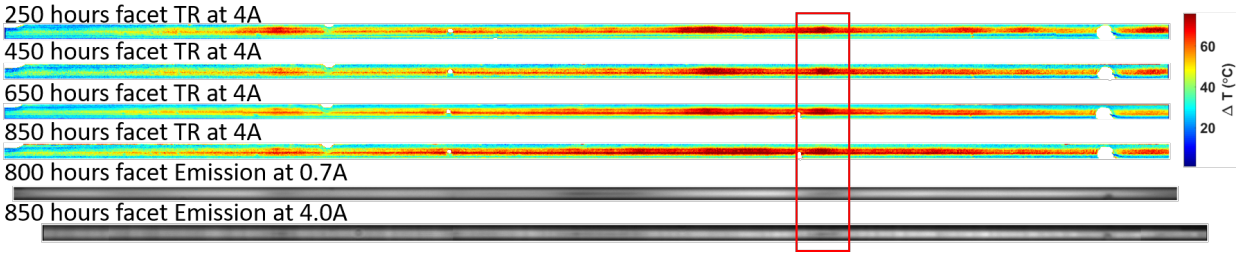
Figure 3.17 compares normalized laser beam induced current (LBIC) and NIR emission signals measured along the optical axis of device CTNW3, where the LBIC excitation wavelength is 1064 nm. Details about the LBIC setup used for this measurement can be found in a previous publication of our collaborators [159]. The NIR signal is only shown for a short distance along the cavity length due to bond wire blocking. Increased 1064 nm LBIC signal (defect absorption) can be observed in the region where the long dark line defect is located in Figure 3.7, which showed suppressed NIR emission. These results indicate that the growing dark line defects are linked to a local increase in defect absorption.

3.2.4 Thermoreflectance Results

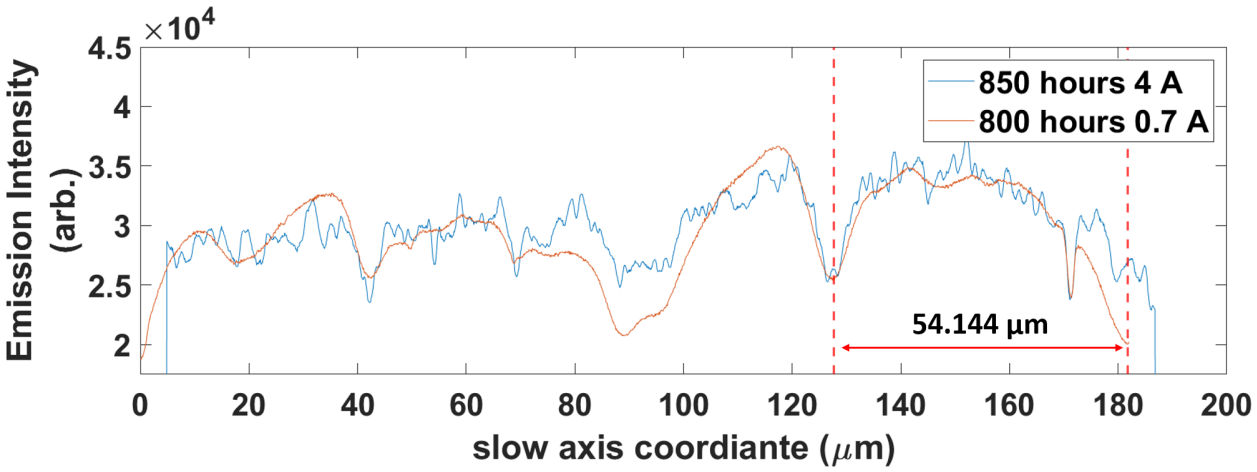
Thermal profiles were measured at 4 A for devices CTNW2, CTNW3, CTNW4, CTNW10, CTNW11, T120TA, and T120Z9 throughout their lifetimes. In this section, thermal profiles at selected time points are presented; the complete set is provided in Appendix A.

3.2.4.1 CTNW2

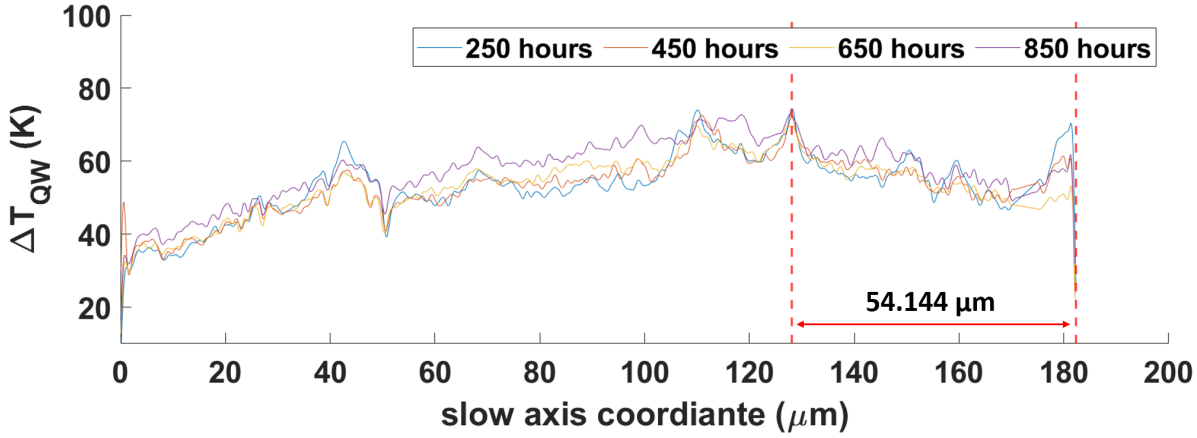
As mentioned in the 3.2.1.1, a dark line originating from the front facet was observed to start propagating into the cavity. A corresponding hot spot at the same location was detected on the front facet, as boxed out in Figure 3.18a. Additionally, the laser's near-field emission profile reveals a dark spot in the same region. Figure 3.18b and 3.18c display the averaged near-field emission profile and facet temperature profile along the slow axis, respectively. The hot spot and dark spot boxed out in Figure 3.18a are located approximately 54 μm from the emitter's right ridge. Figure 3.18d shows the averaged NIR intensity near the front facet along the slow axis. The dark line referenced in 3.2.1.1 is found to be approximately 53 μm away from the right ridge, aligning closely with the location of the hot and dark spots. These results indicate that DLDs can originate from the front facet and propagate into the cavity, leading to the formation of hot spots and dark spots at the facet. However, it is important to note that not every hot spot observed on the front facet is necessarily caused by a DLD.



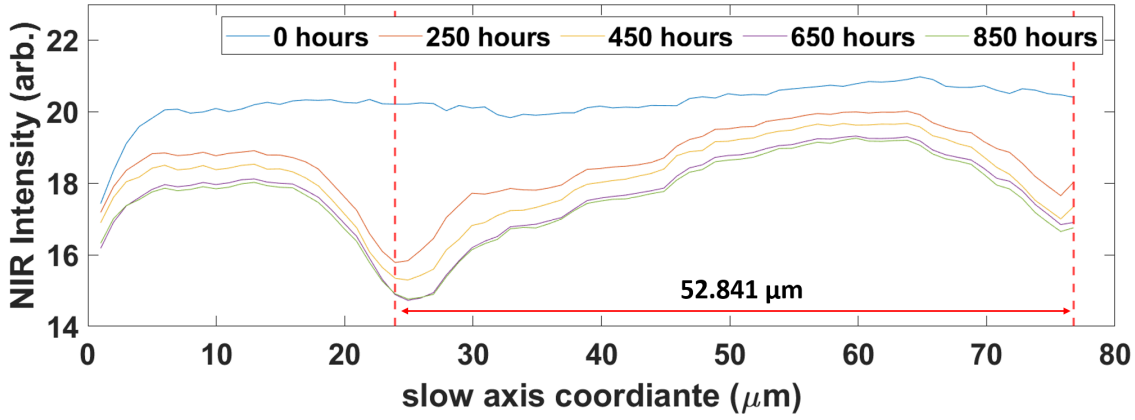
(a)



(b)



(c)



(d)

Figure 3.18: a) Selected 2D thermal profiles of device CTNW2 at 4 A, along with near-field laser emission profiles at 800 hours and 850 hours. b) Averaged near-field emission profile along the slow axis. c) Temperature profiles (averaged in the fast axis direction) within the epitaxial layers at the facet along the slow axis. d) Averaged NIR intensity near the front facet along the slow axis.

3.2.4.2 CTNW3

Figure 3.19 presents selected 2D thermal maps of device CTNW3 at 4 A from 0 to 750 hours. Two distinct hot spots emerged during aging; however, neither led to the failure of the device. As discussed in 3.2.1.2, device CTNW3 failed within the cavity between 700 hours and 750 hours. Since the DLD responsible for failure originated deep in the cavity (approximately 280 μm from the front facet), no corresponding hot spot was observed at the facet. An additional noteworthy observation is that the front facet did not exhibit any significant cooling following the COBD event. This may be because the facet itself was not directly damaged by the COBD process, and the associated optical power loss was insufficient to eliminate localized absorption. As a result, a substantial amount of laser light may still have been absorbed by point defect clusters on the facet, leading to the continued presence of localized hot spots.

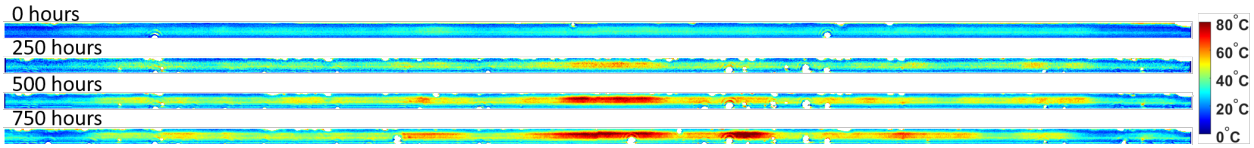


Figure 3.19: Selected 2D thermal profiles of device CTNW3 at 4 A.

3.2.4.3 CTNW4

Figure 3.20 presents the 2D thermal maps of device CTNW4 at 4 A from 0 to 201 hours. While slight temperature increases were observed in certain regions, no significant temperature rise or distinct hot spots were detected on the front facet. This is likely because the device experienced COBD only after 201 hours of aging, as described in 3.2.1.3, and by that time, a substantial number of point defect clusters had not yet formed on the facet. Moreover, similar to observations in device CTNW3, the front facet did not exhibit any noticeable cooling following the COBD event. This may be attributed to the absence of direct facet damage during the COBD process. The DLD responsible for the failure was located approximately 25 μm from the front facet. Despite the proximity of the DLD to the facet, no corresponding hot spot was observed at the facet.

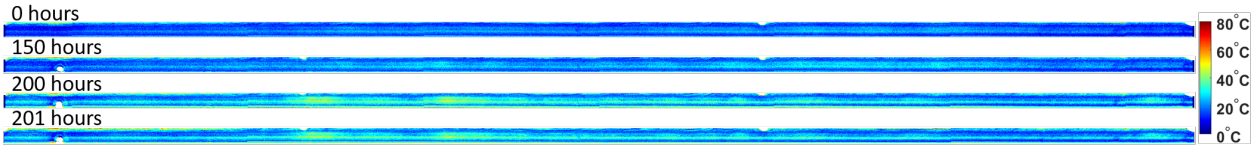


Figure 3.20: Selected 2D thermal profiles of device CTNW4 at 4 A.

3.2.4.4 CTNW10

Figure 3.19 presents selected 2D thermal maps of device CTNW10 at 4 A from 0 to 500 hours. Evident hot spots appeared on the facet as aging progressed. However, as discussed in 3.2.1.5, no DLDs were observed in the cavity, and no significant optical power degradation was detected. These results suggest that the presence of hot spots on the facet may not be the primary cause of gradual optical power decay.

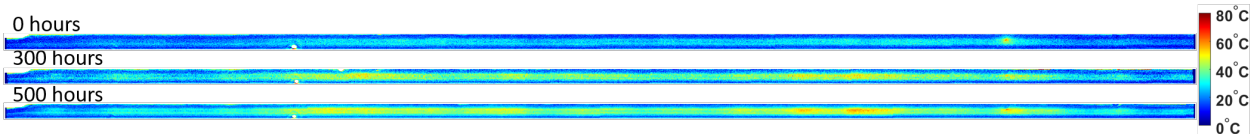
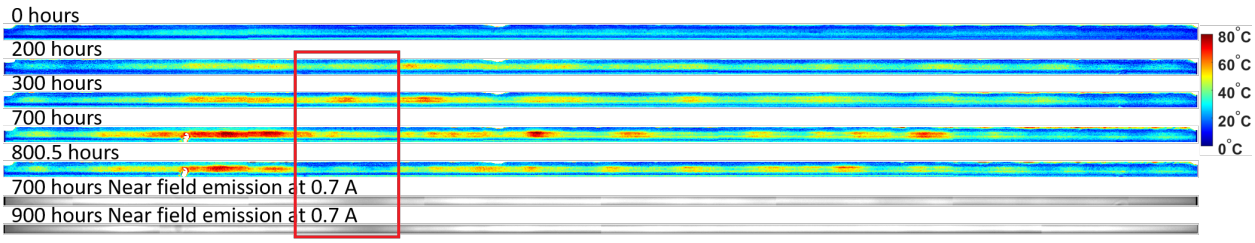


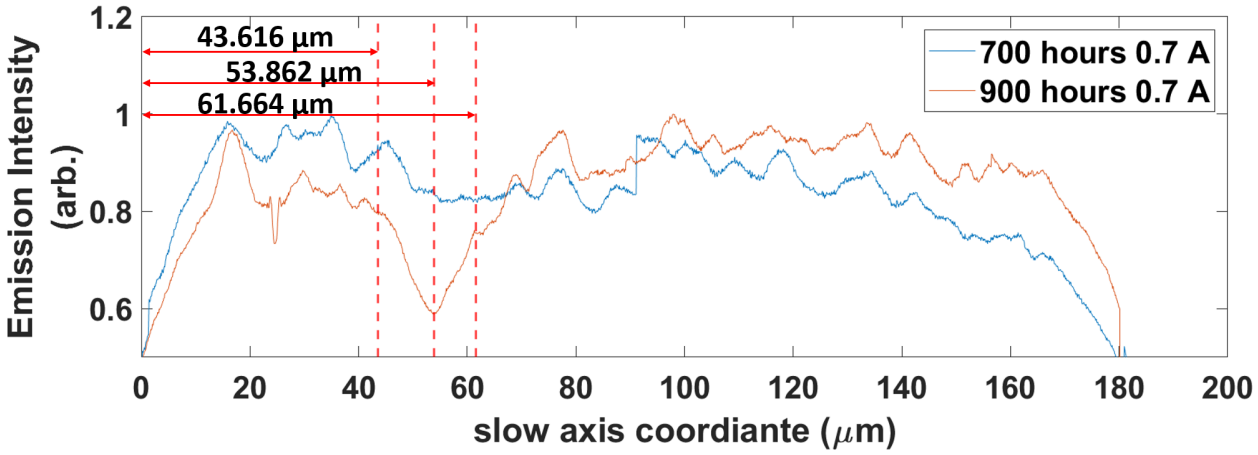
Figure 3.21: Selected 2D thermal profiles of device CTNW10 at 4 A.

3.2.4.5 CTNW11

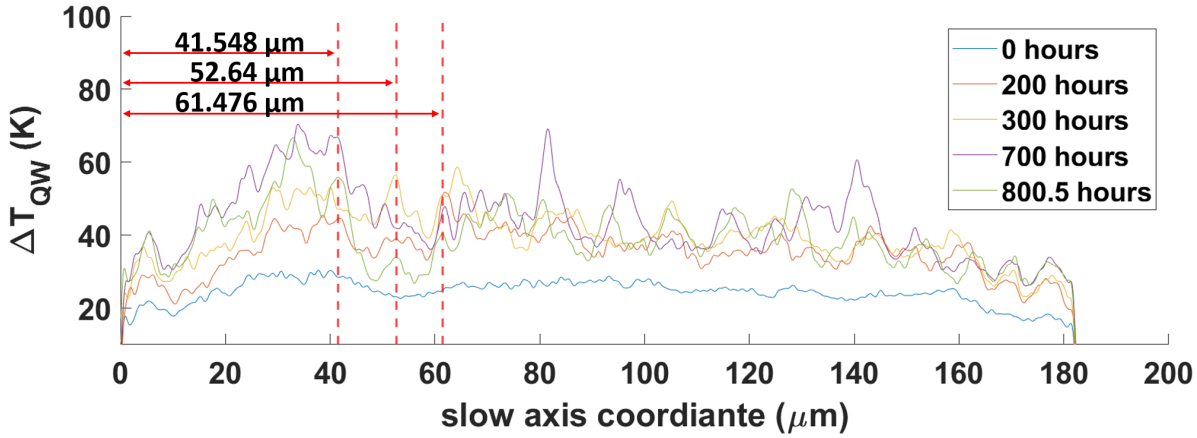
Figure 3.22a presents selected 2D thermal maps of device CTNW11 at 4 A from 0 to 800.5 hours, along with the near-field emission profiles captured before and after failure. Several hot spots emerged throughout the aging process. As described in 3.2.1.6, a DLD originating from the front facet appeared around 300 hours. A corresponding hot spot at the same location on the front facet was observed, as highlighted in Figure 3.22a.A unique observation in this device is that the temperature in the boxed-out region gradually decreased as the device approached failure and dropped significantly following failure. During this period, several other DLDs, located close to the facet and along the same slow-axis coordinate as the facet DLD, continued to propagate with aging. Figures 3.22b and 3.22c show the averaged near-field emission profile and the averaged active region temperature profile along the slow axis, respectively. Vertical dashed lines indicate the region of interest, between approximately 43 μm and 62 μm from the left ridge, where both localized cooling and reduced emission were observed. In the temperature profile, a small peak, representing a localized region of higher temperature, is observed around 53 μm from the left ridge. This position aligns closely with both the lowest-emission point in the near-field profile (Figure 3.22b) and the DLD location identified in the NIR intensity profile near the facet (Figure 3.22d). A possible explanation for the observed localized cooling at the facet, along with the higher-temperature spot in the middle, is that those DLDs located near the facet, along the same slow-axis coordinate as the DLD originating from the facet, absorbed a significant portion of the emitted photons. As a result, fewer photons reached the front facet, leading to reduced total absorption and consequently localized cooling in that region. However, the DLD originating from the facet continued to absorb more light relative to the surrounding area, resulting in a localized temperature peak within the broader cooled region.


0 hours
200 hours
300 hours
700 hours
800.5 hours
700 hours Near field emission at 0.7 A
900 hours Near field emission at 0.7 A
80°C
60°C
40°C
20°C
0°C

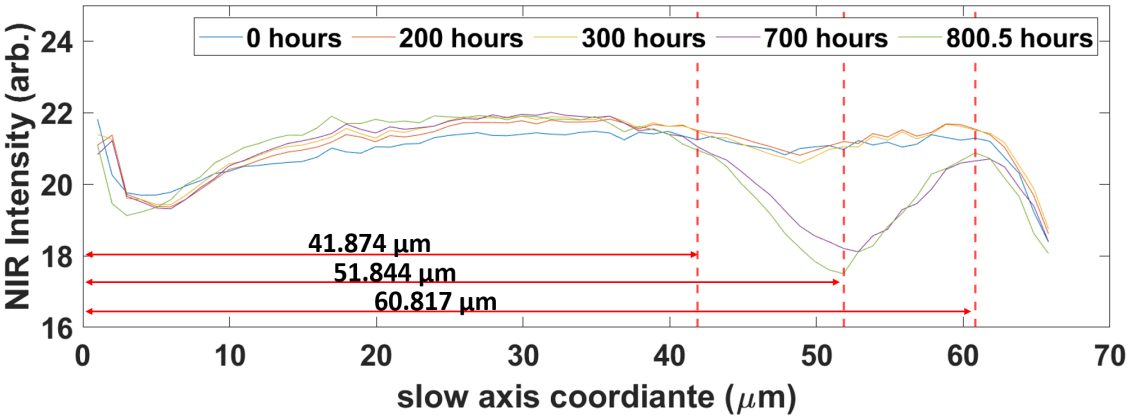
(a)


43.616 µm
53.862 µm
61.664 µm
700 hours 0.7 A
900 hours 0.7 A
Emission Intensity (arb.)
slow axis coordiante (µm)

(b)


41.548 µm
52.64 µm
61.476 µm
0 hours
200 hours
300 hours
700 hours
800.5 hours
ΔT_QW (K)
slow axis coordiante (µm)

(c)



(d)

Figure 3.22: a) Selected 2D thermal profiles of device CTNW11 at 4 A, along with near-field laser emission profiles at 700 hours and 900 hours. b) Averaged near-field emission profile along the slow axis. c) Temperature profiles (averaged in the fast axis direction) within the epitaxial layers at the facet along the slow axis. d) Averaged NIR intensity near the front facet along the slow axis.

3.2.4.6 T120TA

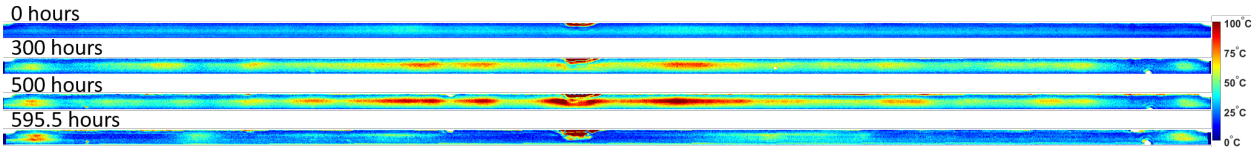
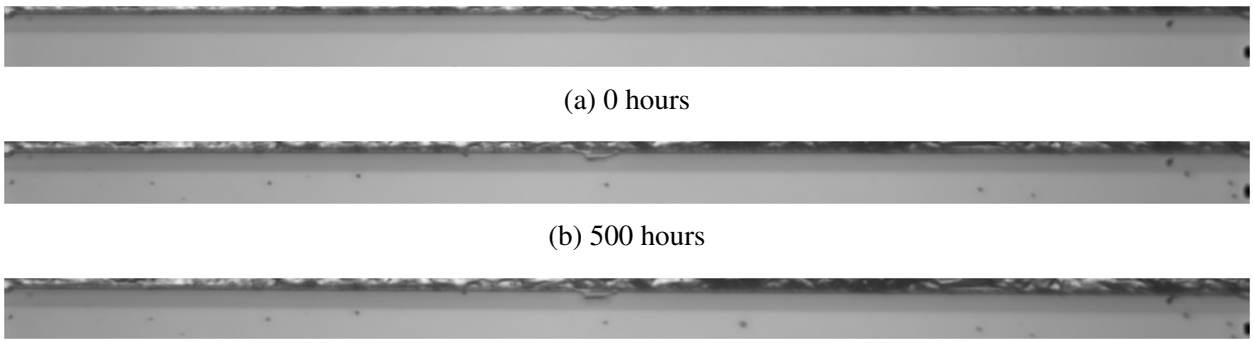


Figure 3.23: Selected 2D thermal profiles of device T120TA at 4 A.

Figure 3.23 presents selected 2D thermal maps of device T120TA at 4 A from 0 to 595.5 hours. A piece of foreign matter is visible in the middle of the stripe from the beginning of the aging process (0 hours). As shown in the DC images in Figure 3.24, this foreign matter appears to be solder that has invaded the epitaxial layer. Unlike the foreign particles described in 2.4.1, which did not influence the degradation process, this solder intrusion expanded with aging and led to the formation of an intense hot spot around it. This eventually triggered COMD of the laser between 500 hours and 595.5 hours, accompanied by visible morphological damage on the facet. Additionally, the entire facet cooled down significantly after the COMD event. It is worth noting that the second DLD branch, which formed between 595.5 and 596 hours (Figure 3.13), did not result in any observable morphological damage to the facet.



(a) 0 hours

(b) 500 hours

(c) 595.5 hours

Figure 3.24: DC images of device T120TA at a) 0 hours, b) 500 hours, c) 595.5 hours.

3.2.4.7 T120Z9

Figure 3.25 presents selected 2D thermal maps of device T120Z9 from 100 to 2202.5 hours. Numerous hot spots emerged during this period, spreading across nearly the entire facet and reaching significantly elevated temperatures. Following the COMD event, the facet temperature dropped dramatically. Although multiple DLD branches were observed originating from the front facet, as shown in Figure 3.14, the COMD process did not result in any visible morphological damage to the facet.

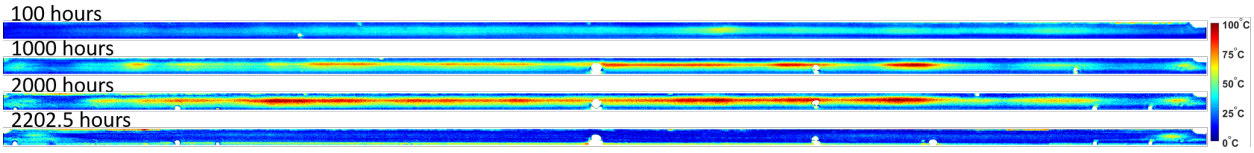


Figure 3.25: Selected 2D thermal profiles of device T120Z9 at 4 A.

3.2.5 Discussion

In summary, the dark spots and dark lines observed in the cavity correspond to defects. Most of the dark lines were found to originate from pre-existing dark spots located within the interior of the fresh device, which were likely introduced during the manufacturing process. Capturing intensity maps of broadband NIR emission through the n-contact window thus provides an in situ, non-destructive, and efficient method for monitoring dark line defect formation and propagation in high-power diode laser cavities during operation. This technique can serve not only as a screening tool for assessing device reliability but also as a diagnostic method for evaluating the influence of various manufacturing processes on defect generation and overall device performance.

As mentioned in 3.2.1, the devices under test were fabricated with three different artificial oxygen doping concentrations: L0 (CTNW2, CTNW3, CTNW4, CTNW5, CTNW10, CTNW11), L1 (CTNW33), and L2 (T120Z9, T120TA). Previous studies have shown that oxygen incorporation can degrade threshold current and slope efficiency in AlGaAs/GaAsP and AlGaAs/InAlGaAs laser structures [160][161][162], which intuitively suggests that oxygen doping may negatively impact device reliability. However, among the devices we evaluated, 5 out of 6 undoped (L0) devices exhibited gradual degradation, whereas only 1 out of 3 oxygen-doped (L1 and L2) devices showed such behavior. Notably, one highly doped device (T120Z9) demonstrated a significantly longer lifetime than all others. These observations suggest that, contrary to earlier notions, oxygen doping may play a role in suppressing gradual degradation rather than accelerating it. A similar conclusion was drawn by our collaborators at LLNL using a complementary set of diagnostics [142].

As discussed in the same publication by our collaborators at LLNL, the nature of these DLDs shown in the NIR maps involves aggregates of multiple dislocations, suggesting that their propagation is likely more complex than the simple glide and climb mechanisms described in 1.3.2 [142]. Previous studies have shown that point defects can facilitate dislocation motion [163], [164]. As illustrated by our collaborators, the aggregation of dislocations in our devices is likely enhanced by interactions with phosphorus vacancies (V_P) [142].

The cavity NIR intensity maps, front facet temperature profiles, and PIV data collectively indicate that DLD propagation within the cavity is the primary contributor to optical power degradation and lasing wavelength shift. In contrast, the impact of facet absorption on optical power decay appears to be limited. DLDs originating from the facet can lead to localized heating and the appearance of dark spots on the front facet; however, not all hot spots are directly linked to cavity DLDs. Only catastrophic optical mirror damage (COMD) results in abrupt cooling across the entire facet. In contrast, hot spots on the facet often persist even after catastrophic optical bulk damage (COBD). Furthermore, although COMD events often result in prominent dark lines originating from the facet, many COMD occurrences do not produce visible morphological damage on the front facet.

Another observation is that for devices exhibiting significant optical power loss, whether due to gradual degradation or COD, the NIR emission near the AR facet is quenched. This quenching effect can be attributed to the non-injecting mirror configuration of the devices under test, where carrier generation near the facet primarily relies on photon absorption. As the optical output power decreases substantially, fewer photons are available for absorption, resulting in a reduced carrier population near the AR facet. Consequently, spontaneous emission of the NIR light in this region is significantly diminished.

CHAPTER 4

Photon-accelerated REDG Mechanism

As discussed in chapter 3, the growth of DLDs creates non-radiative recombination centers and leads to performance decline. Consequently, the growth rate of DLDs has a direct impact on the degradation rate of a device. Gaining insight into the spatial dependence of DLD growth within the laser cavity can reveal regions that are more susceptible to degradation and help identify the dominant mechanisms driving laser failure.

In this chapter, we discuss the longitudinal (along the cavity) position dependence of DLD growth velocity observed in diode laser cavities. The DLD growth velocity is quantified using the NIR defect imaging technique introduced in chapter 3. Based on the observed spatial variation in DLD growth rate along the cavity length, we propose a photon-accelerated mechanism as an important contributor to the enhancement of DLD propagation in diode laser cavities.

As introduced in chapter 1, two key effects contribute to dislocation-driven DLDs formation: recombination enhanced dislocation climb (REDC) and recombination enhanced dislocation glide (REDG). REDC is typically associated with DLDs along the $\langle 100 \rangle$ direction, while REDG is linked to DLDs along the $\langle 110 \rangle$ direction. As mentioned in chapter 3, $\langle 1\bar{1}0 \rangle$ DLDs were observed in our devices, and the propagation of these DLDs is likely more complicated than simple glide and climb motion. In 4.1, we first introduce two mechanisms that have been identified as contributors to the enhancement of DLD propagation. In the following sections, we present our observations on the longitudinal spatial dependence of DLD growth rate and discuss the proposed photon-accelerated mechanism that leads to this behavior.

4.1 Mechanisms behind REDG Effect

4.1.1 Phonon-kick Mechanism

The first quantitative theory of recombination enhanced defect motion in semiconductors was developed by Weeks et al. in 1975 [88]. In this model, a defect with an energy level deep in the

energy band gap of a semiconductor is treated as a "defect molecule", made up of S loosely coupled oscillators. The theory assumes that defect diffusion is triggered if and only if the defect energy exceeds a critical threshold E^*, which was demonstrated experimentally by Kimerling and Lang [15]. As illustrated in Figure 4.1, for a defect state lying ΔE_c below the conduction band, when a carrier, either a hole or an electron, is captured by this defect, energy is released: ΔE_c for electron capture and ΔE_v for hole capture. Theoretically, this energy can be dissipated either radiatively or non-radiatively. Non-radiative pathways include defect recombination and Auger recombination, as discussed in 1.1.3. In this model, defect recombination that deposits the energy into localized vibrational modes is dominant.

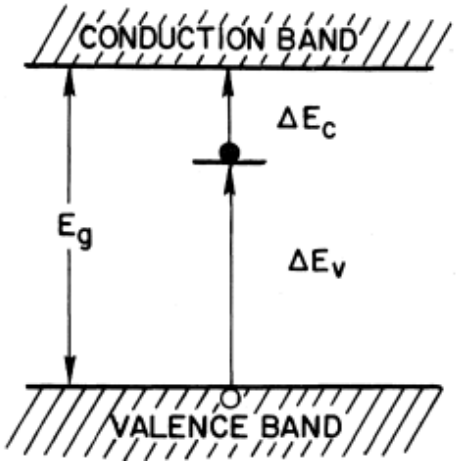


Figure 4.1: Band diagram of a defect energy state in the band gap of a semiconductor [88].

The rate of defect diffusion can be expressed as a function of the defect energy distribution $n(E)$. This distribution is influenced by two factors: (1) interactions between defect molecules and the surrounding lattice, which is a thermal process, and (2) carrier capture events that deposit energy into defects' localized vibrational modes. As a result, the rate of defect diffusion is a superposition of two terms: a thermally excited term and a recombination-enhanced term. An illustration of the defect energy distribution is shown in Figure 4.2. At thermal equilibrium with only defect-lattice interactions, the distribution is given by $n_{eq}(E)$. When a specified amount of energy E_p is deposited into localized vibrational modes via carrier capture, the local energy distribution is perturbed and evolves toward a new equilibrium, given by a function proportional to $R * n_{eq}(E - E_p)$, where R is the carrier capture rate. During the process of energy deposition and redistribution, two distinct coordinates are involved: the carrier capture coordinate and the defect diffusion reaction coordinate. Carrier capture occurs along the capture coordinate, after which a portion of the excess energy is transferred to the defect diffusion coordinate. Since this energy transfer is significantly faster than energy dissipation through the lattice, the defect complex can be considered effectively isolated

from its surroundings. As a result, a new local equilibrium can be established within the defect system. Using Rice-Ramsperger-Kassel theory, the total defect diffusion rate, K_{total}, is derived as:

$$K_{total} = K_{\neq} exp(-\frac{E^*}{kT}) + \eta R exp(-\frac{E^* - E_p}{kT}) \tag{4.1}$$

where $K_{\neq}$ is the rate of equilibration within the defect molecule and η is the efficiency of energy transfer from carrier capture to defect motion. The first term represents the thermally activated process, while the second term represents the process enhanced by carrier capture.

Later, based on experimental observations of the temperature, stress, and external irradiation dependence of dislocation glide velocity, Maeda et al. proposed an empirical formula for dislocation velocity, as follows [103][104]:

$$V = V_t(\frac{\tau}{\tau_0})^m \, exp(-\frac{E^*}{kT}) \; + V_e(\frac{\tau}{\tau_0})^m(\frac{I}{I_0})^\gamma \, exp(-\frac{E^* - E_p}{kT}) \tag{4.2}$$

where τ is the stress, I is the external irradiation intensity, T is the bulk temperature. The parameters γ and m are empirical constants, with $\gamma \approx 1$ and $m \approx 1 \sim 2$. The role of external irradiation is primarily to generate free carriers that mobilize defects via the REDG mechanism. Note that the values of m depends on the dislocation type (α, β, screw) and doping type (n-type or p-type) in GaAs; it typically falls within the range of 1 to 2 [165][166]. A comparison of Equation 4.1 and Equation 4.2 reveals a clear similarity between the two expressions, suggesting that same recombination-enhanced kinetics is operating in both point defect diffusion and dislocation glide [103].

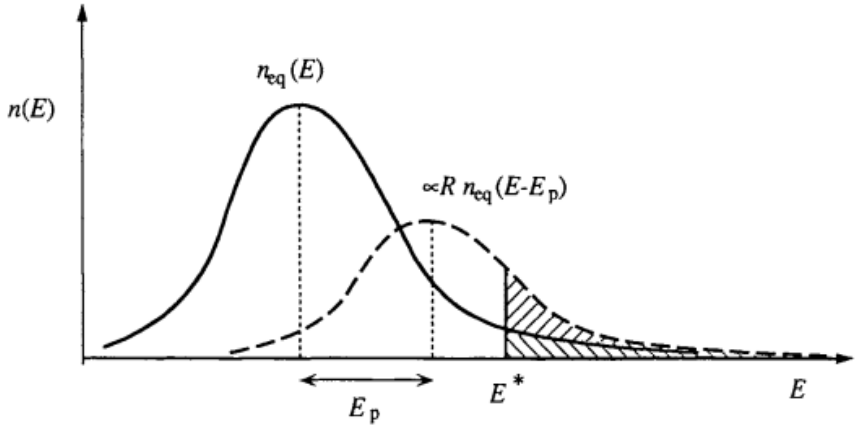


Figure 4.2: The number distribution functions $n(E)$ of defect molecules possessing vibration energy between E and $E + dE$ [104].

4.1.2 Thermal Stress Mechanism

In addition to the widely accepted phonon-kick mechanism, Schwartz proposed another mechanism, suggesting that thermal stress generated by non-radiative recombination at DLDs can also enhance the dislocation glide process [167]. Schwartz observed that the DLD growth velocity is proportional to $I^{1.8}$ under optical irradiation, where I is the irradiation intensity. According to Equation 4.2, where $\gamma = 1$, and Equation 4.1, where the recombination rate R is proportional to I, one would expect the DLD growth velocity to scale linearly with I. To explain the experimentally observed exponent of 1.8, Schwartz points out that the DLD propagation velocity is also proportional to τ^m, where m falls between 1 and 2. He further suggested that this stress τ can be thermal stress induced by local heating at the DLD site, and the local heating is caused by capture of carriers excited the optical irradiation. So that

$$V \sim \tau^m \sim \Delta T^m \sim I^m \tag{4.3}$$

Schwartz's results suggest that the phonon-kick mechanism is not the sole contributor to DLD growth; the thermal stress mechanism they proposed also plays a significant role in augmenting DLD propagation.

4.2 Longitudinal Spatial Dependence of DLD Growth Velocity in Diode Lasers

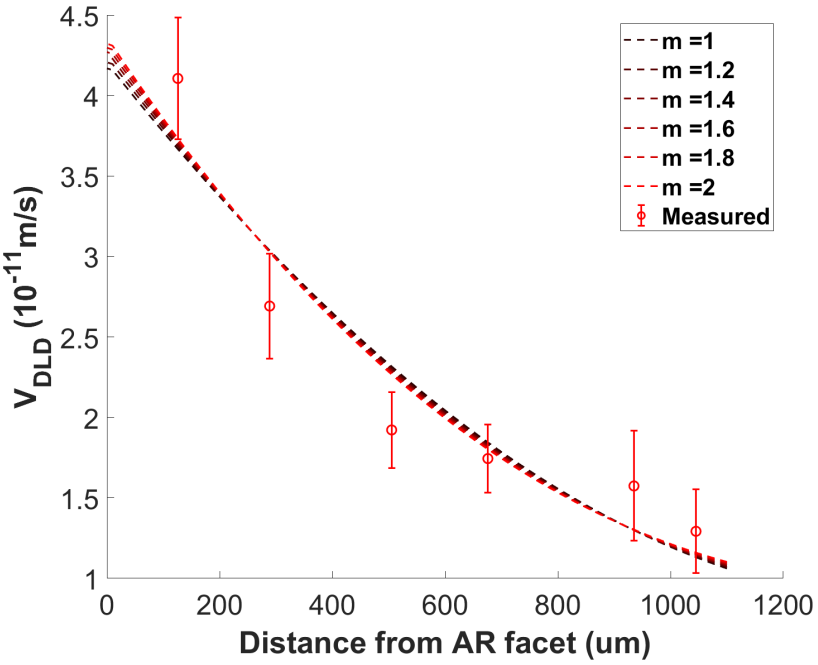
As mentioned in 1.3.2.2, it has been demonstrated that the DLD growth rate in laser diodes is linearly dependent on injected current density in diode laser devices [99][100][101], while defect velocity and growth rate in a bulk material scales with the intensity of external excitation (such as laser beams or electron beams) [102][103][104]. Other key factors affecting DLD propagation rate in bulk materials include temperature and mechanical stress [103][104][102][105][168].

Despite the insights mentioned above, no prior research has investigated the spatial dependence of DLD growth rate in laser diodes. Given that the longitudinal spatial hole burning (LSHB) effect results in non-uniform carrier density, photon density, and injected current along the laser cavity [169][170][171][172], investigating the spatial dependence of DLD growth rate is important, as it captures the non-uniformity in growth rate and helps identify the dominant factors influencing defect motion.

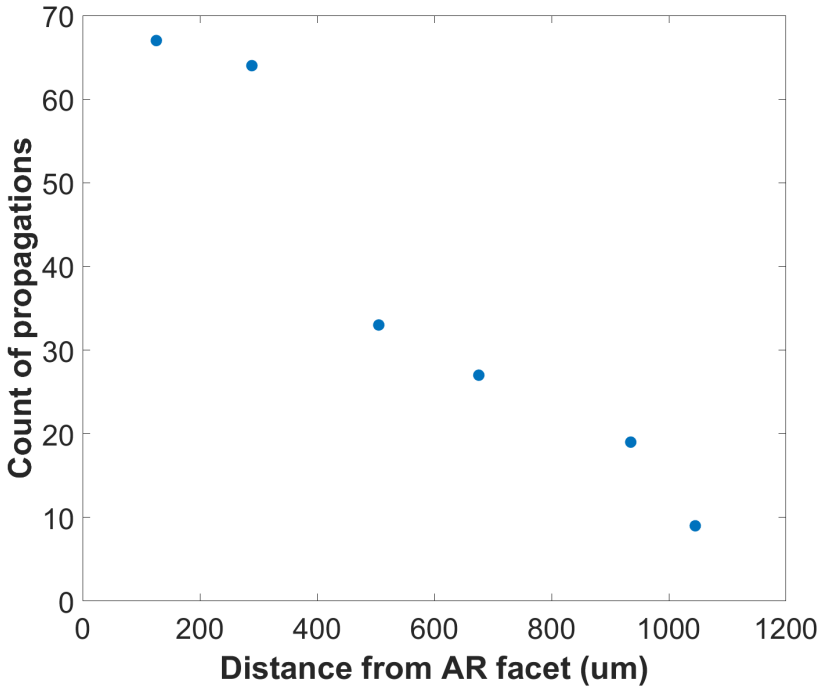
4.2.1 Calculation of DLD Growth Velocity

Four L0 devices (CTNW2, CTNW3, CTNW4, CTNW11) were analyzed here, as they were aged under the same conditions and have the same device parameters. The time-resolved defect distribution images are shown in chapter 3. The transformation from DSDs to DLDs follows a sequential process, as described in previous studies: a tiny dark spot first expands, increasing in radius, and then it propagates along the ⟨110⟩ direction [102][12]. In this study, we focus on the DLD propagation along the ⟨110⟩ direction. The DLD growth rate is calculated by dividing the total propagation length during an aging step by the number of hours in that step (e.g., 50 or 100 hours). Note that when multiple DLDs (or DSDs) are present in a device, a specific DLD may or may not propagate after an aging step. Therefore, each instance of DLD propagation during an aging step is considered an independent defect motion activity, and the longitudinal position of its starting point is recorded.

The DLD growth rate was calculated for all observable DLDs across the four devices. The growth rate for each propagation event was determined following every aging step. To analyze the longitudinal dependence of DLD behavior, the average growth rate was evaluated as a function of position, using 200 μm segments along the cavity length. The results are shown in Figure 4.3a, where error bars represent two standard errors. In parallel, the number of DLD propagation events was counted within each segment and is shown in Figure 4.3b. The DLD growth rate clearly decreases as the distance from the anti-reflective (AR) facet increases. Similarly, the number of DLD propagation events also declines with distance from the AR facet, and no dark line propagation was observed beyond 1200 μm. In our devices with a 1500 μm cavity length, the DLD growth rate at a distance of ~100 μm the AR facet is approximately three times higher than at a distance of ~1100 μm from the AR facet.



(a)



(b)

Figure 4.3: a) Average DLD growth rate (measured) for segments along the cavity vs. distance from the AR facet (segment length = 200 μm) and non-linear regression fitted DLD growth rate for different m values. b) Number of dark line defect propagation observed for segments along the cavity vs. distance from the AR facet (segment length = 200 μm)

4.2.2 Longitudinal Spatial Hole Burning Simulation

As mentioned above, the longitudinal spatial hole burning (LSHB) effect motivates the investigation of the longitudinal dependence of DLD growth velocity. To explore the underlying mechanisms responsible for this position-dependent behavior, our collaborators at LLNL simulated the photon and carrier density profiles under constant voltage boundary conditions and an isothermal cavity assumption, as shown in Figure 4.4. The simulation approach is very similar to the methodology reported in [171], and the resulting carrier density profile is consistent with experimental measurements for similar devices [173].

For better understanding of the LSHB effect, basic governing equations and boundary conditions used for the simulation are introduced below:

$$\begin{aligned} \frac{dS^+(z)}{dz} &= (\Gamma g(z) - \alpha_i) S^+(z) \\ \frac{dS^-(z)}{dz} &= -(\Gamma g(z) - \alpha_i) S^-(z) \end{aligned} \tag{4.4}$$

Boundary conditions:

$$\begin{aligned} \frac{S^+(0)}{S^-(0)} &= R_{AR} \\ \frac{S^-(L)}{S^+(L)} &= R_{HR} \end{aligned} \tag{4.5}$$

where S^+ represents photons propagating towards the HR facet, S^- represents photons propagating towards the AR facet, z represents distance from the AR facet, Γ represents the optical mode confinement factor, $g(z)$ represents the gain, α_i represents the intrinsic optical loss, and L represents the cavity length. Note that the gain $g(z)$ is non-uniform and dependent on the distance from the AR facet, due to the coupling between carrier density and photon density in the rate equations.

According to the results of LSHB effect simulation, carrier densities in the quantum well and waveguide decrease toward the AR facet, which is known to contribute to the DLD growth rate. As illustrated in Figure 4.4, the waveguide carrier density decreases toward the AR facet, whereas the total photon density increases in that direction. The relative variation of the simulated carrier density in the quantum well closely mirrors that in the waveguide. These results suggest that DLD growth in diode laser cavities is directly enhanced by photon absorption.

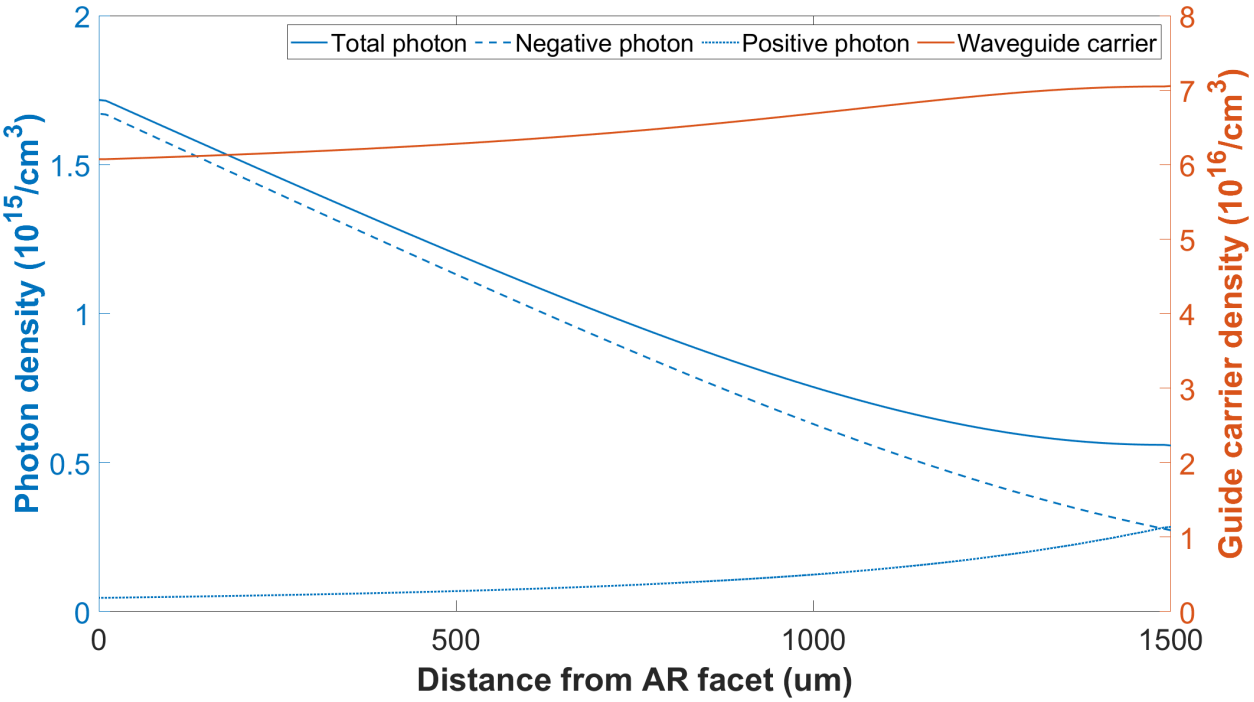


Figure 4.4: Simulation results of photon density and waveguide carrier density along the longitudinal direction. Negative photon density (S^-) represents light propagating toward the AR facet, while positive photon density (S^+) represents light propagating toward the HR facet. The total photon density is the sum of both components. Note that the relative variation of simulated carrier density in the quantum well is very similar to that in the waveguide.

4.2.3 Asymmetric DLD Propagation

Asymmetries observed in DLD growth provide further evidence supporting the role of direct photon absorption in enhancing the defect propagation process. Device CTNW2 (Figure 3.6) illustrates this phenomenon: the edge of the DLD closer to the AR facet remains largely stationary, while the edge closer to the HR facet exhibits significant propagation, which is an asymmetric growth of DLD towards the HR facet. This phenomenon is more prominent when the DLD is closer to the AR facet. This behavior is illustrated in Figure 4.5 and can be explained by the following reasons:

1. The ratio of photon flux propagating towards the AR facet (S^-) to the flux propagating towards the HR facet (S^+) increases as position approaches the AR facet due to LSHB, with the ratio approaching a value of the inverse facet reflectivity [169][170][171][172][173].

2. Optical absorption within the DLD inhibits the large number of photons incident on the DLD that are propagating toward the AR facet (S^-) from interacting with the DLD edge closer to the AR facet. As a result, propagation of this edge can only be triggered by the relatively smaller population of incident photons traveling toward the HR facet (S^+). Conversely, the

DLD edge closer to the HR facet is primarily influenced by the large population of photons traveling toward the AR facet (S^-).

3. As a result of (1) and (2), the DLD edge closer to the HR facet is exposed to a higher photon flux compared to the edge closer to the AR facet. Consequently, the DLD is more likely to propagate toward the HR facet. This asymmetry becomes more pronounced at positions closer to the AR facet, where the ratio of S^- to S^+ is significantly larger.

Taking device CTNW2 at 50 hours as an example, the rear- and front-facing edges of the DSD in Figure 3.6 are located at 289 μm and 298 μm from the AR facet, respectively. At these positions, our LSHB simulations indicate that the S^- photon flux at the rear-facing edge is 23.6 times greater than the S^+ photon flux at the front-facing edge.

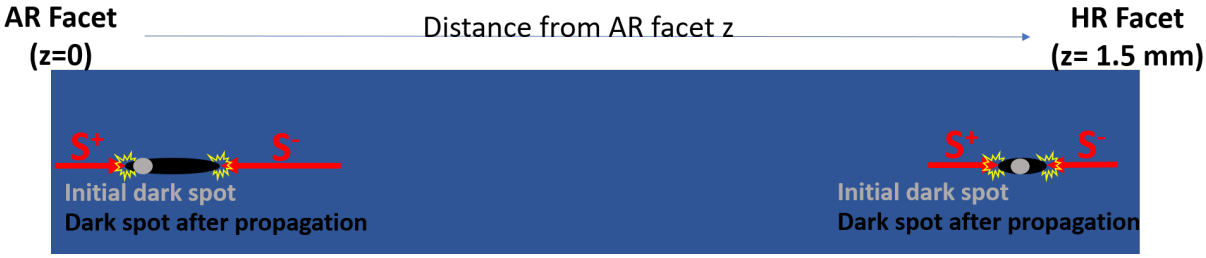


Figure 4.5: Illustration of asymmetric dark line defect (DLD) propagation driven by a large S^- to S^+ ratio closer to the AR facet. The initial dark spots are represented by grey spots, while the dark spot after propagation are shown as a black spots.

4.2.4 Photon-accelerated REDG

The strong photon density dependence observed here does not necessarily imply that carrier capture plays no role in DLD growth. Rather, defect photo-ionization can augment or accelerate a carrier capture-based REDG process as illustrated by the following argument. In classic REDG model, defect growth involves phonon kicks generated by a process in which a defect D cycles between an ionized (D^+) and neutral (D^0) state due to carrier capture of electrons (e^-) and holes (h^+), as illustrated by reactions in Equation 4.4:

$$D^+ + e^- \rightarrow D^0, \qquad D^0 + h^+ \rightarrow D^+ \qquad (classic\ REDG) \tag{4.6}$$

In this case, based on Equation 4.1, the defect growth rate is proportional to the following term:

$$V \sim R\eta\, exp(-\frac{E^* - E_{phonon-kick}}{kT}) \tag{4.7}$$

where the carrier capture rate R is the combined rate of reactions described in Equation 4.6, which can be expressed in the following form:

$$R = \frac{1}{1/R_n + 1/R_p} \tag{4.8}$$

$$R_{n,p} = s_{n,p} v_{n,p} N_{n,p} \tag{4.9}$$

where $s_{n,p}$ denotes the carrier capture cross-section for electrons and holes, respectively; $v_{n,p}$ is the corresponding carrier thermal velocity, and $N_{n,p}$ is the carrier density. Among the two carrier capture processes described in Equation 4.6, one is typically much smaller than the other. As a result, the combined rate R is determined by the slower rate.

The exponential term in Equation 4.7 accounts for the reduction of the activation energy for defect motion, E^*, due to the phonon-kick mechanism, as discussed in 4.1.1 [15][88][104]. The value of $E_{phonon-kick}$ corresponds to the energy deposited into localized vibrational modes and is taken to be the greater of the values associated with electron and hole capture events.

In a simple photon-accelerated model proposed here, the presence of a large photon density $S \sim 10^{15} cm^{-3}$ in the diode laser cavity, combined with a typical photon absorption cross section $s_{opt} \sim 10^{-16} cm^2$ [174][175], results in a defect photon-ionization rate (Equation 4.10) that can significantly exceed the slower carrier capture rate that determines R ($R_{photon} \gg R$).

$$R_{photon} = s_{opt} \frac{c}{n_r} S \tag{4.10}$$

where c/n_r represents the group velocity of photons in the cavity. As a result, the slower carrier capture process is replaced by the photo-ionization process, thereby accelerating the REDG reaction via photon ($h\nu$) absorption. Assuming that hole capture is the slower of the two carrier capture processes, the corresponding photon-accelerated REDG reactions are:

$$D^+ + e^- \rightarrow D^0, \qquad D^0 + h\nu + \rightarrow D^+ + e^- \qquad (photon - accelerated) \tag{4.11}$$

With the slower carrier capture process replaced by the photo-ionization mechanism, the defect growth rate is expected to increase by at least a factor of R_{photon}/R. The photon-accelerated process (Equation 4.11) would involve a similar reduction in activation energy $E_{phonon-kick}$ as in the classic REDG process (Equation 4.6), if the faster carrier capture process results in a larger phonon-kick that couples more efficiently to the localized vibrational modes responsible for defect motion. It is also possible that the photo-ionization process results in a larger phonon kick energy $E_{phonon-kick}$. For example, in the case of defects in a waveguide layer with a band gap E_g much larger than the lasing photon energy, the classic REDG process will provide an energy $E_{phonon-kick}$ smaller than

E_g. However, photo-ionization could excite carriers into higher-order conduction band valleys, thereby increasing $E_{phonon-kick}$. This qualitative analysis illustrates that photo-ionization has the potential to significantly enhance defect growth rates.

4.2.5 Non-linear Regression Fit

Using the values of the photon density (S) and waveguide carrier density (n_{guide}) from the LSHB simulation mentioned above, a non-linear regression analysis was performed to quantify the relative contribution of photon absorption to the DLD growth rate.

First, the form of the fitting equation was determined. According to the REDG velocity equation, the DLD growth velocity can be expressed as:

$$V \sim R\tau^m \, exp(-\frac{E^* - E_p}{kT}) \tag{4.12}$$

where the exponent m ranges between 1 and 2 [165][166], as discussed in 4.1.1. The carrier or photon capture rate R is proportional to carrier or photon density, and can therefore be expressed as:

$$R \sim C_1 S + C_2 n_{guide} \tag{4.13}$$

As introduced in 4.1.2, Schwartz pointed out that a local temperature rise can increase thermal stress, thereby facilitating DLD propagation [167]. The thermal stress τ, which may arise from either carrier capture or optical absorption, can be approximated as:

$$\tau \sim \Delta T \sim C_3 S + C_4 n_{guide} \tag{4.14}$$

where C_1, C_2, C_3, C_4 are fitting coefficients to be determined. To quantify the respective contributions of photon density and waveguide carrier density to the DLD growth rate, a nonlinear regression fit was performed using the following expression:

$$V_{DLD} \sim (C_1 S + C_2 n_{guide})(C_3 S + C_4 n_{guide})^m \tag{4.15}$$

In this equation, the first term represents the recombination rate, while the second term accounts for thermal stress. All fitting coefficients are constrained to be non-negative. The fitting results for various values of m are shown in Figure 4.3a. Since the cross terms in Equation 4.15 involve both the photon density S and the waveguide carrier density n_{guide}, we use the ratio

$$\frac{C_1 S(C_3 S + C_4 n_{guide})^m}{V_{DLD}} \tag{4.16}$$

to quantify the relative contribution of photon density to DLD growth. As shown in Figure 4.3a, the fitting results are not sensitive to the choice of m; however, increasing m tends to reduce the photon contribution ratio. Nevertheless, as illustrated in Figure 4.6, even when m equals 2, the photon contribution remains as high as 67% at the AR facet and approximately 50% at 1000 μm from the AR facet. These results strongly suggest that photon density plays a significant role in enhancing DLD growth.

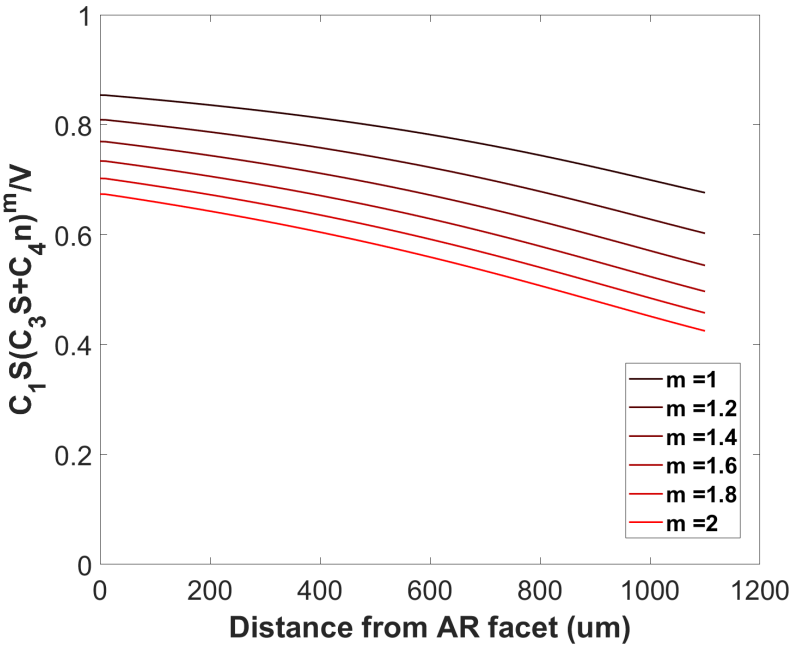


Figure 4.6: Ratio of the photon-assisted component to the total DLD growth velocity.

CHAPTER 5

Summary and Future Work

5.1 Summary

Diode lasers, one of the most significant scientific advancements of the past six decades, offer not only the high power density, excellent beam quality, and spectral coherence characteristic of their counterparts, such as gas, dye, and solid-state lasers, but also deliver exceptionally high energy conversion efficiency and compactness. Despite these advantages, the degradation of diode lasers has remained a persistent challenge since their inception, limiting their reliability, maximum output power, efficiency, and operational lifetime. In this work, non-destructive defect characterization techniques were employed to investigate the degradation process by monitoring the formation and evolution of defects on both the facets and cavities of diode lasers throughout their operational lifetimes. CCD-based thermoreflectance microscopy was employed to image 2D temperature profiles of the front facets, enabling the tracking of defect formation and evolution at the facet. In addition, a NIR defect imaging technique was developed and applied to visualize defect dynamics within the device cavities over time. Through these cavity defect images, a longitudinal spatial dependence of dark line defect (DLD) growth velocity was observed. Based on this observation, a photon-assisted mechanism is proposed as a primary driver of the enhanced DLD propagation.

By thermally profiling the front facet of a device throughout its lifetime, we observed a gradual increase in overall facet temperature, accompanied by the formation of several localized hot spots. Notably, two concentrated hot spots emerged immediately before and after laser failure, which corresponded to regions that ceased emitting after failure. However, no visible morphological changes were detected at these locations, even under SEM. Based on these findings, we conclude that point defect clusters gradually form on the facet, leading to localized heating, which in turn facilitates the creation of additional defects. When local temperature or defect density reaches a threshold, catastrophic optical damage (COD) is triggered. However, the critical defects responsible for device failure are either too small to be resolved on the facet or are located within the cavity near the front facet. In either case, the hot spots associated with these defects can be effectively

traced using the thermoreflectance technique.

For defect characterization within laser cavities, a near-infrared (NIR) defect imaging technique was developed, utilizing NIR emission originating from the waveguide core layer of the device. An intensity gradient along the cavity and above-threshold intensity clamping were observed in this NIR emission, suggesting it is associated with spontaneous emission from deep-level states in the quantum well and waveguide core layers. NIR intensity maps of multiple devices were imaged. In some cases, dark-line propagation was observed alongside a corresponding decline in optical power and a redshift in lasing wavelength. The results demonstrate that a greater number of dark lines, or a longer propagation length, correlates with more rapid degradation, confirming that the dark lines visible in the NIR images represent defects responsible for laser degradation. This NIR emission serves as an effective defect imaging signal because the associated defects lead to enhanced non-radiative recombination, affecting both interband transitions (fundamental laser emission) and deep-level transitions (NIR emission). Furthermore, the long wavelength of this NIR light allows it to transmit through the thick GaAs substrate without significant absorption, enabling non-destructive, through-substrate imaging of cavity defects.

Cavity defect imaging results from devices with varying artificial oxygen doping concentrations suggest that gradual degradation is suppressed in oxygen-doped devices. This finding contrasts with earlier notions that oxygen incorporation negatively impacts the reliability of diode lasers [160][161][162]. Our observation aligns with conclusions drawn from a complementary set of diagnostics presented in Ref. [142], which provides a detailed explanation of this behavior. Specifically, it was proposed that interstitial oxygen atoms preferentially combine with phosphorus vacancies, thereby reducing the density of these vacancies and non-radiative recombination associated with them [142].

Facet temperature profiles of several devices were simultaneously acquired during cavity defect imaging tests. The results indicate that dark lines propagating from the facet into the cavity are typically accompanied by corresponding hot spots on the facet. However, not all facet hot spots could be directly linked to dark-line defects (DLDs) within the cavity. These findings suggest that while some facet heating is caused by cavity defects, other hot spots are associated with the formation of point defect clusters on the facet. Importantly, the propagation of DLDs within the cavity, compared to facet absorption, plays a dominant role in the gradual degradation of diode lasers. Furthermore, it was observed that facet failure (COMD) results in a significant cooling of the entire facet. In contrast, cavity failure (COBD) does not produce a comparable cooling effect on the facet.

Using the NIR defect imaging technique, a longitudinal spatial dependence of dark-line defect (DLD) growth velocity was observed. This spatial variation, together with the known non-uniform distribution of photon and carrier densities along the cavity introduced by the LSHB effect, led to

the proposal of a photon-accelerated mechanism that enhances DLD propagation. In the widely accepted phonon-kick mechanism, the electron or hole capture rate often serves as the rate-limiting step in defect growth. By contrast, in the proposed photon-accelerated mechanism, the slower carrier capture process may be replaced by a faster photon absorption process, thereby enabling a faster defect growth rate.

In summary, this dissertation presents new observations and insights into the degradation of diode lasers. A broadband near-infrared (NIR) emission originating from the active region of the laser was demonstrated to be effective for imaging dark line defects (DLDs) in the cavity. While cavity DLDs have traditionally been associated with rapid degradation and COD, this work identifies them as the primary contributor to gradual degradation as well. Contrary to conventional expectations, oxygen doping was found to suppress gradual degradation. Furthermore, photon absorption was shown to play a significant role in driving DLD propagation, challenging the prevailing view that attributes defect motion primarily to carrier capture.

5.2 Future Work

There are several directions in which this work can extend in the future.

5.2.1 Nature of DLDs that lead to COMD

In Chapter 2 and Chapter 3, several devices that experienced catastrophic optical mirror damage (COMD) were discussed. Among them, morphological changes on the front facet were observed in only one device, despite cavity NIR imaging showing that all DLDs formed during COMD originated from the front facet. This implies that the initiation points of these DLDs were located no more than 1 μm from the facet surface. This raises important questions: Where exactly is the initiation point located? How far is it from the facet surface? And why did it not result in a molten or visibly damaged region on the facet at such a short distance?

To address these open questions, high-resolution techniques such as transmission electron microscopy (TEM) may be employed to directly investigate the subsurface structure near the facet. However, such analysis would require substrate removal from the device under test, a process that may introduce new defects and potentially alter the native defect landscape, complicating the interpretation of the results.

5.2.2 Expanding the NIR Defect Imaging Technique to Devices at Various Wavelengths

While the NIR defect imaging technique developed in this dissertation has proven effective for characterizing DLD formation and evolution in high-power diode lasers operating near 800 nm, its applicability to devices at other emission wavelengths remains an important direction for future research. Extending this technique to lasers operating in various wavelength ranges would provide a more universally applicable diagnostic tool for non-destructive, in situ reliability assessment of a wide range of photonic devices. As a result can enable broader insight into defect dynamics across diverse material systems and device structures.

5.2.3 Mitigation of the Photon-accelerated REDG Process

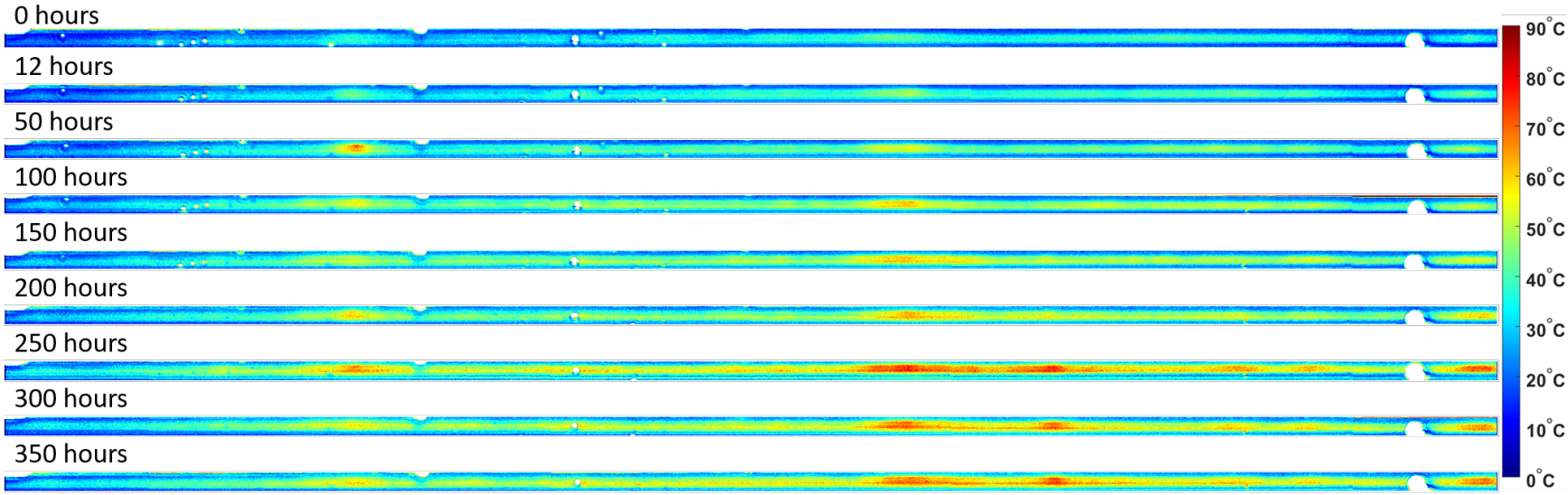
As discussed in Chapter 4, the dark line defect (DLD) propagation process can be significantly accelerated by photon absorption. Future efforts may focus on strategies to mitigate this effect and thereby enhance device reliability. One potential direction involves eliminating or reducing the density of initial dark spot defects observed in fresh devices. This requires a detailed investigation into the origins of these pre-existing defects, particularly by evaluating how different manufacturing steps, such as epitaxial growth and wafer bonding, contribute to their formation.

Another promising approach is to address the longitudinal spatial hole burning (LSHB) effect, which gives rise to a non-uniform photon density profile along the cavity. Mitigating this non-uniformity could reduce the asymmetry in DLD propagation and minimize localized acceleration of defect growth. Potential methods include cavity design optimization, reduction of the reflectivity difference between AR and HR facets, or reduction of cavity length to achieve more uniform photon distribution.

APPENDIX A

Thermal Profiles

A.1 Thermal Profiles of CTNW2



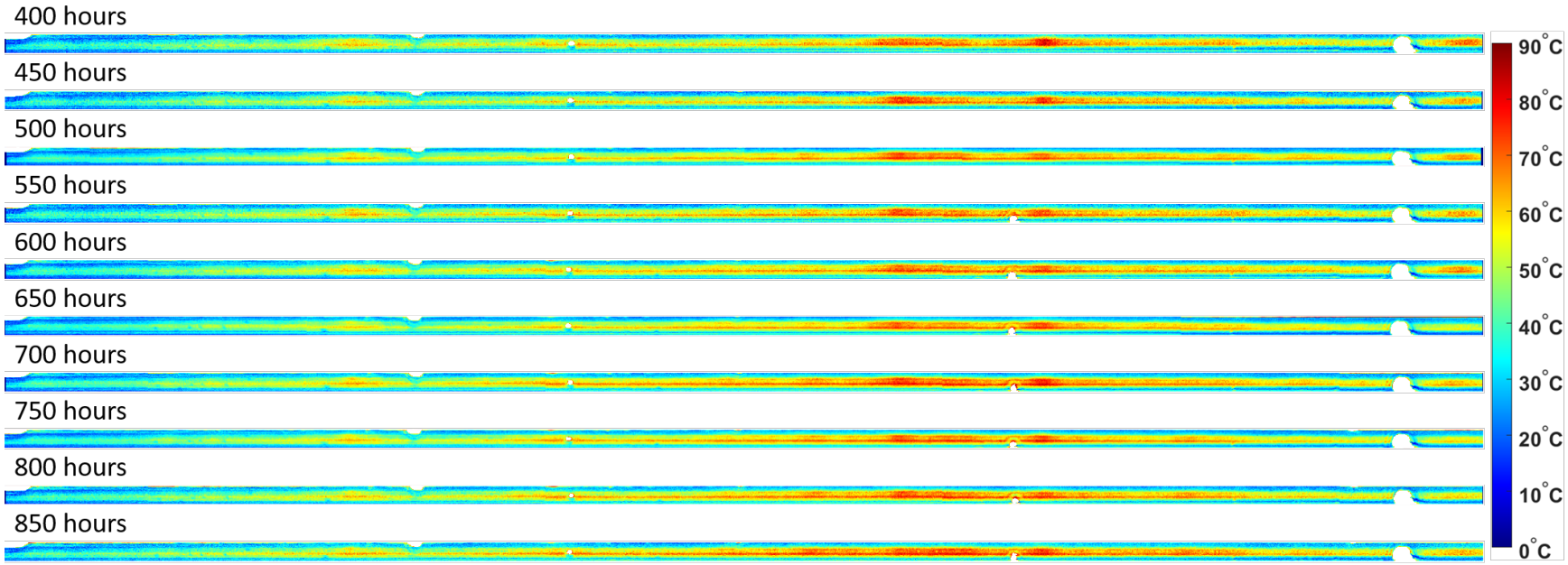


Figure A.1: Thermal maps of device CTNW2 at 4 A from 0 to 850 hours.

A.2 Thermal Profiles of CTNW3

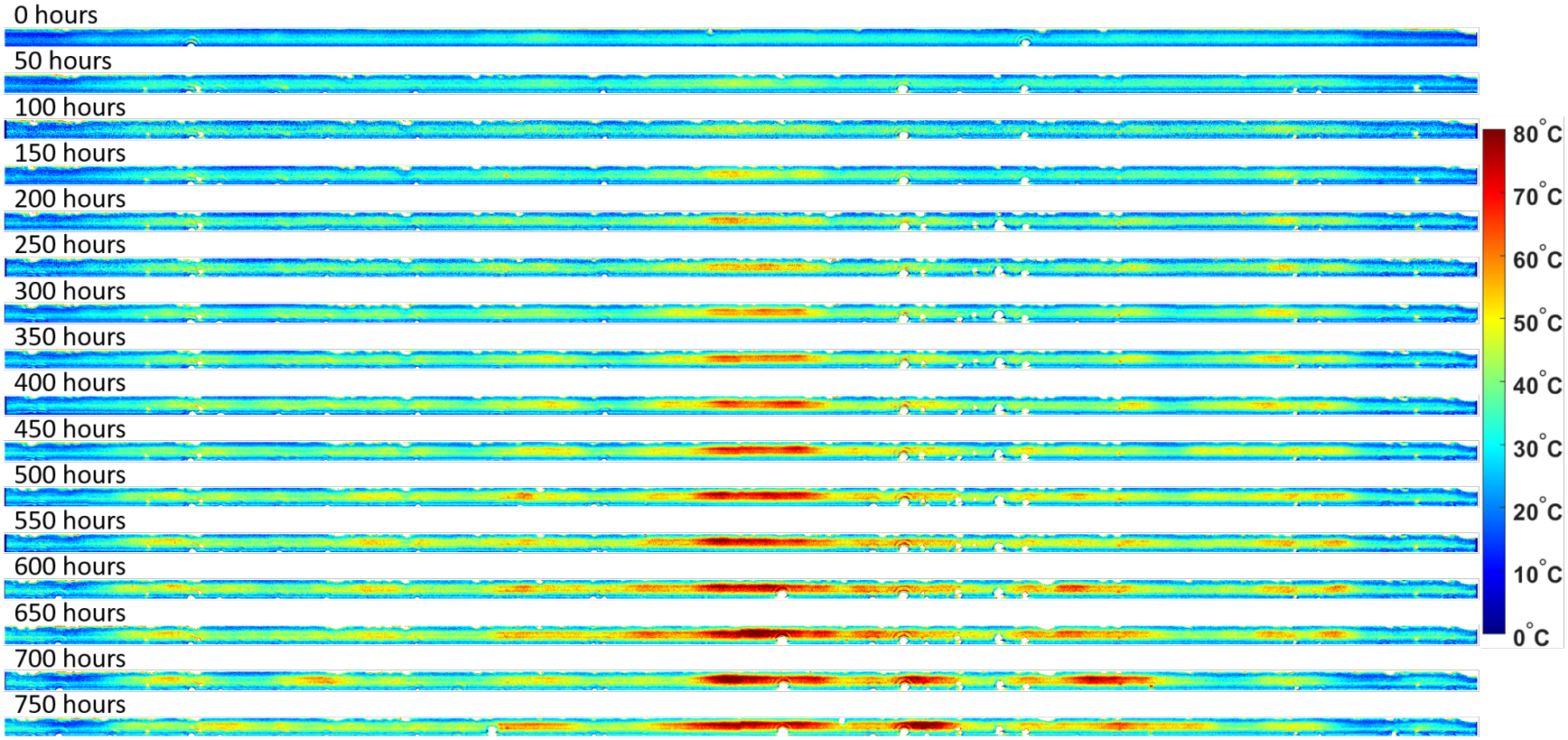


Figure A.2: Thermal maps of device CTNW3 at 4 A from 0 to 750 hours.

A.3 Thermal Profiles of CTNW10

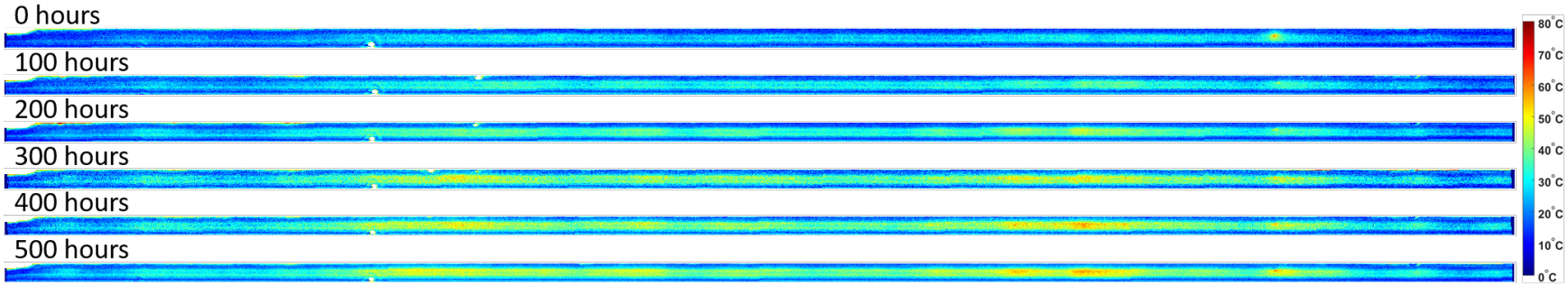


Figure A.3: Thermal maps of device CTNW10 at 4 A from 0 to 500 hours.

A.4 Thermal Profiles of CTNW11

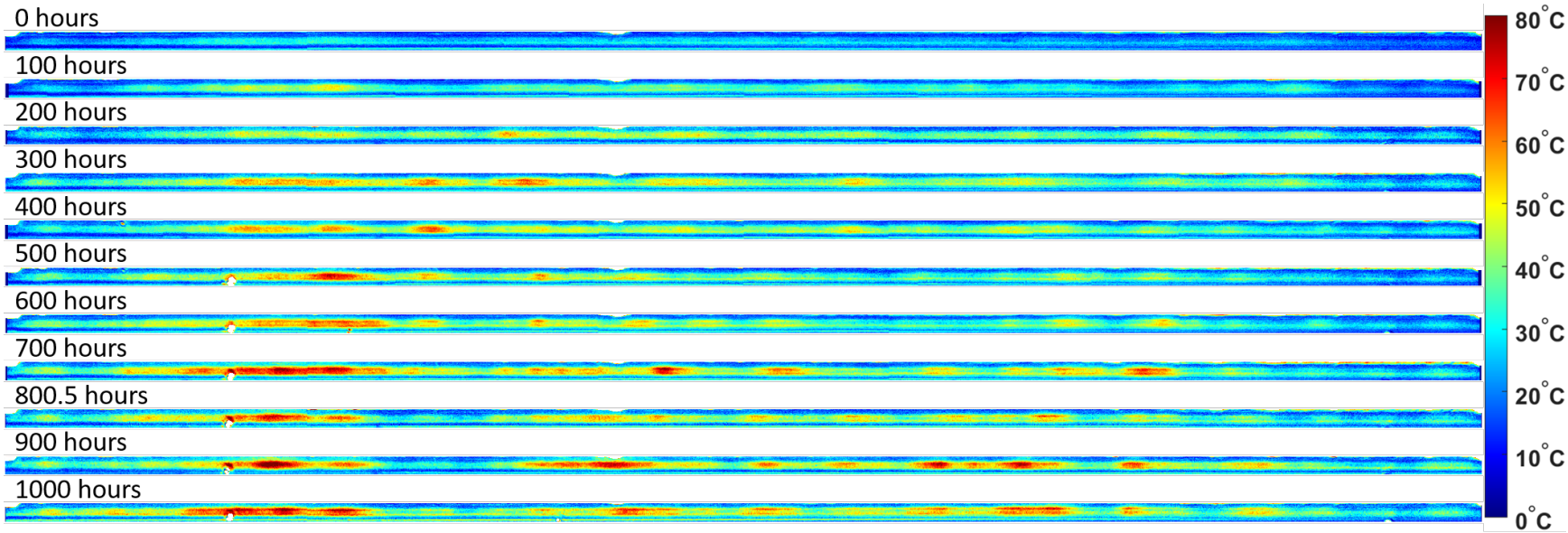


Figure A.4: Thermal maps of device CTNW11 at 4 A from 0 to 1000 hours.

A.5 Thermal Profiles of T120TA

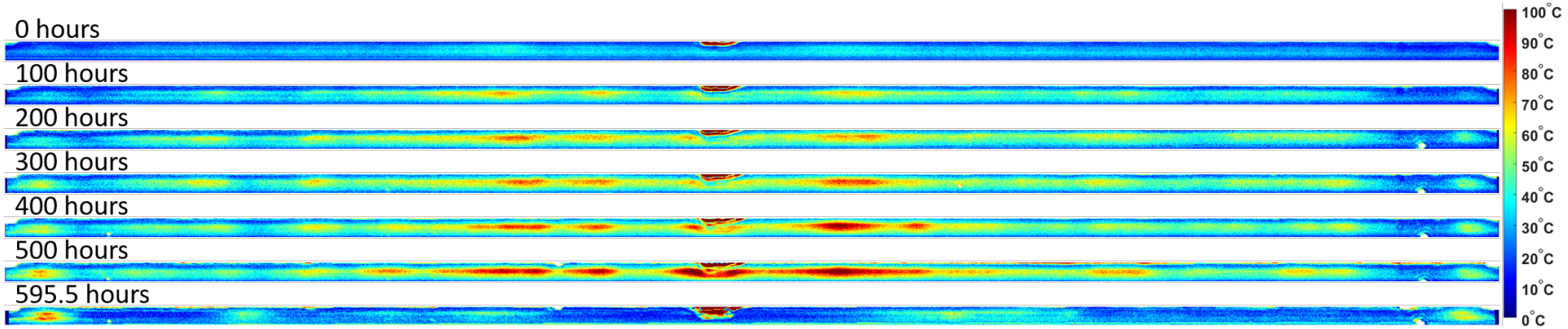
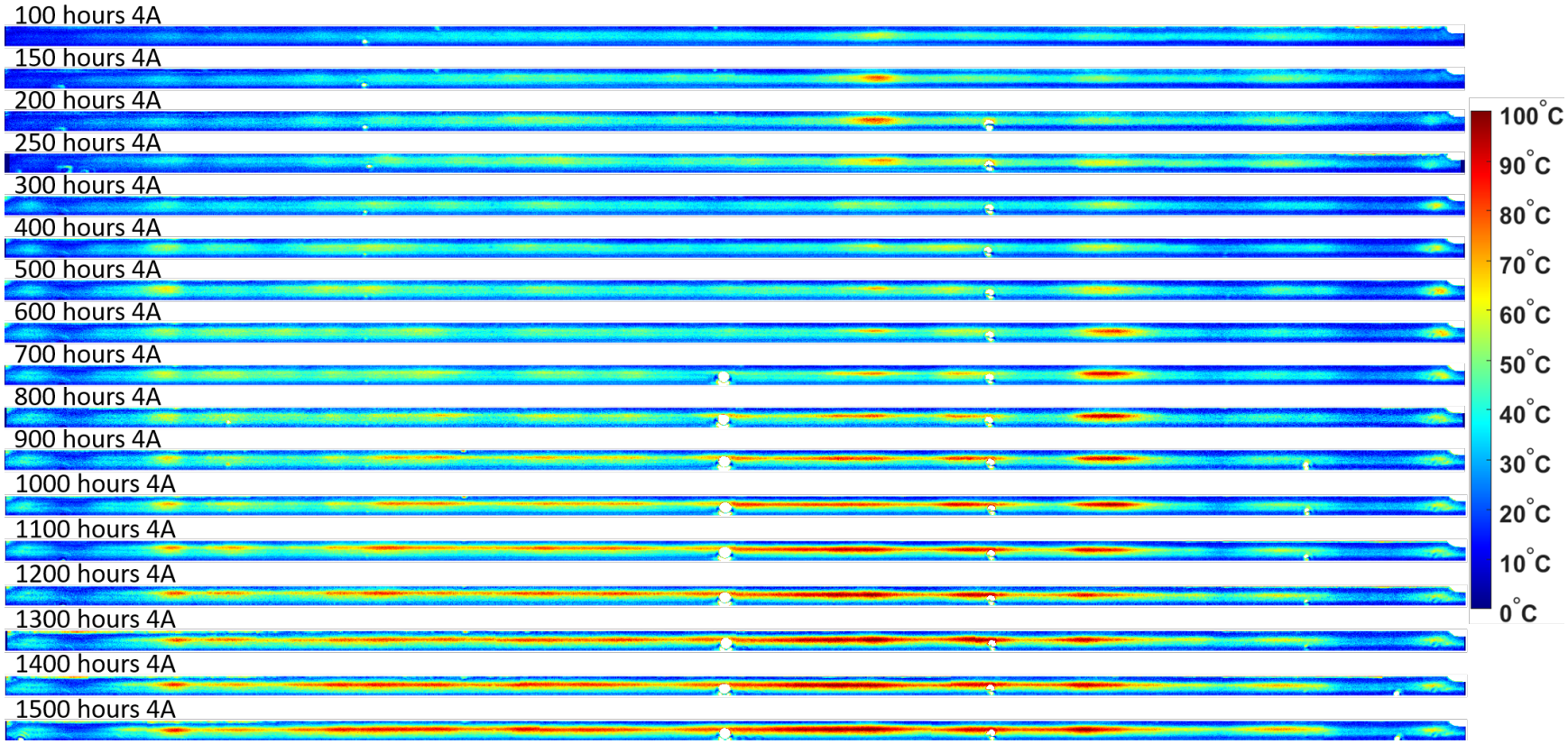


Figure A.5: Thermal maps of device T120TA at 4 A from 0 to 595.5 hours.

A.6 Thermal Profiles of T120Z9



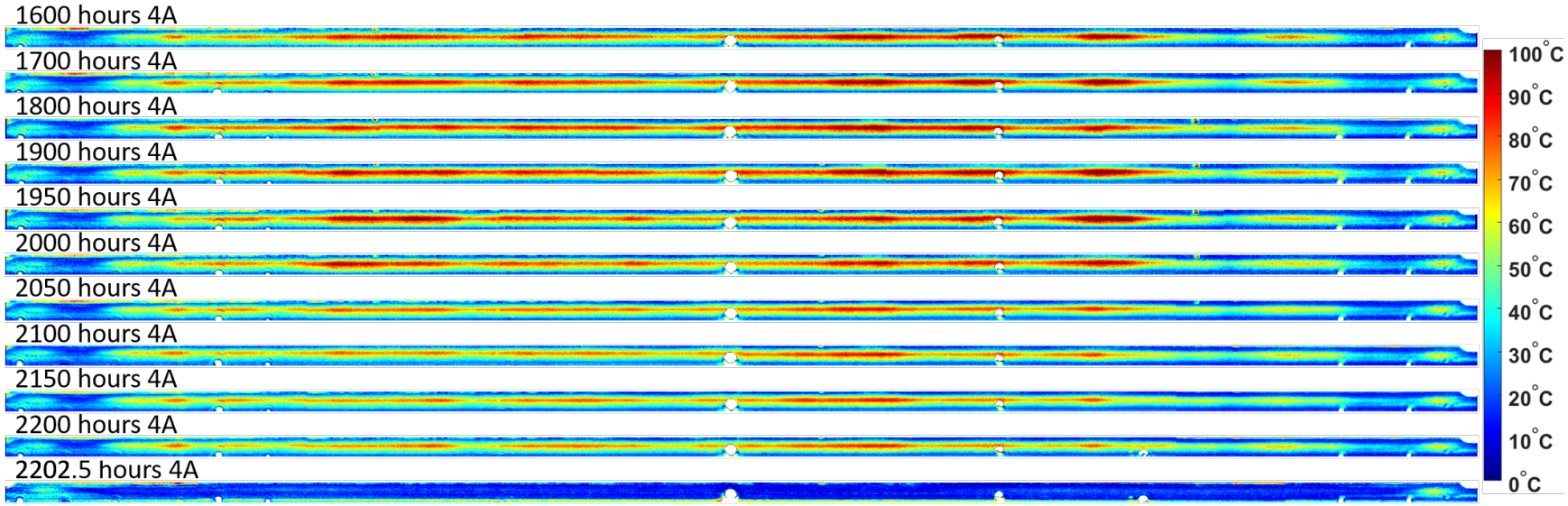


Figure A.6: Thermal maps of device T120Z9 at 4 A from 0 to 2202.5 hours.

Bibliography

[1] R. N. Hall, G. E. Fenner, J. Kingsley, T. Soltys, and R. Carlson, "Coherent light emission from gaas junctions," *Physical Review Letters*, vol. 9, no. 9, p. 366, 1962.

[2] M. I. Nathan, W. P. Dumke, G. Burns, F. H. Dill, and G. Lasher, "Stimulated emission of radiation from gaas p-n junctions," *Applied Physics Letters*, vol. 1, no. 3, pp. 62–64, 1962.

[3] P. W. Epperlein, *Semiconductor laser engineering, reliability and diagnostics: a practical approach to high power and single mode devices*. John Wiley & Sons, 2013.

[4] A. Yariv, *Quantum Electronics*. John Wiley & Sons, 1989.

[5] P. Bhattacharya, *Semiconductor optoelectronic devices*. Prentice-Hall, Inc., 1997.

[6] N. Wiedmann, J. Jandeleit, D. Hoffmann, P. Loosen, and R. Poprawe, "Defects and degradation of inga (al) as/gaas high-power diode lasers," in *Advanced High-Power Lasers*, SPIE, vol. 3889, 2000, pp. 90–95.

[7] D. Pierścińska, "Thermoreflectance spectroscopy—analysis of thermal processes in semiconductor lasers," *Journal of Physics D: Applied Physics*, vol. 51, no. 1, p. 013 001, 2017.

[8] B. Monemar, "Degradation processes in semiconductor lasers," *Physica Scripta*, vol. 24, no. 2, p. 367, 1981.

[9] B. De Loach, B. Hakki, R. Hartman, and L. D'asaro, "Degradation of cw gaas double-heterojunction lasers at 300 k," *Proceedings of the IEEE*, vol. 61, no. 7, pp. 1042–1044, 1973.

[10] P. Petroff and R. Hartman, "Defect structure introduced during operation of heterojunction gaas lasers," *Applied Physics Letters*, vol. 23, no. 8, pp. 469–471, 1973.

[11] T. Kamejima, K. Ishida, and J. Matsui, "Injection-enhanced dislocation glide under uniaxial stress in gaas–(gaal) as double heterostructure laser," *Japanese Journal of Applied Physics*, vol. 16, no. 2, p. 233, 1977.

[12] M. Fukuda, "Reliability and degradation of semiconductor lasers and leds," *Artech House*, pp. 325–333, 1991.

[13] M. Fukuda and G. Mura, "Laser diode reliability," in *Advanced Laser Diode Reliability*, Elsevier, 2021, pp. 1–49.

[14] J. Jiménez, "Laser diode reliability: Crystal defects and degradation modes," *Comptes Rendus Physique*, vol. 4, no. 6, pp. 663–673, 2003.

[15] L. Kimerling, "Recombination enhanced defect reactions," *Solid-State Electronics*, vol. 21, no. 11-12, pp. 1391–1401, 1978.

[16] V. Hortelano, J. Anaya, J. Souto, J. Jiménez, J. Perinet, and F. Laruelle, "Defect signatures in degraded high power laser diodes," *Microelectronics Reliability*, vol. 53, no. 9-11, pp. 1501–1505, 2013.

[17] K. Endo, S. Matsumoto, H. Kawano, I. Sakuma, and T. Kamejima, "Rapid degradation of ingaasp/inp double heterostructure lasers due to¡ 110¿ dark line defect formation," *Applied Physics Letters*, vol. 40, no. 11, pp. 921–923, 1982.

[18] P. Petroff, "Defects in iii–v compound semiconductors," in *Semiconductors and Semimetals*, vol. 22, Elsevier, 1985, pp. 379–403.

[19] K. Häusler, U. Zeimer, B. Sumpf, G. Erbert, and G. Tränkle, "Degradation model analysis of laser diodes," *Journal of Materials Science: Materials in Electronics*, vol. 19, pp. 160–164, 2008.

[20] J. Jandeleit, N. Wiedmann, P. Loosen, and R. Poprawe, "Reliability and degradation mechanisms of high-power diode lasers," in *Testing, Packaging, Reliability, and Applications of Semiconductor Lasers IV*, SPIE, vol. 3626, 1999, pp. 217–221.

[21] L. Wang, E. McVay, S. H. Baxamusa, *et al.*, "Imaging of dark line defect growth in high-power diode laser cavities using broadband near infrared light emission from the laser cavity," *Applied Physics Letters*, vol. 125, no. 25, 2024.

[22] J. Tomm, A. Bärwolff, A. Jaeger, *et al.*, "Deep level spectroscopy of high-power laser diode arrays," *Journal of applied physics*, vol. 84, no. 3, pp. 1325–1332, 1998.

[23] C. Ropers, T. Q. Tien, C. Lienau, *et al.*, "Observation of deep level defects within the waveguide of red-emitting high-power diode lasers," *Applied physics letters*, vol. 88, no. 13, 2006.

[24] J. W. Tomm, M. Ziegler, M. Oudart, J. Nagle, and J. Jiménez, "Gradual degradation of gaas-based quantum well lasers, creation of defects, and generation of compressive strain," *physica status solidi (a)*, vol. 206, no. 8, pp. 1912–1915, 2009.

[25] O. Ueda, "Reliability and degradation of iii-v optical devices focusing on gradual degradation," in *Materials and Reliability Handbook for Semiconductor Optical and Electron Devices*, Springer, 2012, pp. 87–122.

[26] T. Uji, T. Suzuki, and T. Kamejima, "Deep-level changes in (al, ga) as double-heterostructure lasers degraded during accelerated aging at high temperatures," *Applied Physics Letters*, vol. 36, no. 8, pp. 655–657, 1980.

[27] C. Henry, P. Petroff, R. Logan, and F. Merritt, "Catastrophic damage of al x ga1- x as double-heterostructure laser material," *Journal of applied physics*, vol. 50, no. 5, pp. 3721–3732, 1979.

[28] W. Nakwaski, "Thermal analysis of the catastrophic mirror damage in laser diodes," *Journal of applied physics*, vol. 57, no. 7, pp. 2424–2430, 1985.

[29] P. G. Eliseev, "Optical strength of semiconductor laser materials," *Progress in quantum electronics*, vol. 20, no. 1, pp. 1–82, 1996.

[30] W. Tang, H. Rosen, P. Vettiger, and D. Webb, "Raman microprobe study of the time development of algaas single quantum well laser facet temperature on route to catastrophic breakdown," *Applied physics letters*, vol. 58, no. 6, pp. 557–559, 1991.

[31] M. Ziegler, V. Talalaev, J. W. Tomm, *et al.*, "Surface recombination and facet heating in high-power diode lasers," *Applied Physics Letters*, vol. 92, no. 20, 2008.

[32] W. Tang, H. Rosen, P. Vettiger, and D. Webb, "Evidence for current-density-induced heating of algaas single-quantum-well laser facets," *Applied physics letters*, vol. 59, no. 9, pp. 1005–1007, 1991.

[33] P. Epperlein, "Mapping of local temperatures on mirrors of gaas/algaas laser diodes," in *Inst. Phys. Conf. Ser*, vol. 112, 1990, pp. 633–638.

[34] A. Moser, E.-E. Latta, and D. Webb, "Thermodynamics approach to catastrophic optical mirror damage of algaas single quantum well lasers," *Applied physics letters*, vol. 55, no. 12, pp. 1152–1154, 1989.

[35] J. S. Yoo, H. H. Lee, and P. Zory, "Temperature rise at mirror facet of cw semiconductor lasers," *IEEE journal of quantum electronics*, vol. 28, no. 3, pp. 635–639, 1992.

[36] A. K. Jha, "Thermal characterization of high-power diode lasers using thermoreflectance," Ph.D. dissertation, University of Michigan, 2021.

[37] Y. Sin, Z. Lingley, N. Presser, M. Brodie, N. Ives, and S. C. Moss, "Catastrophic optical bulk damage in high-power ingaas-algaas strained quantum well lasers," *IEEE Journal of Selected Topics in Quantum Electronics*, vol. 23, no. 6, pp. 1–13, 2017.

[38] J. W. Tomm, M. Ziegler, M. Hempel, and T. Elsaesser, "Mechanisms and fast kinetics of the catastrophic optical damage (cod) in gaas-based diode lasers," *Laser & Photonics Reviews*, vol. 5, no. 3, pp. 422–441, 2011.

[39] G. Chen and C. Tien, "Facet heating of quantum well lasers," *Journal of applied physics*, vol. 74, no. 4, pp. 2167–2174, 1993.

[40] T. Shibutani, M. Kume, K. Hamada, *et al.*, "A novel high-power laser structure with current-blocked regions near cavity facets," *IEEE Journal of Quantum Electronics*, vol. 23, no. 6, pp. 760–764, 1987.

[41] J. S. Yoo, H. H. Lee, and P. S. Zory, "On surface recombination velocity and output intensity limit of pulsed semiconductor lasers," *IEEE Photonics technology letters*, vol. 3, no. 7, pp. 594–596, 1991.

[42] J. Jacob, R. Petr, M. Jaspan, *et al.*, "Fault protection of broad-area laser diodes," in *High-Power Diode Laser Technology and Applications VII*, SPIE, vol. 7198, 2009, pp. 324–333.

[43] Y.-K. Su, H. Wang, C. Lin, W. Chen, and S. Chen, "Improvement of algainp light emitting diode by sulfide passivation," *IEEE Photonics Technology Letters*, vol. 15, no. 10, pp. 1345–1347, 2003.

[44] T. Yuasa, M. Ogawa, K. Endo, and H. Yonezu, "Degradation of (alga) as dh lasers due to facet oxidation," *Applied Physics Letters*, vol. 32, no. 2, pp. 119–119, 1978.

[45] A. Oosenbrug, "Reliability aspects of 980-nm pump lasers in edfa applications," in *In-Plane Semiconductor Lasers: from Ultraviolet to Mid-Infrared II*, SPIE, vol. 3284, 1998, pp. 20–27.

[46] L. W. Tu, E. Schubert, M. Hong, and G. Zydzik, "In-vacuum cleaving and coating of semiconductor laser facets using thin silicon and a dielectric," *Journal of applied physics*, vol. 80, no. 11, pp. 6448–6451, 1996.

[47] H. Ichikawa, C. Fukuda, K. Hamada, and T. Nakabayashi, "Facet passivation of gainasp/inp edge-emitting laser diode by aluminum ultrathin layer insertion," *Japanese journal of applied physics*, vol. 47, no. 10R, p. 7890, 2008.

[48] P. Ressel, G. Erbert, U. Zeimer, *et al.*, "Novel passivation process for the mirror facets of al-free active-region high-power semiconductor diode lasers," *IEEE Photonics Technology Letters*, vol. 17, no. 5, pp. 962–964, 2005.

[49] G. Beister, J. Maege, D. Gutsche, *et al.*, "Simple method for examining sulphur passivation of facets in ingaas-algaas (lambda= 0.98 μm) laser diodes," *Applied physics letters*, vol. 68, no. 18, pp. 2467–2468, 1996.

[50] E. V. Konenkova, "Modification of gaas (1 0 0) and gan (0 0 0 1) surfaces by treatment in alcoholic sulfide solutions," *Vacuum*, vol. 67, no. 1, pp. 43–52, 2002.

[51] C. Silfvenius, P. Blixt, C. LINDSTRÖM, and A. Feitisch, "Native-nitride passivation eliminates facet failure," *Laser focus world*, vol. 39, no. 11, pp. 69–73, 2003.

[52] Y. Chou, R. Lai, G. Li, *et al.*, "Innovative nitride passivation of 0.1/spl mu/m ingaas/inalas/inp hemts using high-density inductively coupled plasma cvd (hd-icp-cvd)," in *Conference Proceedings. 14th Indium Phosphide and Related Materials Conference (Cat. No. 02CH37307)*, IEEE, 2002, pp. 315–318.

[53] H. Horie, Y. Yamamoto, N. Arai, and H. Ohta, "Thermal rollover characteristics up to 150/spl deg/c of buried-stripe type 980-nm laser diodes with a current injection window delineated by a sin x layer," *IEEE photonics technology letters*, vol. 12, no. 1, pp. 13–15, 2000.

[54] F. Rinner, J. Rogg, M. Kelemen, *et al.*, "Facet temperature reduction by a current blocking layer at the front facets of high-power ingaas/algaas lasers," *Journal of applied physics*, vol. 93, no. 3, pp. 1848–1850, 2003.

[55] J. Hashimoto, T. Katsuyama, I. Yoshida, M. Murata, and H. Hayashi, "Stable singlemode operation of 0.98 μm gainas/gainasp/gainp buried ridge stripe laser with algainp current blocking layer," *Electronics Letters*, vol. 30, no. 14, pp. 1146–1147, 1994.

[56] J. Michaud, P. Del Vecchio, L. Béchou, *et al.*, "Precise facet temperature distribution of high-power laser diodes: Unpumped window effect," *IEEE Photonics Technology Letters*, vol. 27, no. 9, pp. 1002–1005, 2015.

[57] M. Lee, J. Song, J. Yu, T. Kim, H. Lim, and Y. Lee, "Intermixing behavior in ingaas/ingaasp multiple quantum wells with dielectric and ingaas capping layers," *Applied Physics A*, vol. 73, pp. 357–360, 2001.

[58] J. H. Marsh, "Quantum well intermixing," *Semiconductor science and technology*, vol. 8, no. 6, p. 1136, 1993.

[59] H.-C. Ko, M.-W. Cho, J.-H. Chang, and M. Yang, "A new structure of 780 nm algaas/gaas high power laser diode with non-absorbing mirrors.," *Applied Physics A: Materials Science & Processing*, vol. 68, no. 4, 1999.

[60] R. Thornton, D. Welch, R. Burnham, T. Paoli, and P. Cross, "High power (2.1 w) 10-stripe algaas laser arrays with si disordered facet windows," *Applied physics letters*, vol. 49, no. 23, pp. 1572–1574, 1986.

[61] C. Walker, A. Bryce, and J. Marsh, "Improved catastrophic optical damage level from laser with nonabsorbing mirrors," *IEEE Photonics Technology Letters*, vol. 14, no. 10, pp. 1394–1396, 2002.

[62] H. Yonezu, M. Ueno, T. Kamejima, and I. Hayashi, "An algaas window structure laser," *IEEE Journal of Quantum Electronics*, vol. 15, no. 8, pp. 775–781, 1979.

[63] H. Taniguchi, H. Ishii, R. Minato, Y. Ohki, T. Namegaya, and A. Kasukawa, "25-w 915-nm lasers with window structure fabricated by impurity-free vacancy disordering (ifvd)," *IEEE Journal of Selected Topics in Quantum Electronics*, vol. 13, no. 5, pp. 1176–1179, 2007.

[64] P. Piva, S. Fafard, M. Dion, *et al.*, "Reduction of ingaas/gaas laser facet temperatures by band gap shifted extended cavities," *Applied physics letters*, vol. 70, no. 13, pp. 1662–1664, 1997.

[65] P. Piva, R. Goldberg, I. Mitchell, *et al.*, "Reduced 980 nm laser facet absorption by band gap shifted extended cavities," *Journal of Vacuum Science & Technology B: Microelectronics and Nanometer Structures Processing, Measurement, and Phenomena*, vol. 16, no. 4, pp. 1790–1793, 1998.

[66] R. Lammert, G. Smith, D. Forbes, M. Osowski, and J. Coleman, "Strained-layer ingaas-gaas-aigaas buried-heterostructure lasers with nonabsorbing mirrors by selective-area mocvd," in *Semiconductor Lasers: Advanced Devices and Applications*, Optica Publishing Group, 1995, pp. MC–3.

[67] F. Gfeller, P. Buchmann, P. Epperlein, H. Meier, and J. Reithmaier, "High-power single-mode algaas lasers with bent-waveguide nonabsorbing etched mirrors," *Journal of applied physics*, vol. 72, no. 6, pp. 2131–2135, 1992.

[68] J. Ungar, N. Bar-Chaim, and I. Ury, "High-power gaalas window lasers," *Electronics Letters*, vol. 22, no. 5, pp. 279–280, 1986.

[69] D. Botez, "Design considerations and analytical approximations for high continuous-wave power, broad-waveguide diode lasers," *Applied Physics Letters*, vol. 74, no. 21, pp. 3102–3104, 1999.

[70] I. Petrescu-Prahova, P. Modak, E. Goutain, *et al.*, "High d/gamma values in diode laser structures for very high power," in *High-Power Diode Laser Technology and Applications VII*, SPIE, vol. 7198, 2009, pp. 445–452.

[71] J. Pomplun, S. Burger, F. Schmidt, *et al.*, "Finite element simulation of the optical modes of semiconductor lasers," *physica status solidi (b)*, vol. 247, no. 4, pp. 846–853, 2010.

[72] M. Maximov, Y. M. Shernyakov, I. Novikov, L. Y. Karachinsky, N. Y. Gordeev, and U. Ben, "Ami, db arbiv, a. sharon, va shchukin, nn ledentsov, t. kettler, k. posilovic and d. bimberg,"high–power low–beam divergence edge–emitting semiconductor lasers with 1– and 2–d photonic bandgap crystal waveguide"," *IEEE J. Select. Topics Quant. Electronics*, vol. 14, no. 4, pp. 1113–1122, 2008.

[73] B. Corbett, P. Lambkin, J. O'Callaghan, *et al.*, "Modal analysis of large spot size, low output beam divergence quantum-dot lasers," *IEEE Photonics Technology Letters*, vol. 19, no. 12, pp. 916–918, 2007.

[74] D. R. Miftakhutdinov, A. P. Bogatov, and A. E. Drakin, "Catastrophic optical degradation of the output facet of high-power single-transverse-mode diode lasers. 1. physical model," *Quantum Electronics*, vol. 40, no. 7, p. 583, 2010.

[75] D. R. Miftakhutdinov, A. P. Bogatov, and A. E. Drakin, "Catastrophic optical degradation of the output facet of high-power single-transverse-mode diode lasers. 2. calculation of the spatial temperature distribution and threshold of the catastrophic optical degradation," *Quantum Electronics*, vol. 40, no. 7, p. 589, 2010.

[76] T. Kamejima and H. Yonezu, "Catastrophic optical damage generation mechanism in (alga) as dh lasers," *Japanese Journal of Applied Physics*, vol. 19, no. S1, p. 425, 1980.

[77] B. Hakki and F. Nash, "Catastrophic failure in gaas double-heterostructure injection lasers," *Journal of Applied Physics*, vol. 45, no. 9, pp. 3907–3912, 1974.

[78] O. Ueda, K. Wakao, S. Komiya, A. Yamaguchi, S. Isozumi, and I. Umebu, "Catastrophic degradation of ingaasp/ingap double-heterostructure lasers grown on (001) gaas substrates by liquid-phase epitaxy," *Journal of applied physics*, vol. 58, no. 11, pp. 3996–4002, 1985.

[79] S. N. Elliott, P. M. Smowton, M. Ziegler, J. W. Tomm, and U. Zeimer, "Time resolved studies of catastrophic optical mirror damage in red-emitting laser diodes," *Journal of Applied Physics*, vol. 107, no. 12, 2010.

[80] R. Mallard, R. Clayton, D. Mayer, and L. Hobbs, "Failure analysis of high power gaas-based lasers using electron beam induced current analysis and transmission electron microscopy," *Journal of Vacuum Science & Technology A: Vacuum, Surfaces, and Films*, vol. 16, no. 2, pp. 825–829, 1998.

[81] M. Ziegler, J. W. Tomm, D. Reeber, *et al.*, "Catastrophic optical mirror damage in diode lasers monitored during single-pulse operation," *Applied Physics Letters*, vol. 94, no. 19, 2009.

[82] K. Park, J. Lee, D. Jang, *et al.*, "Characterization of catastrophic optical damage in al-free ingaas/ingap 0.98 μm high-power lasers," *Applied physics letters*, vol. 73, no. 18, pp. 2567–2569, 1998.

[83] A. Chin, R. Bertaska, M. Jaspan, *et al.*, "A comprehensive model of catastrophic optical-damage in broad-area laser diodes," in *High-Power Diode Laser Technology and Applications VII*, SPIE, vol. 7198, 2009, pp. 375–390.

[84] M. Bou Sanayeh, A. Jaeger, W. Schmid, *et al.*, "Investigation of dark line defects induced by catastrophic optical damage in broad-area algainp laser diodes," *Applied physics letters*, vol. 89, no. 10, 2006.

[85] M. B. Sanayeh, "Catastrophic optical damage in high power algainp diode lasers," Ph.D. dissertation, Duisburg, Essen, Univ., Diss., 2008, 2008.

[86] C. Snyder, J. Lee, R. Hull, and R. Logan, "Catastrophic degradation lines at the facet of ingaasp/inp lasers investigated by transmission electron microscopy," *Applied physics letters*, vol. 67, no. 4, pp. 488–490, 1995.

[87] D. Hull and D. J. Bacon, *Introduction to dislocations*. Elsevier, 2011, vol. 37.

[88] J. D. Weeks, J. C. Tully, and L. Kimerling, "Theory of recombination-enhanced defect reactions in semiconductors," *Physical Review B*, vol. 12, no. 8, p. 3286, 1975.

[89] P. Hutchinson and P. Dobson, "Defect structure of degraded gaalas-gaas double heterojunction lasers," *Philosophical Magazine*, vol. 32, no. 4, pp. 745–754, 1975.

[90] P. Petroff and R. Hartman, "Rapid degradation phenomenon in heterojunction gaalas–gaas lasers," *Journal of Applied Physics*, vol. 45, no. 9, pp. 3899–3903, 1974.

[91] M. Ishii, H. Kan, W. Susaki, and Y. Ogata, "Suppression of defect formation in gaas layers by removing oxygen in lpe," *Applied Physics Letters*, vol. 29, no. 6, pp. 375–375, 1976.

[92] H. Wang, A. Hopgood, and G. Ng, "Analysis of dark-line defect growth suppression in in x ga 1- x as/gaas strained heterostructures," *Journal of applied physics*, vol. 81, no. 7, pp. 3117–3123, 1997.

[93] P. Kirkby, "Dislocation pinning in gaas by the deliberate introduction of impurities," *IEEE Journal of Quantum Electronics*, vol. 11, no. 7, pp. 562–568, 1975.

[94] R. Waters, S. Yellen, N. Ruggieri, and D. Bour, "Inhibited dark-line defect formation in strained ingaas/algaas quantum well lasers," *IEEE photonics technology letters*, vol. 2, pp. 531–533, 1990.

[95] K. Ishida, T. Kamejima, and J. Matsui, "Nature of¡ 110¿ dark-line defects in degraded (gaal) as-gaas double-heterostructure lasers," *Applied Physics Letters*, vol. 31, no. 6, pp. 397–399, 1977.

[96] O. Ueda, I. Umebu, S. Yamakoshi, and T. Kotani, "Nature of dark defects revealed in ingaasp/inp double heterostructure light emitting diodes aged at room temperature," *Journal of Applied Physics*, vol. 53, no. 4, pp. 2991–2997, 1982.

[97] O. Ueda, "Degradation of iii–v opto-electronic devices," *Journal of the Electrochemical Society*, vol. 135, no. 1, p. 11C, 1988.

[98] R. Hartman and A. Hartman, "Strain-induced degradation of gaas injection lasers," *Applied Physics Letters*, vol. 23, no. 3, pp. 147–149, 1973.

[99] K. Fukagai, S. Ishikawa, and K. E. Yuasa, "Current density dependence for dark-line defect growth velocity in strained ingaas/algaas quantum well laser diodes," *Japanese journal of applied physics*, vol. 30, no. 3A, p. L371, 1991.

[100] T. Egawa, Y. Hasegawa, T. Jimbo, and M. Umeno, "Degradation mechanism of algaas/gaas laser diodes grown on si substrates," *Applied physics letters*, vol. 67, no. 20, pp. 2995–2997, 1995.

[101] Y. Hasegawa, T. Egawa, T. Jimbo, and M. Umeno, "Influences of dark line defects on characteristics of algaas/gaas quantum well lasers grown on si substrates," *Japanese journal of applied physics*, vol. 34, no. 6R, p. 2994, 1995.

[102] H. Imai, T. Fujiwara, K. Segi, M. Takusagawa, and H. Takanashi, "Degradations of optically-pumped gaalas double heterostructures at elevated temperatures," *Japanese Journal of Applied Physics*, vol. 18, no. 3, p. 589, 1979.

[103] K. Maeda, M. Sato, A. Kubo, and S. Takeuchi, "Quantitative measurements of recombination enhanced dislocation glide in gallium arsenide," *Journal of Applied Physics*, vol. 54, no. 1, pp. 161–168, 1983.

[104] K. Maeda and S. Takeuchi, "Enhancement of dislocation mobility in semiconducting crystals by electronic excitation," in *Dislocations in solids*, vol. 10, Elsevier, 1996, pp. 443–504.

[105] Y. Nannichi, J. Matsui, and K. Ishida, "Rapid degradation in double-heterostructure lasers. ii. semiquantitative analyses on the propagation of dark line defects," *Japanese Journal of Applied Physics*, vol. 14, no. 10, p. 1561, 1975.

[106] T. Coenen and N. Haegel, "Cathodoluminescence for the 21st century: Learning more from light," *Applied Physics Reviews*, vol. 4, no. 3, 2017.

[107] S. Dadgostar, J. Souto, and J. Jiménez, "Cl as a tool for device characterisation: The case of laser diode degradation," *Nano Express*, vol. 2, no. 1, p. 014 001, 2021.

[108] A. Martín-Martín, M. Avella, M. Pommiès, *et al.*, "Study of the degradation of algaas-based high-power laser bars: V defects," *Journal of Materials Science: Materials in Electronics*, vol. 19, pp. 140–144, 2008.

[109] M. Hempel, F. La Mattina, J. W. Tomm, U. Zeimer, R. Broennimann, and T. Elsaesser, "Defect evolution during catastrophic optical damage of diode lasers," *Semiconductor Science and Technology*, vol. 26, no. 7, p. 075 020, 2011.

[110] S. Zhang, L. Li, and A. Kumar, *Materials characterization techniques*. CRC press, 2008.

[111] S. Ruvimov, A. Klein, U. Richter, I. Rechenberg, K. Scheerschmidt, and J. Heydenreich, "Tem study of the rapid degradation of pump laser diodes," *physica status solidi (a)*, vol. 146, no. 1, pp. 415–424, 1994.

[112] Y. Li, W. Tang, Y. Zhang, *et al.*, "Nanoscale characterization of v-defect in ingan/gan qws leds using near-field scanning optical microscopy," *Nanomaterials*, vol. 9, no. 4, p. 633, 2019.

[113] B. Kim, D. Moon, K. Joo, *et al.*, "Investigation of leakage current paths in n-gan by conductive atomic force microscopy," *Applied Physics Letters*, vol. 104, no. 10, 2014.

[114] A. Orlando, F. Franceschini, C. Muscas, *et al.*, "A comprehensive review on raman spectroscopy applications," *Chemosensors*, vol. 9, no. 9, p. 262, 2021.

[115] C. F. Geraldes, "Introduction to infrared and raman-based biomedical molecular imaging and comparison with other modalities," *Molecules*, vol. 25, no. 23, p. 5547, 2020.

[116] S. D. McGrane, D. S. Moore, P. M. Goodwin, and D. M. Dattelbaum, "Quantitative tradeoffs between spatial, temporal, and thermometric resolution of nonresonant raman thermometry for dynamic experiments," *Applied Spectroscopy*, vol. 68, no. 11, pp. 1279–1288, 2014.

[117] P. Epperlein, G. Bona, and P. Roentgen, "Local mirror temperatures of red-emitting (al) gainp quantum-well laser diodes by raman scattering and reflectance modulation measurements," *Applied physics letters*, vol. 60, no. 6, pp. 680–682, 1992.

[118] R. Puchert, J. Tomm, A. Jaeger, A. Bärwolff, J. Luft, and W. Späth, "Emitter failure and thermal facet load in high-power laser diode arrays.," *Applied Physics A: Materials Science & Processing*, vol. 66, no. 5, 1998.

[119] T. Q. Tien, F. Weik, J. W. Tomm, *et al.*, "Thermal properties and degradation behavior of red-emitting high-power diode lasers," *Applied physics letters*, vol. 89, no. 18, 2006.

[120] W. S. Yoo, J. H. Kim, and S. M. Han, "Multiwavelength raman characterization of silicon stress near through-silicon vias and its inline monitoring applications," *Journal of Micro/Nanolithography, MEMS, and MOEMS*, vol. 13, no. 1, pp. 011 205–011 205, 2014.

[121] M. Ziegler, J. W. Tomm, T. Elsaesser, C. Matthiesen, M. Bou Sanayeh, and P. Brick, "Real-time thermal imaging of catastrophic optical damage in red-emitting high-power diode lasers," *Applied Physics Letters*, vol. 92, no. 10, 2008.

[122] Z. M. Zhang and G. Machin, "Overview of radiation thermometry," *Experimental Methods in the Physical Sciences*, vol. 42, pp. 1–28, 2009.

[123] O. MARTIN and P. EPPERLEIN, "Reflectance modulation studies on laser diode mirrors," *Gallium Arsenide And Related Compounds 1991*, pp. 353–358, 1992.

[124] P. Chan, K. Pipe, Z. Mi, J. Yang, P. Bhattacharya, and D. Lüerßen, "Thermal relaxation time and heat distribution in pulsed ingaas quantum dot lasers," *Applied physics letters*, vol. 89, no. 1, 2006.

[125] P. K. Chan, K. P. Pipe, G. Qin, and Z. Ma, "Thermoreflectance imaging of current dynamics in high power sige heterojunction bipolar transistors," *Applied physics letters*, vol. 89, no. 23, 2006.

[126] M. Farzaneh, K. Maize, D. Lüerßen, *et al.*, "Ccd-based thermoreflectance microscopy: Principles and applications," *Journal of Physics D: Applied Physics*, vol. 42, no. 14, p. 143 001, 2009.

[127] D. Pierścińska, A. Kozlowska, K. Pierściński, *et al.*, "Thermal processes in high-power laser bars investigated by spatially resolved thermoreflectance," *Journal of Materials Science: Materials in Electronics*, vol. 19, pp. 150–154, 2008.

[128] S. Dilhaire, S. Grauby, and W. Claeys, "Thermoreflectance calibration procedure on a laser diode: Application to catastrophic optical facet damage analysis," *IEEE electron device letters*, vol. 26, no. 7, pp. 461–463, 2005.

[129] J. Landesman, E. Martin, B. Depret, A. Fily, and P. Braun, "Local channel temperature measurements on pseudomorphic high electron mobility transistors by photoluminescence spectroscopy," *MRS Online Proceedings Library (OPL)*, vol. 516, p. 45, 1998.

[130] Y. P. Varshni, "Temperature dependence of the energy gap in semiconductors," *physica*, vol. 34, no. 1, pp. 149–154, 1967.

[131] T. Moss, "Relations between the refractive index and energy gap of semiconductors," *physica status solidi (b)*, vol. 131, no. 2, pp. 415–427, 1985.

[132] E. Matatagui, A. Thompson, and M. Cardona, "Thermoreflectance in semiconductors," *Physical Review*, vol. 176, no. 3, p. 950, 1968.

[133] J. Christofferson and A. Shakouri, "Thermoreflectance based thermal microscope," *Review of Scientific Instruments*, vol. 76, no. 2, 2005.

[134] S. Grauby, B. Forget, S. Hole, and D. Fournier, "High resolution photothermal imaging of high frequency phenomena using a visible charge coupled device camera associated with a multichannel lock-in scheme," *Review of Scientific Instruments*, vol. 70, no. 9, pp. 3603–3608, 1999.

[135] S. Grauby, A. Salhi, J.-M. Rampnoux, H. Michel, W. Claeys, and S. Dilhaire, "Laser scanning thermoreflectance imaging system using galvanometric mirrors for temperature measurements of microelectronic devices," *Review of Scientific Instruments*, vol. 78, no. 7, 2007.

[136] J. Christofferson, K. Maize, Y. Ezzahri, J. Shabani, X. Wang, and A. Shakouri, "Microscale and nanoscale thermal characterization techniques," *Journal of Electronic Packaging*, vol. 130, no. 4, p. 041 101, Nov. 2008.

[137] P. M. Mayer, D. Lüerßen, R. J. Ram, and J. A. Hudgings, "Theoretical and experimental investigation of the thermal resolution and dynamic range of ccd-based thermoreflectance imaging," *JOSA A*, vol. 24, no. 4, pp. 1156–1163, 2007.

[138] L. Gammaitoni, P. Hänggi, P. Jung, and F. Marchesoni, "Stochastic resonance," *Reviews of modern physics*, vol. 70, no. 1, p. 223, 1998.

[139] D. Luerssen, J. A. Hudgings, P. M. Mayer, and R. J. Ram, "Nanoscale thermoreflectance with 10mk temperature resolution using stochastic resonance," in *Semiconductor Thermal Measurement and Management IEEE Twenty First Annual IEEE Symposium, 2005.*, IEEE, 2005, pp. 253–258.

[140] I. Vurgaftman, J. Meyer, and L. R. Ram-Mohan, "Band parameters for iii–v compound semiconductors and their alloys," *Journal of applied physics*, vol. 89, no. 11, pp. 5815–5875, 2001.

[141] A. K. Jha, C. Li, K. P. Pipe, *et al.*, "Measurement of facet optical absorption in high power diode lasers using thermoreflectance," in *2019 IEEE High Power Diode Lasers and Systems Conference (HPD)*, IEEE, 2019, pp. 25–26.

[142] E. D. McVay, R. J. Deri, S. H. Baxamusa, *et al.*, "Aging mechanisms of broad area ~800 nm laser diodes," *IEEE Journal of Selected Topics in Quantum Electronics*, vol. 31, pp. 1–9, 2025.

[143] F. Dabkowski, A. Chin, P. Gavrilovic, S. Alie, and D. Beyea, "Temperature profile along the cavity axis of high power quantum well lasers during operation," *Applied physics letters*, vol. 64, no. 1, pp. 13–15, 1994.

[144] M. Ziegler, R. Pomraenke, M. Felger, *et al.*, "Infrared emission from the substrate of gaas-based semiconductor lasers," *Applied Physics Letters*, vol. 93, no. 4, 2008.

[145] A. Kozlowska, P. Wawrzyniak, J. W. Tomm, F. Weik, and T. Elsaesser, "Deep level emission from high-power diode laser bars detected by multispectral infrared imaging," *Applied Physics Letters*, vol. 87, no. 15, 2005.

[146] J. W. Tomm, F. Weik, A. Kozlowska, M. Latoszek, M. Bugajski, and M. Zbroszczyk, "New characterization methods for semiconductor lasers," in *Optoelectronic Devices: Physics, Fabrication, and Application II*, SPIE, vol. 6013, 2005, pp. 183–190.

[147] M. Hempel, J. W. Tomm, F. Yue, M. A. Bettiati, and T. Elsaesser, "Short-wavelength infrared defect emission as a probe of degradation processes in 980 nm single-mode diode lasers," *Laser & Photonics Reviews*, vol. 8, no. 5, pp. L59–L64, 2014.

[148] M. Hempel, J. W. Tomm, T. Elsaesser, D. Venables, V. Rossin, and E. Zucker, "Analysis of 980nm emitting single-spatial mode diode lasers at high power levels by complementary imaging techniques," in *High-Power Diode Laser Technology and Applications XIII*, SPIE, vol. 9348, 2015, pp. 197–202.

[149] J. W. Tomm, M. Ziegler, H. Kissel, and J. Biesenbach, "Defect imaging in laser diodes by mapping their near-infrared emission," *Journal of electronic materials*, vol. 39, pp. 723–726, 2010.

[150] A. Kozlowska, P. Wawrzyniak, A. Malag, M. Teodorczyk, J. W. Tomm, and F. Weik, "Reliability screening of diode lasers by multispectral infrared imaging," *Journal of applied physics*, vol. 99, no. 5, 2006.

[151] R. Kernke, M. Hempel, J. W. Tomm, *et al.*, "Shortwave infrared (swir) emission from 450 nm ingan diode lasers," *Optical Materials Express*, vol. 6, no. 6, pp. 2139–2146, 2016.

[152] A. Alkauskas, J. L. Lyons, D. Steiauf, and C. G. Van de Walle, "First-principles calculations of luminescence spectrum line shapes for defects in semiconductors: The example of gan and zno," *Physical review letters*, vol. 109, no. 26, p. 267 401, 2012.

[153] A. Alkauskas, M. D. McCluskey, and C. G. Van de Walle, "Tutorial: Defects in semiconductors—combining experiment and theory," *Journal of Applied Physics*, vol. 119, no. 18, 2016.

[154] S. Rauch, H. Wenzel, M. Radziunas, M. Haas, G. Tränkle, and H. Zimer, "Impact of longitudinal refractive index change on the near-field width of high-power broad-area diode lasers," *Applied Physics Letters*, vol. 110, no. 26, 2017.

[155] S. Khamari, S. Arslan, C. Zink, S. J. Sweeney, and P. Crump, "Carrier density non-pinning at stripe edges and widened lateral far field due to longitudinal temperature variation in broad-area high power diode lasers," *Applied Physics Letters*, vol. 122, no. 21, 2023.

[156] M. Gonzalez, A. Carlin, C. Dohrman, E. Fitzgerald, and S. Ringel, "Determination of bandgap states in p-type in0. 49ga0. 51p grown on sige/si and gaas by deep level optical spectroscopy and deep level transient spectroscopy," *Journal of Applied Physics*, vol. 109, no. 6, 2011.

[157] J. Cederberg, B. Bieg, J. .-. Huang, S. Stockman, M. Peanasky, and T. Kuech, "Oxygen-related deep levels in al 0.5 in 0.5 p grown by movpe," *Journal of electronic materials*, vol. 29, pp. 426–429, 2000.

[158] A. Raisanen, L. Brillson, R. Goldman, K. L. Kavanagh, and H. Wieder, "Dislocation-induced deep level states in in 0.08 ga 0.92 as/gaas heterostructures," *Journal of electronic materials*, vol. 23, pp. 929–933, 1994.

[159] E. McVay, R. Deri, D. Mittelberger, *et al.*, "Laser beam induced current for defect concentration and aging analysis of broad area laser diodes," in *CLEO 2024*, Optica Publishing Group, 2024.

[160] A. Knauer, H. Wenzel, G. Erbert, B. Sumpf, and M. Weyers, "Influence of oxygen in algaas-based laser structures with al-free active region on device properties," *Journal of electronic materials*, vol. 30, pp. 1421–1424, 2001.

[161] J. S. Roberts, L. M. Smith, and P. L. Tihanyi, "Residual oxygen contamination of inalgaas sqw high-power laser diodes," in *In-Plane Semiconductor Lasers IV*, SPIE, vol. 3947, 2000, pp. 58–65.

[162] Y. Mihashi, M. Miyashita, N. Kaneno, *et al.*, "Influence of oxygen on the threshold current of algaas multiple quantum well lasers grown by metalorganic chemical vapor deposition," *Journal of crystal growth*, vol. 141, no. 1-2, pp. 22–28, 1994.

[163] L. Kimerling, P. Petroff, and H. Leamy, "Injection-stimulated dislocation motion in semiconductors," *Applied Physics Letters*, vol. 28, no. 6, pp. 297–300, 1976.

[164] A. Hopgood, "Vacancy-controlled model of degradation in ingaas/algaas/gaas heterostructure lasers," *Journal of applied physics*, vol. 76, no. 7, pp. 4068–4071, 1994.

[165] S. K. Choi, M. Mihara, and T. Ninomiya, "Dislocation velocities in gaas," *Japanese Journal of Applied Physics*, vol. 16, no. 5, p. 737, 1977.

[166] I. Yonenaga and K. Sumino, "Effects of in impurity on the dynamic behavior of dislocations in gaas," *Journal of applied physics*, vol. 62, no. 4, pp. 1212–1219, 1987.

[167] B. Schwartz, "Dark line defect growth in optically pumped al x ga1- x as laser material," *Journal of applied physics*, vol. 58, no. 2, pp. 677–682, 1985.

[168] H. Nakashima, S. Kishino, N. Chinone, and R. Ito, "Growth and propagation mechanism of¡ 110¿-oriented dark-line defects in gaas-ga1- x al x as double heterostructure crystals," *Journal of Applied Physics*, vol. 48, no. 7, pp. 2771–2775, 1977.

[169] S. Arslan, H. Wenzel, J. Fricke, *et al.*, "The impact of longitudinal spatial hole burning on the carrier density profile in high-power lasers," in *2021 27th International Semiconductor Laser Conference (ISLC)*, IEEE, 2021, pp. 1–2.

[170] R. Swertfeger, S. Patra, R. Deri, *et al.*, "Longitudinal current crowding as power limit in high power 975 nm diode lasers," in *2020 IEEE Photonics Conference (IPC)*, IEEE, 2020, pp. 1–2.

[171] S. Arslan, R. Swertfeger, J. Fricke, *et al.*, "Non-uniform longitudinal current density induced power saturation in gaas-based high power diode lasers," *Applied Physics Letters*, vol. 117, no. 20, 2020.

[172] S. Arslan, H. Wenzel, J. Fricke, *et al.*, "Experimental and theoretical studies into longitudinal spatial hole burning as a power limit in high-power diode lasers at 975 nm," *Applied Physics Letters*, vol. 122, no. 26, 2023.

[173] T. Hao, J. Song, R. Liptak, and P. O. Leisher, "Experimental verification of longitudinal spatial hole burning in high-power diode lasers," in *Laser Technology for Defense and Security X*, SPIE, vol. 9081, 2014, pp. 117–125.

[174] G. Björklund and H. Grimmeiss, "Determination of optical ionization cross sections in gap using charge storage and impurity photovoltaic effect," *Solid-State Electronics*, vol. 14, no. 7, pp. 589–601, 1971.

[175] C. Henry, H. Kukimoto, G. Miller, and F. Merritt, "Photocapacitance studies of the oxygen donor in gap. ii. capture cross sections," *Physical Review B*, vol. 7, no. 6, p. 2499, 1973.